

1  
2  
3  
4  
5  
6  
7  
8 **A cortical circuit for orchestrating oromanual food manipulation**  
9

10  
11  
12 Xu An<sup>1,2</sup>, Katherine Matho<sup>2</sup>, Yi Li<sup>1,2</sup>, Hemanth Mohan<sup>1,2</sup>, X. Hermione Xu<sup>1,5</sup>, Ian Q. Whishaw<sup>3</sup>,  
13 Adam Kepecs<sup>4\*</sup>, Z. Josh Huang<sup>1,2,5\*</sup>  
14  
15

16 <sup>1</sup>Department of Neurobiology, Duke University Medical Center, Durham, NC 27710, USA

17 <sup>2</sup>Cold Spring Harbor Laboratory, Cold Spring Harbor, NY 11724, USA

18 <sup>3</sup>Department of Neuroscience, Canadian Centre for Behavioural Research, University of Lethbridge,  
19 Lethbridge, AB, T1K 3M4, Canada

20 <sup>4</sup>Department of Neuroscience and Department of Psychiatry, Washington University in St. Louis, St.  
21 Louis, MO, USA.

22 <sup>5</sup>Department of Biomedical Engineering, Duke University Pratt School of Engineering, Durham,  
23 NC 27708, USA  
24  
25  
26  
27  
28  
29  
30  
31  
32  
33  
34

35 \*corresponding authors: [josh.huang@duke.edu](mailto:josh.huang@duke.edu); [akepecs@wustl.edu](mailto:akepecs@wustl.edu)  
36  
37

38  
39 **ABSTRACT**  
40

41 Cooperative forelimb and mouth movements during eating contribute to diet selection among  
42 vertebrates including the oromanual manipulatory skills in rodents and primates. Whereas spinal and  
43 brainstem circuits implement forelimb and orofacial actions, whether there is a specialized cortical  
44 circuit that flexibly assembles these to achieve cross-body and oromanual coordination for skilled  
45 manipulation remains unclear. Here we discover a cortical region and its cell-type-specific circuitry that  
46 orchestrates body postures and oromanual coordination for food manipulation in mice. An optogenetic  
47 screen of cortical areas and projection neuron types identified a rostral forelimb-orofacial area (RFO),  
48 wherein activation of pyramidal tract ( $PT^{Fezf2}$ ) and intratelencephalic ( $IT^{PlxnD1}$ ) neurons induced  
49 concurrent posture, forelimb and orofacial eating-like movements. In a pasta-eating behavior, RFO  
50  $PT^{Fezf2}$  and  $IT^{PlxnD1}$  activity were closely correlated with picking up the pasta, adopting a sitting posture,  
51 oromanual manipulation, and hand-assisted biting. RFO inactivation and inhibition of RFO  $PTs^{Fezf2}$  and  
52  $ITs^{PlxnD1}$  impaired posture and oromanual coordination, leading to deficient pasta manipulation and  
53 biting. RFO is reciprocally connected to forelimb and orofacial sensorimotor areas as well as insular and  
54 visceral areas. Within this network,  $ITs^{PlxnD1}$  project bilaterally to the entire network and the ventrolateral  
55 striatum and  $PTs^{Fezf2}$  project to multiple subcortical areas associated with forelimb and orofacial  
56 control. These results suggest that  $ITs^{PlxnD1}$  select and coordinate the feeding program involving multiple  
57 body parts and  $PTs^{Fezf2}$  implement the fine details of movements. Our study reveals a neural circuit basis  
58 of hand-mouth coordination for object manipulation.

## 59 INTRODUCTION

60  
61 Using the hands to assist feeding is characteristic of many vertebrate orders and amongst  
62 Euarchontoglires such as rodents and primates, features a sitting posture associated with cooperative  
63 food handling by the hands and the mouth<sup>1-3</sup>. This characteristic of feeding is a behavioral  
64 innovation that has diversified dietary options, relaxing constraints imposed by environmental niches  
65<sup>1,3</sup>. The adoption of a sitting posture releases forelimbs from body support and allows for flexible  
66 coordination of hand and mouth movements. These movements feature the manipulation of food by  
67 the hands so that it can be oriented for transfer into the mouth, the transfer of food from the mouth to  
68 the hands for acts such as holding while chewing, and the cooperation of the hands and mouth in  
69 food preparation acts such as biting<sup>3-5</sup>. The neural circuitry that contributes to the orchestration of  
70 these skilled movements across multiple body parts, especially the coordination of hand and mouth  
71 in manipulation, is almost entirely unknown. Nevertheless, it is likely that the elaboration of this  
72 neural circuitry contributes to evolution of the diversity of hand skills in serial order displayed by  
73 higher primates including humans<sup>6,7</sup>.

74  
75 In the hierarchically organized vertebrate motor control infrastructure<sup>8-10</sup>, lower-level controllers in  
76 brainstem regions are capable of issuing commands that mediate diverse actions such as reach,  
77 grasp, lick, bite, and chew<sup>11</sup>. How these actions are flexibly coordinated to achieve food retrieval  
78 and food manipulation toward an integrated behavior such as feeding is largely unclear. Although  
79 major insight has been gained from studying relatively isolated and well-trained forelimb  
80 movements, such as reach and grasp in non-human primates<sup>12-15</sup> and rodents<sup>16-20</sup>, more complex  
81 and flexible natural behaviors to achieve ethological goals<sup>21,22</sup> have rarely been examined. In  
82 particular, little attention has been directed toward understanding the integrated movements of hands  
83 and mouth with body posture required for the complex behavior of food manipulation. This is due in  
84 part to the involvement of multiple body parts making it challenging to study the underlying brain  
85 circuit mechanisms.

86  
87 The present study uses the laboratory mouse, which displays sophisticated sensorimotor behaviors  
88 that enable feeding on a wide variety of otherwise non-accessible food items, such as shelled seeds  
89 and nutrient-rich body parts of captured insects, through oromanual manipulation<sup>5,23-26</sup>. Thus, the  
90 mouse represents a valuable experimental model for exploring the neural basis of manipulation and  
91 enables the application of the full suite of genetic tools for neural circuit analysis<sup>27,28</sup>. Here,  
92 combining a systematic optogenetic screen of projection neuron (PN) types and cortical areas with a  
93 quantitative analysis of a natural feeding behavior, cell-type resolution neural recording, functional  
94 manipulation, and input-output circuit mapping, we describe a cortical area and its associated brain  
95 circuits that orchestrate body postures and oromanual coordination for food manipulation.

## 97 RESULTS

### 99 **Optogenetic identification of a cortical area that elicits oromanual fictive eating**

We performed an optogenetic activation screen to identify cortical regions involved in coordinated forelimb and orofacial movements. Classic micro-stimulation experiments in humans<sup>29</sup>, non-human primates<sup>30,31</sup>, and rodents<sup>32-34</sup> have revealed topographic motor maps of cortical areas that induce body part movement. Recent optogenetic activation studies in mice have probed more restricted cortical cell populations in motor control<sup>35-37</sup>, but these have been limited to a few mostly mixed neuronal populations (e.g. Thy1 transgenic lines), and thus have yet to achieve neuron type and neural circuit resolution. We have recently generated a suite of mouse knock-in driver lines targeting hierarchically organized cortical PNs, including pyramidal tract (PT), corticothalamic (CT), and intratelencephalic (IT) classes, and subpopulations therein<sup>38</sup>. To systematically examine the role of different cortical areas and PN types in forelimb and orofacial motor control, we used these driver lines to express channelrhodopsin (ChR2) in 8 different neural populations, including subpopulations of PT (*Fezf2*, *Tcerg11*, *Sema3e*), IT (*PlxnD1*, *Tbr2*), and CT (*Tle4*) neurons, with comparisons to a broad PN line (*Emx1*) and a previously used *Thy1* transgenic line 18 (*Thy1-Tg18*) targeting mixed PN populations<sup>39</sup> (**Fig. 1a**). Using a head-fixed preparation, we directed a laser beam (473 nm, 50 Hz, 0.5 s) through thinned skull to activate each of 128 sites on a 375- $\mu$ m resolution grid within a 3 mm x 6 mm region of the right dorsal cortex while recording forelimb and orofacial movements using high-speed cameras (**Fig. 1b, c**). Among the 8 driver lines screened (**Fig. 1d, Extended Data Fig. 1a-f**), PT<sup>Fezf2</sup> and IT<sup>PlxnD1</sup> activation induced robust and coordinated forelimb and orofacial movements; we thus focused subsequent investigation on these two cell types.

The *Fezf2-CreER* driver line captures a majority of corticofugal neurons projecting to striatal, thalamic, collicular, brainstem, and spinal targets<sup>38</sup>. Activation of PTs<sup>Fezf2</sup> across the dorsal cortex of *Fezf2;Ai32* mice (expressing ChR2 in PTs<sup>Fezf2</sup>) revealed a topographic motor map of contralateral forelimb and orofacial movements organized along a postero-medial to antero-lateral axis (**Fig. 1d, Extended Data Fig. 2a, b, g, i, j**). Posterior caudal forelimb area (pCFA) stimulation induced lateral forelimb abduction with elbow extension as well as digit opening and extension (**Fig. 1d, Extended Data Fig. 2d, g, Supplementary Video 1**). Medial caudal forelimb area (mCFA) stimulation evoked rhythmic forelimb treading (up-down) movements (**Extended Data Fig. 2a-c, e, Supplementary Video 2**). Anterior caudal forelimb area (aCFA) stimulation induced stepping or reaching-like forelimb movements involving sequential elbow, wrist, and digit flexion followed by extension (**Fig. 1d, Extended Data Fig. 2f, g, Supplementary Video 3**). Notably, PT<sup>Fezf2</sup> activation in an area anterolateral to the CFA induced robust and concurrent forelimb-orofacial movements, which included contralateral forelimb adduction to the body midline with hand supination and digit flexing and closing, jaw opening, and tongue protrusion (**Fig. 1d-j, Extended Data Fig. 2g, Supplementary Video 4**). The sequence of the forelimb and jaw movements appeared to reflect a coordinated behavior suitable for delivering food to the mouth (**Fig. 1e**). We named this area the Rostral Forelimb Orofacial area (RFO). RFO lies at partially overlapped location with the tongue-jaw motor cortex (tJM1), previously identified by examining only orofacial movements<sup>40</sup>.

The *PlxnD1-CreER* driver line captures a major IT population in L2/3/5A that projects bilaterally to the cortex and striatum<sup>38</sup>. IT<sup>PlxnD1</sup> activation in most cortical areas only induced weak or no observable forelimb movement (**Fig. 1d, Extended Data Fig. 2a, b, h**). Strikingly, IT<sup>PlxnD1</sup> activation in the RFO generated highly coordinated bilateral forelimb-orofacial movements that resembled eating (**Fig. 1d-j**,

144 **Extended Data Fig. 2h, Supplementary Video 5).** These movements included jaw opening with  
145 concurrent bilateral (5/13 mice) or unilateral (8/13 mice) hand-to-mouth withdraw, flexing and closing  
146 of the digits of both hands (**Fig. 1e-g, j**). The bilateral forelimb movements may be attributable to the  
147 bilateral projections of ITs<sup>PlxnD1</sup> to the cortex and striatum<sup>38</sup>. At the end of RFO IT<sup>PlxnD1</sup> and PT<sup>Fezf2</sup>  
148 activation, the contralateral hand was invariably moved to a consistent position close to the mouth  
149 regardless of its start positions (**Fig. 1f, h, i**), suggesting that the induced hand movement is mouth  
150 directed. IT<sup>PlxnD1</sup> and PT<sup>Fezf2</sup> activation in a more lateral part of the RFO induced rhythmic jaw  
151 movements along with hand-to-mouth withdraw (**Fig. 1d, i, Extended Data Fig. 2g-l**). The forelimb  
152 and orofacial movements induced by PT<sup>Fezf2</sup> and IT<sup>PlxnD1</sup> activation were robust to different stimulation  
153 frequencies and were induced primarily by long-duration stimulation (500 ms), whereas short-duration  
154 stimulation (100 ms) only induced brief restricted movements (**Fig. 1d, Extended Data Fig. 1g-k**).

155  
156 Because optogenetic stimulation of RFO in *Fezf2;Ai32* and *PlxnD1;Ai32* mice could also activate  
157 axons of passage of ChR2-expressing PNs from other areas, we repeated these experiments using a  
158 viral strategy to express ChR2 specifically in RFO PTs<sup>Fezf2</sup> or ITs<sup>PlxnD1</sup> (**Extended Data Fig. 3a**).  
159 Activating RFO PTs<sup>Fezf2</sup> or ITs<sup>PlxnD1</sup> was sufficient to induce synergistic forelimb and orofacial  
160 movements similar to those observed in *Fezf2;Ai32* and *PlxnD1;Ai32* mice (**Extended Data Fig. 3b-**  
161 **i**). Thus, our results reveal a specific cortical area (RFO, **Fig. 1k**), where the activation of PT or IT  
162 PNs induce forelimb-orofacial movements that resemble natural eating behavior.

163  
164 Among the 6 other driver lines we screened, PN<sup>Emx1</sup> activation induced forelimb and orofacial  
165 movements in the most wide-spread cortical areas (**Extended Data Fig. 1a, e, f**). The PN<sup>Thy1-Tg18</sup>  
166 forelimb motor map was diffuse and less topographically organized compared to that of PT<sup>Fezf2</sup> (**Fig. 1d,**  
167 **Extended Data Fig. 1b, e**). Activation of L2/3 ITs<sup>Tbr2-E17</sup> produced motor maps similar to those of  
168 ITs<sup>PlxnD1</sup>, but the movements were weaker (**Fig. 1d, Extended Data Fig. 1c, e, f**). CT<sup>Tle4</sup> activation  
169 induced forelimb and orofacial movements mostly in the lateral areas relative to Bregma (**Extended**  
170 **Data Figs. 1d-f**). Neither PTs<sup>Tcerg11</sup> nor PTs<sup>Sema3E</sup> induced significant movements (**Extended Data Fig.**  
171 **1e, f**).

### 173 **RFO IT<sup>PlxnD1</sup> activation induces fictive eating with coordinated body and oromanual movements**

174 To further explore the role of RFO in coordinating whole body movements associated with eating, we  
175 stimulated RFO PTs<sup>Fezf2</sup> and ITs<sup>PlxnD1</sup> in freely-moving mice. PT<sup>Fezf2</sup> activation induced a shoulder  
176 adduction that raised the contralateral hand toward the body midline, with associated hand supination  
177 and digit flexion. In addition, a concurrent ipsiversive head turning and lowering brought the snout to  
178 contact the radial surface of the left hand, while the ipsilateral hand maintained body support (**Fig. 1l-o,**  
179 **Supplementary Video 6**). Activation of RFO ITs<sup>PlxnD1</sup> induced a sitting posture and concomitant  
180 bilateral shoulder adduction that brought both hands to the body midline. During the adduction, the  
181 digits flexed and closed and contacted the mouth (**Fig. 1l-o, Supplementary Video 7**). These results  
182 reveal that RFO PNs, ITs<sup>PlxnD1</sup> in particular, mediate whole body movements for eating as well as the  
183 head, mouth, forelimb, hand, and digit movements of eating. Compared with head-fixed stimulation,  
184 RFO PT<sup>Fezf2</sup> and IT<sup>PlxnD1</sup> stimulation in free-moving mice had a lower probability of inducing hand-to-  
185 mouth movement but a high probability of inducing head-to-hand movements (**Fig. 1j, p, q**). Together,  
186 these results indicate that RFO-induced movements bring together the hand and the mouth (i.e., instead

of bringing the hand to the mouth as in head-fixed mice) and this goal can be achieved in different ways according to behavioral context.

### **Pasta eating requires oromaneal dexterity and coordination in food handling**

To explore the role of RFO in food handling and eating, we established a behavioral task, a “Mouse Restaurant”, in which mice retrieve and consume food items (**Fig. 2a, Extended Data Fig. 4a-d, Supplementary Video 8**). This setup featured automated, self-initiated trials (including automated food item delivery) that enable efficient testing of animals with minimal experimenter involvement (**Extended Data Fig. 4a-c**). Behavior was filmed by 3-synchronized video cameras, together with concurrent sound recording that allowed registering the biting events associated with oromaneal movements (**Fig. 2a, Extended Data Fig. 4a, e**). In the task, mice were able to manipulate and eat different kinds of food items (pellets, angel-hair pasta, sunflower seeds, oats, etc.) largely without training (**Supplementary Videos 9, 10**) and learned to shuttle between the waiting and dining areas within 1-3 sessions (see Methods). Amongst food items tested, the angel-hair pasta presented several advantages. It has a consistent shape and length (15 mm), when bitten the sound is audible, and pasta-eating behavior has been previously characterized<sup>41-44</sup>. The Mouse Restaurant provided recordings of thousands of trials and millions of video frames of pasta-eating behavior. Using DeepLabCut<sup>45</sup>, we labeled 12,623 images to track 10 body parts of the eating mice and three parts of the pasta. These included the left and right eyes, hands, ankles, nose, tongue, jaw, and tail base and the top, center, and bottom of the pasta (**Fig. 2b, Supplementary Video 11**). We analyzed over 4 million video frames to identify and annotate re-used units of movement, the action motifs<sup>21</sup>, and sensorimotor events (**Extended data Fig. 5**). We then designed an actogram, which presents overlays of the location and action of key body parts and sensorimotor events, and co-registered biting events across an entire trial in a single graph (**Fig. 2c**).

The angel-hair pasta eating behavior was organized into several stages, each comprising multiple characteristic action motifs involving multiple body parts (**Fig. 2c, d**). Upon entering the dining area, mice *approach* the pasta and most often *retrieve* it from the floor by licking and then grasping it with the teeth (**Fig. 2c, d, Extended Data Figs. 4d, 5a, b**). They then immediately adopt a *sitting posture* on the haunches and subsequently transfer the pasta to their hands with both hands reaching for it (**Fig. 2c, d, Extended Data Fig. 5c, d**). The mice consume the pasta in repeated *handle-eat* bouts (**Fig. 2c, d**). After a piece of pasta is eaten, the mice *leave* the dining area.

The *handle-eat* bout was characterized by highly coordinated and dexterous manipulatory movements, with continual oromaneal movements to appropriately position the pasta for eating. Each bout started with a hand withdraw that brought pasta to the opening mouth (**Fig. 2c, d, Extended Data Fig. 5e**). Hand movements resulted in a mouse using specialized grasp movements with each hand. One hand made a guide grasp, which held proximal end of the pasta in the mouth, most likely by pressing the pasta with the thumb. The other hand made a support grasp, in which the tips of the digits held the pasta more distally from the mouth and directed the pasta further into the mouth after each bite<sup>43</sup> (**Fig. 2b**). To advance the pasta into the mouth as it was reduced by biting, mice made frequent release and re-grasp movements with one or both hands to reposition the hand on the pasta (**Fig. 2c, d, Extended Data Fig. 5f, g**). These hand adjustments most often occurred just

230 before the first bite of each bout in order to position the pasta between the teeth for the bite (**Fig. 2c,**  
231 **e, Extended Data Fig. 6a**). Frame-by-frame analysis further revealed that mice tended to make hand  
232 adjustments with pasta clenched by the mouth (**Fig. 2d, f, Extended Data Figs. 5f, g, 6b**),  
233 suggesting cooperative oromaneal movements for pasta positioning, usually with a characteristic  
234 oblique angle between the hands and the teeth (**Fig. 2d**).

235  
236 Analysis of hand movements shortly before and after biting revealed a rapid downward movement of  
237 both hands before a bite, suggesting that the hands exert a fulcrum-like action on the pasta to aid the  
238 bite (**Fig. 2g, h, Extended Data Fig. 6c-e**). A movement phase analysis uncovered that pasta biting  
239 was achieved by a cooperative hand and jaw action that *snapped* the pasta, producing an audible  
240 snapping sound (**Fig. 2i-l**). Pasta that was snapped from the stem was then chewed (**Fig. 2d**). Thus,  
241 pasta insertion into the mouth, positioning after insertion, and biting all involved coordinated  
242 movements between both the hands and the mouth (**Fig. 2d**). The various movements of eating can  
243 be described as action motifs (pick-up, sit and transfer to hands, withdraw toward the mouth, handle  
244 and bite, chew) because although varying from pasta to pasta and for each pasta as it is reduced in  
245 length with each bite, they are always recognizable and measurable.

### 246 **RFO is necessary for hand recruitment and oromaneal manipulation in pasta eating**

247 To determine whether RFO was involved in pasta eating, we suppressed neural activity by bilateral  
248 infusion of GABA<sub>A</sub> receptor agonist, muscimol (**Extended Data Fig. 7a, b**). Following infusion, the  
249 mice were able to approach and locate the pasta in a seemingly normal way, but they showed deficits  
250 in grasping the pasta by licking (**Extended Data Fig. 7c-f**). For mice that managed to grasp the pasta  
251 by mouth and adopted a sitting posture, their hand recruitment was severely impaired. They usually  
252 failed to manipulate the pasta into a proper orientation for mouth grasping and biting. In attempting  
253 to eat, they displayed a hunched posture related to their difficulty with oromaneal movements, and  
254 frequently dropped the pasta during consumption (**Fig. 2m-o, Extended Data Fig. 7c, d,**  
255 **Supplementary Video 12**). One mouse didn't adopt a sitting posture and consumed all of the pasta  
256 from the floor using only its mouth (**Extended Data Fig. 7g, Supplementary Video 13**). These  
257 impairments resulted in mice taking significantly longer to eat (**Fig. 2m, Extended Data Fig. 7c, d**),  
258 losing the pasta (e.g. pasta was thrown out of the dining area due to clumsiness of oromaneal  
259 movements), or leaving the dining area without finishing a piece of pasta. On the other hand, there  
260 were no deficits in hand grip force and bite force (**Extended Data Fig. 7h**). Together, these results  
261 indicate that RFO contributes to multiple movement modules from sitting posture to hand  
262 recruitment and oromaneal coordination that are together required for coordinated eating behavior.

### 263 **RFO neural activity correlate with oromaneal pasta manipulation**

264 To examine neural activity patterns within the RFO during pasta eating in freely-moving mice, we used  
265 fiber photometry to record population calcium dynamics from PTs<sup>Fezf2</sup> or ITs<sup>PlxnD1</sup> in the right RFO and,  
266 as a comparison, the left aCFA - an area involved in forelimb movement (**Fig. 3a-d, Supplementary**  
267 **Videos 14, 15**). PT<sup>Fezf2</sup> and IT<sup>PlxnD1</sup> activity patterns were broadly similar, we thus refer to their activity  
268 together as PN<sup>Fezf2/PlxnD1</sup> (**Fig. 3c, d**). As mice entered the dining area (marked by stepping across an  
269 elevated bar, **Fig. 2a**) to approach the pasta, PN<sup>Fezf2/PlxnD1</sup> activity in aCFA was higher than that in RFO,  
270 suggesting a role of aCFA in locomotion (**Extended Data Fig. 8**). Immediately following retrieval, as  
271  
272

273 mice took a sitting posture and transferred the pasta from the mouth to the hands, RFO PN<sup>Fezf2/PlxnD1</sup>  
274 activity sharply increased and then fell and rose in proportion to food handling vigor (**Fig. 3c-f, h, i**).  
275 During the same period, aCFA PN<sup>Fezf2/PlxnD1</sup> activity decreased to baseline levels (i.e., levels when mice  
276 were resting in the waiting area; **Fig. 3c, d, f, i**). After the pasta was consumed and as a mouse left the  
277 dining area, RFO activity dropped whereas aCFA activity increased (**Fig. 3c, d**).

278  
279 We next analyzed RFO PT<sup>Fezf2</sup> and IT<sup>PlxnD1</sup> activity patterns during the handle-bite periods and the  
280 chewing periods that were automatically identified by using a hidden Markov model (**Extended Data**  
281 **Fig. 9**). We found that elevated RFO PT<sup>Fezf2</sup> and IT<sup>PlxnD1</sup> activity was specifically correlated with  
282 handle-bite periods (**Fig. 3e, g, h, j**). The RFO activity increase was best correlated with the pasta  
283 positioning movement of getting pasta into the mouth but was not related to the movement of removing  
284 the pasta from the mouth after a bite (**Fig. 3e, g, h, j**). Both PT<sup>Fezf2</sup> and IT<sup>PlxnD1</sup> activity rose after the  
285 onset of hand withdraw, with a shorter delay for ITs<sup>PlxnD1</sup> compared to that for PTs<sup>Fezf2</sup> (**Fig. 3g, j, k**),  
286 indicating that IT<sup>PlxnD1</sup> activity leads PT<sup>Fezf2</sup> activity in each handle-eat bout. In addition, a cross-  
287 correlation analysis revealed that the elevation of RFO activity reliably followed hand withdraw,  
288 measured as decreasing hand-to-nose distance (**Fig. 3l, m**), suggesting that PN<sup>Fezf2/PlxnD1</sup> activity was  
289 associated with controlling oromaneal movements during the handle-bite period. Importantly, the  
290 correlation coefficient of IT<sup>PlxnD1</sup> activity was significantly higher than that of PT<sup>Fezf2</sup> activity (**Fig. 3m**),  
291 suggesting that ITs<sup>PlxnD1</sup> may compose an overarching sensorimotor program of oromaneal manipulation  
292 whereas PTs<sup>Fezf2</sup> may broadcast commands for the execution of specific actions. RFO activity increase  
293 was also correlated with hand adjustments that advanced the pasta for a bite and with pasta  
294 biting/snapping (**Fig. 3e, g, h, j**). Activity declined sharply during chewing (**Fig. 3e, g, h, j**). Together,  
295 these results indicate that RFO PT<sup>Fezf2</sup> and IT<sup>PlxnD1</sup> activity are associated with the oromaneal  
296 movements of positioning the pasta in the mouth and of biting it, and IT<sup>PlxnD1</sup> activity likely initiates the  
297 coordinated oromaneal movements for food handling.

298  
299 To further clarify whether RFO PN<sup>Fezf2/PlxnD1</sup> activity were associated with oromaneal coordination or  
300 with eating using mouth only, we fed mice 1-mm long pieces of angel-hair pasta, which were eaten  
301 without sitting up and handling (**Fig. 3n, q, Supplementary Videos 16, 17**). RFO PT<sup>Fezf2</sup> and IT<sup>PlxnD1</sup>  
302 activity rose immediately as the mice picked up the pasta by mouth but then quickly decreased to  
303 baseline with chewing (**Fig. 3n-s**). These results indicate that RFO PT<sup>Fezf2</sup> and IT<sup>PlxnD1</sup> activity are  
304 associated with coordinated mouth and hand movements of inserting pasta into the mouth and  
305 manipulating the pasta, in addition to eating with mouth.

### 307 **Division of labor between RFO PN types in oromaneal manipulation**

308 To examine the role of RFO PN types in pasta eating, we suppressed the activity of all projection  
309 neurons (PNs<sup>Emx1</sup>), pyramidal tract neurons (PTs<sup>Fezf2</sup>), or intratelencephalic neurons (ITs<sup>PlxnD1</sup>) at  
310 different stages of the pasta-eating behavior (**Fig. 4a, Extended Data Fig. 10a**). Bilateral inhibition  
311 of these PN types as the mice approached the pasta did not perturb the approach (**Fig. 4b, Extended**  
312 **Data Fig. 10b**). Inhibition of PNs<sup>Emx1</sup> or PTs<sup>Fezf2</sup>, but not ITs<sup>PlxnD1</sup>, delayed pasta pick-up and  
313 increased lick attempts (**Fig. 4b-d, Supplementary Videos 18-20**), likely due to impairments in  
314 tongue grasp movements. Following mouth pick-up and transfer of pasta to the hands, inhibition of  
315 PNs<sup>Emx1</sup> and ITs<sup>PlxnD1</sup>, but not PTs<sup>Fezf2</sup>, significantly increased the time taken to make the first bite

(Fig. 4b, e). This was due to uncoordinated pasta orienting with the hands and difficulty in making mouth grasp of the pasta (Fig. 4b, Extended Data Fig. 10c, d).

Bilateral PN inhibition during the handle-eat stage significantly reduced and delayed pasta biting (Fig. 4a, f, g). The deficit was not due to an impairment in biting *per se*. When we presented pasta to the mice in a holding device so that the mice could bite without using their hands, RFO PN inhibition did not interfere with pasta biting (Extended Data Fig. 11, Supplementary Videos 21-23). Multi-faceted quantitative analysis revealed that the deficit of RFO PN inhibition was in oromaneal coordination of positioning the pasta in the mouth and of applying force to snap it (Fig. 4h-p).

Inhibition of  $PNs^{Emx1}$  or  $ITs^{PlxnD1}$  during the handle-eat stage produced excessive and uncoordinated hand movements, including unproductive bimanual adjustments (Fig. 4f, h, Supplementary Videos 24, 25), which led to increased but ineffective pasta orientation changes before it was grasped in the mouth (Extended Data Fig. 10e). Four of six *Emx1* mice were unable to position pasta for a single bite during inhibition (Fig. 4f, g). The difficulty in orienting the pasta was confirmed by more variable ( $PNs^{Emx1}$ ) and more vertical orientations ( $PTs^{Fezf2}$  and  $ITs^{PlxnD1}$ ) for pasta positioning (Fig. 4i, j). Furthermore,  $PT^{Fezf2}$  and  $IT^{PlxnD1}$  inhibition altered the pasta holding position of the support hand at the time of biting (Fig. 4k, l, Supplementary Videos 26, 27), resulting in more vertical pasta bite orientations (Fig. 4k, m, Extended Data Fig. 12). The pasta bite relied critically on the movements of incisors, as the mice always used their incisors to bite even under PN inhibition (Extended Data Fig. 13). Finally, PN inhibition disrupted the coordination between the bite and hand movement (i.e., the phase relationship) for snapping the pasta. With respect to the phase of the hand and mouth movements for snapping pasta,  $PT^{Fezf2}$  inhibition resulted in delayed bite in relation to downward hand movement and  $IT^{PlxnD1}$  inhibition resulted in increased variability of this phase relationship (Fig. 4n-p). Altogether, these results indicate that  $PNs^{Emx1}$ ,  $PTs^{Fezf2}$ , and  $ITs^{PlxnD1}$  in the RFO orchestrate the online coordination of oromaneal manipulation in positioning the pasta in the mouth and for snapping the pasta.

### RFO PN input-output connectivity patterns reveal cortical and brain networks for oromaneal coordination

To explore RFO-centered brain circuits that contribute to oromaneal manipulation for eating, we examined brain-wide input-output connectivity patterns of  $ITs^{PlxnD1}$  and  $PTs^{Fezf2}$ . Anterograde tracing revealed that  $ITs^{PlxnD1}$  project bilaterally to primary and secondary motor (MOp, MOs) and sensory (SSp, SSs) orofacial (especially mouth) and forelimb (especially upper limb) areas, and to dorsal agranular insular cortex (AId), visceral cortex (VISC), and the capsular part of the central amygdala nucleus (CEAc) (Fig. 5a, b, e, Extended Data Fig. 14a, b, d, Supplementary Video 28).  $ITs^{PlxnD1}$  also project bilaterally to the ventrolateral striatum (Fig. 5b, e, Extended Data Fig. 14b, d), a region implicated in feeding and food handling<sup>46-48</sup>. In contrast,  $PTs^{Fezf2}$  have sparse axon projections to other cortical regions and striatum but project prominently to multiple ipsilateral or contralateral subcortical targets in the thalamus, lateral superior colliculus (ISC), pons, and medulla (Fig. 5b, e, Extended Data Fig. 14b-d, Supplementary Video 29). This projection crosses at the pyramidal decussation to innervate the spinal cord (Extended Data Fig. 14c). The brainstem targets of  $PTs^{Fezf2}$  include multiple command centers for forelimb and orofacial actions such as reaching (PARN)<sup>49,50</sup>, grasping (PARN,

MDRN)<sup>49-51</sup>, jaw opening (PSV, SPV, IRN)<sup>52-54</sup>, licking (PSV, SPV, IRN)<sup>52-54</sup>, and whisking (PSV, SPV, IRN)<sup>53-55</sup>.

Retrograde monosynaptic rabies tracing revealed that cortical inputs to ITs<sup>PlxnD1</sup> and PTs<sup>Fezf2</sup> of the RFO derived almost exclusively from their projection targets (i.e., forelimb and orofacial sensorimotor areas, AId, and VISC; **Fig. 5c-e, Extended Data Fig. 15a, b, d, f, Supplementary Videos 30, 31**). In addition, ITs<sup>PlxnD1</sup> and PTs<sup>Fezf2</sup> receive major subcortical inputs from the thalamus, including the ventral anterior-lateral complex and posterior complex (**Fig. 5d, e, Extended Data Fig. 15b, e, f**). Another weak yet reliable subcortical input source is the external segment of the globus pallidus (**Extended Data Fig. 15c, f**).

Collectively, these results reveal several hallmarks of RFO connectivity. Within the cortex, RFO forms a reciprocally connected network involving primary and secondary forelimb and orofacial sensorimotor areas as well as insular and visceral areas, and receives additional inputs from the thalamus and basal ganglia. Whereas ITs<sup>PlxnD1</sup> target the ventrolateral striatum, thereby contributing to a cortico-striatal-thalamic loop, PTs<sup>Fezf2</sup> broadcast cortical outputs to all levels of the subcortical structures. This RFO-centered brain network appears well suited to coordinate motor actions across multiple body parts according to online multi-modal sensory inputs (somatosensory and visceral for taste quality) for orchestrating food manipulation during eating. The involvement of VISC and CEAc might further engage valence, incentive, and emotional systems associated with eating.

## DISCUSSION

We have examined the cortical circuit contribution to a naturalistic behavior with inherent ethological relevance, mouse manipulating and eating diverse food items of various configurations and textures. Eating took place in a Mouse Restaurant that provided three dimensional filming and sound recording for capturing, analyzing, and understanding this complex freely-moving behavior. Our analysis describes pasta eating as a sequence of readily identifiable stages, each comprising recognizable action motifs. Our analyses revealed microscale fast movements of hand adjustments, oromanual manipulation, and biting in the context of a macroscale action sequence comprising food retrieval and eating. Because oromanual movements are conserved within rodents and primates<sup>3,4,56</sup>, the results are relevant to understanding the complexity of primate and human oromanual movements. Although pose estimation algorithms, such as DeepLabCut<sup>45</sup>, can automate the tracking of body parts that are visible, occluded body parts and fine scale movements of the digits are prone to tracking errors. Other challenges include identifying interpretable action motifs and accurately delineating their time course and relationships. Our manual annotation of action motifs from over 4 million video frames presented in the form of actograms provide a ground truth and publicly accessible dataset, which should inspire future machine learning algorithms. Future incorporation of X-ray based fluoroscopy<sup>57</sup> may further capture internal oral actions of the tongue, teeth, and jaw movements. As natural behavior is the “language” of the brain, an understanding of the organization of its syllables and grammar provides a pathway to exploring its neural circuits<sup>21,22,58</sup>.

402  
403 Lesion<sup>59,60</sup>, anatomical<sup>61-63</sup>, and physiological<sup>64</sup> studies have focused on the role of primary (M1)  
404 and secondary (M2) motor cortices in control of relatively isolated and well-trained forelimb  
405 movements (e.g. reach and grasp) in primates<sup>61,65</sup> and rodents<sup>66</sup>. These studies have revealed  
406 correlations of cortical neuron activity with a range of movement parameters (e.g. force<sup>13,15</sup> and  
407 kinematics<sup>14,67</sup>) and have suggested motor cortex as a dynamic system for activity pattern generation  
408<sup>68</sup>. Nevertheless, the role of cortical networks beyond M1 and M2 and the cellular and circuitry basis  
409 in orchestrating more complex ethological behaviors in freely moving animals, such as oromanual  
410 coordination to place food in the mouth and to manipulate food for biting, have remained poorly  
411 understood. Leveraging mouse genetic tools<sup>38</sup>, our optogenetic screen with PN-type resolution  
412 across the dorsal cortex combined with a non-hypothesis driven assay of forelimb and orofacial  
413 movements revealed the RFO and its role in food manipulation. Previous studies of rodent cortex  
414 have characterized the anterolateral and more posteromedial areas (ALM and CFA) that control  
415 separate orofacial, lick<sup>69,70</sup> vs forelimb reaching<sup>71</sup> movements, in head-fixed animals. The  
416 juxtaposition of RFO between these two distinct areas suggests its plausible origin, an evolutionary  
417 expansion and overlap of orofacial and forelimb areas shaping a novel area with distinct connectivity  
418 patterns to both orofacial and forelimb sensorimotor areas that support a novel behavioral function.  
419 In this respect it is noteworthy that stimulation of the macaque precentral gyrus, a region juxtaposed  
420 between mouth and hand motor areas, also induces coordinated oromanual movements<sup>30</sup> and the  
421 human precentral gyrus contains neurons that respond to mouth stimuli and elicit concurrent hand-  
422 to-mouth and mouth movements when stimulated<sup>72</sup>. Together, these findings suggest that a  
423 conserved RFO contributes to the food manipulation behavior in rodents and primates including  
424 humans.

425  
426 Among diverse cortical PN classes, IT and PT manifest distinct molecular, anatomical, and  
427 physiological properties and represent intracortical processing streams and subcortical output  
428 channels, respectively<sup>73</sup>. Leveraging reliable genetic access to ITs<sup>PlxnD1</sup> and PTs<sup>Fezf2</sup> in combination  
429 with fine-grained quantitative analysis of an ethological behavior, here we reveal categorical  
430 distinctions of IT and PT functions that are highly congruent with and rooted in their anatomical  
431 distinctions. As a main RFO output channel, PTs<sup>Fezf2</sup> mainly project unilaterally to multiple  
432 subcortical, especially brainstem and spinal, areas implicated in regulating forelimb and orofacial  
433 actions<sup>35,50,53</sup>. Within the RFO local circuitry, ITs<sup>PlxnD1</sup> likely provide excitatory inputs to PTs<sup>Fezf2</sup> as  
434 ITs are overall upstream of PTs<sup>73,74</sup>. More importantly, ITs<sup>PlxnD1</sup> project bilaterally to several other  
435 cortical areas and the ventrolateral striatum, which together may constitute a forelimb-orofacial  
436 corticostriatal sensorimotor network. Consistent with this overarching anatomical framework, PT<sup>Fezf2</sup>  
437 activation induced contralateral and relatively limited forelimb-orofacial movements. In contrast,  
438 IT<sup>PlxnD1</sup> activation elicited bilateral and highly concerted movements that integrate body posture with  
439 head, orofacial, forelimb, and digit movements that constitute fictive eating. This is likely achieved  
440 by recruiting the extended RFO network that includes forelimb and orofacial sensory and motor  
441 areas. Furthermore, whereas PT<sup>Fezf2</sup> inhibition mainly disrupted the execution of skilled oral (e.g.  
442 lick-to-retrieve) and forelimb actions, IT<sup>PlxnD1</sup> inhibition predominantly disrupted oromanual  
443 coordination. We interpret the lack of a complete impairment of oromanual manipulation by RFO  
444 PN inhibition to reflect that a distributed network involving multiple other areas supports this

445 behavior; and redundancy in the network controlling such a fundamental behavior would be highly  
446 adaptive, as shown in other motor behaviors<sup>69,75</sup>.

447  
448 Notably, PTs<sup>Fezf2</sup> and ITs<sup>PlxnD1</sup> receive inputs from common thalamic and cortical areas, suggesting  
449 their coordinated modulation by multi-sensory feedback and motor efference within an RFO-  
450 centered cortical network. Thus, contrary to lower-level brainstem command centers that mostly  
451 elicited isolated and relatively stereotyped actions and were modulated by local somatosensory  
452 inputs from within the same body part<sup>11,53</sup>, RFO PN receive multi-modal sensory inputs, process  
453 sensorimotor information within an extended cortico-striatal-thalamic network, and broadcast  
454 outputs across subcortical levels to coordinate movements across the body toward orchestrating a  
455 dexterous ethological behavior. Importantly, compared with PT<sup>Fezf2</sup>, IT<sup>PlxnD1</sup> activity in RFO rose  
456 earlier after hand withdraw and was more strongly correlated with handle-bite periods, suggesting its  
457 crucial role in coordinating oromanual movements for pasta manipulation and biting. Thus it is  
458 possible that ITs<sup>PlxnD1</sup> may select, coordinate, and monitor an overarching feeding program, while  
459 PTs<sup>Fezf2</sup> contribute to the implementation of fine movements. Future work could reveal whether the  
460 feeding network described here contributes to the many other rodent behaviors that involve hand  
461 mouth cooperation, including self-grooming, pup cleaning, nest building, and play.

462  
463 Our work establishes an experimental paradigm for exploring the neural circuitry underlying  
464 dexterous sensorimotor control in unconstrained animals, with implications for studying primate  
465 dexterity<sup>76</sup> and robotic manipulation<sup>77</sup>. We reveal the circuitry implementation of a neural  
466 architecture that reflects several core principles of hierarchical motor control<sup>10</sup>. Indeed, partial  
467 autonomy of brainstem command centers, information factorization between brainstem and cortical  
468 controllers, amortized higher level control, and inter-region communication may together facilitate  
469 multi-joint, full-scale body control. This neural architecture is well suited for generating a robust,  
470 flexible, and versatile behavioral repertoire toward achieving ethological goals under variable and  
471 changing circumstances. Future work could explore whether similar neural circuitry may mediate  
472 other complex behaviors in which animals coordinate the action of different body parts, including  
473 serial action of human hand and mouth movements used for the languages<sup>6,7</sup>.

## 474 475 476 477 **ACKNOWLEDGMENTS**

478 We thank Yongjun Qian for making the GtACR1 AAV vector and virus; Joshua Hatfield for helping  
479 with STP imaging and video annotations; Priscilla Wu, Joshua Hatfield, and Bao-Xia Han for animal  
480 preparation and maintenance; Robert Eifert at the machine shop of CSHL for the fabrication of  
481 custom-designed parts; and William Galbavy, Shreyas M. Suryanarayana, and Jason Tucciarone for  
482 helpful discussions. We thank Richard Mooney for comments on the manuscript. This work was  
483 supported in part by NIMH grants 1DP1MH129954-01 and 5U19MH114821-03 to Z.J.H.

## 484 485 486 **AUTHOR CONTRIBUTIONS**

487 X.A. and Z. J. H. conceived this study. Z.J.H. supervised the study. X.A. designed the research and  
488 performed the majority of the experiments, and analyzed data. K.M. performed STP imaging and  
489 anatomy analyses. Y.L. performed in vivo electrophysiology recording. H.M. provided advice for

490 data analysis. X.H.X. analyzed behavioral videos. A.K. and I.Q.W. made contributions to data  
491 analysis and discussion. Z.J.H. and X.A. wrote the manuscript with inputs from I.Q.W. and A.K.  
492  
493  
494

## 495 REFERENCES

- 496  
497  
498  
499
- 500 1 Iwaniuk, A. N. & Whishaw, I. Q. On the origin of skilled forelimb movements. *Trends Neurosci* **23**,  
501 372-376 (2000). [https://doi.org/10.1016/s0166-2236\(00\)01618-0](https://doi.org/10.1016/s0166-2236(00)01618-0)
  - 502 2 Sustaita, D. *et al.* Getting a grip on tetrapod grasping: form, function, and evolution. *Biol Rev Camb*  
503 *Philos Soc* **88**, 380-405 (2013). <https://doi.org/10.1111/brv.12010>
  - 504 3 Whishaw, I. Q. a. K., J.M. in *Feeding in Vertebrates: Evolution, Morphology, Behavior,*  
505 *Biomechanics* Ch. 6, 159-186 (Springer, 2019).
  - 506 4 Hirsche, L. A., Cenni, C., Leca, J.-B. & Wishaw, I. Q. Two Types of Withdraw-to-Eat Movement  
507 Related to Food Size in Long-Tailed Macaques (*Macaca fascicularis*): Insights into the Evolution of  
508 the Visual Control of Hand Shaping in Anthropoid Primates. *Animal Behavior and Cognition* **9**, 176-  
509 195 (2022). <https://doi.org/10.26451/abc.09.02.02.2022>
  - 510 5 Barrett, J. M., Raineri Tapias, M. G. & Shepherd, G. M. G. Manual dexterity of mice during food-  
511 handling involves the thumb and a set of fast basic movements. *PLoS One* **15**, e0226774 (2020).  
512 <https://doi.org/10.1371/journal.pone.0226774>
  - 513 6 Kolodny, O. & Edelman, S. The problem of multimodal concurrent serial order in behavior.  
514 *Neuroscience & Biobehavioral Reviews* **56**, 252-265 (2015).  
515 [https://doi.org:https://doi.org/10.1016/j.neubiorev.2015.07.009](https://doi.org/https://doi.org/10.1016/j.neubiorev.2015.07.009)
  - 516 7 Lashley, K. S. *The problem of serial order in behavior*. Vol. 21 (Bobbs-Merrill Oxford, 1951).
  - 517 8 Suryanarayana, S. M., Robertson, B. & Grillner, S. The neural bases of vertebrate motor behaviour  
518 through the lens of evolution. *Philos Trans R Soc Lond B Biol Sci* **377**, 20200521 (2022).  
519 <https://doi.org/10.1098/rstb.2020.0521>
  - 520 9 Arber, S. & Costa, R. M. Connecting neuronal circuits for movement. *Science* **360**, 1403-1404  
521 (2018). <https://doi.org/10.1126/science.aat5994>
  - 522 10 Merel, J., Botvinick, M. & Wayne, G. Hierarchical motor control in mammals and machines. *Nat*  
523 *Commun* **10**, 5489 (2019). <https://doi.org/10.1038/s41467-019-13239-6>
  - 524 11 Arber, S. & Costa, R. M. Networking brainstem and basal ganglia circuits for movement. *Nat Rev*  
525 *Neurosci* **23**, 342-360 (2022). <https://doi.org/10.1038/s41583-022-00581-w>
  - 526 12 Churchland, M. M. *et al.* Neural population dynamics during reaching. *Nature* **487**, 51-56 (2012).  
527 <https://doi.org/10.1038/nature11129>
  - 528 13 Evarts, E. V. Pyramidal tract activity associated with a conditioned hand movement in the monkey. *J*  
529 *Neurophysiol* **29**, 1011-1027 (1966). <https://doi.org/10.1152/jn.1966.29.6.1011>
  - 530 14 Georgopoulos, A. P., Kalaska, J. F., Caminiti, R. & Massey, J. T. On the relations between the  
531 direction of two-dimensional arm movements and cell discharge in primate motor cortex. *J Neurosci*  
532 **2**, 1527-1537 (1982).
  - 533 15 Kakei, S., Hoffman, D. S. & Strick, P. L. Muscle and movement representations in the primary  
534 motor cortex. *Science* **285**, 2136-2139 (1999). <https://doi.org/10.1126/science.285.5436.2136>
  - 535 16 Galinanes, G. L., Bonardi, C. & Huber, D. Directional Reaching for Water as a Cortex-Dependent  
536 Behavioral Framework for Mice. *Cell Rep* **22**, 2767-2783 (2018).  
537 <https://doi.org/10.1016/j.celrep.2018.02.042>
  - 538 17 Hyland, B. Neural activity related to reaching and grasping in rostral and caudal regions of rat motor  
539 cortex. *Behav Brain Res* **94**, 255-269 (1998). [https://doi.org/10.1016/s0166-4328\(97\)00157-5](https://doi.org/10.1016/s0166-4328(97)00157-5)

- 540 18 Miri, A. *et al.* Behaviorally Selective Engagement of Short-Latency Effector Pathways by Motor  
541 Cortex. *Neuron* **95**, 683-696 e611 (2017). <https://doi.org/10.1016/j.neuron.2017.06.042>
- 542 19 Sauerbrei, B. A. *et al.* Cortical pattern generation during dexterous movement is input-driven.  
543 *Nature* **577**, 386-391 (2020). <https://doi.org/10.1038/s41586-019-1869-9>
- 544 20 Wang, X. *et al.* Deconstruction of Corticospinal Circuits for Goal-Directed Motor Skills. *Cell* **171**,  
545 440-455 e414 (2017). <https://doi.org/10.1016/j.cell.2017.08.014>
- 546 21 Datta, S. R., Anderson, D. J., Branson, K., Perona, P. & Leifer, A. Computational Neuroethology: A  
547 Call to Action. *Neuron* **104**, 11-24 (2019). <https://doi.org/10.1016/j.neuron.2019.09.038>
- 548 22 Miller, C. T. *et al.* Natural behavior is the language of the brain. *Curr Biol* **32**, R482-R493 (2022).  
549 <https://doi.org/10.1016/j.cub.2022.03.031>
- 550 23 Galvin, L., Mirza Agha, B., Saleh, M., Mohajerani, M. H. & Whishaw, I. Q. Learning to cricket hunt  
551 by the laboratory mouse (*Mus musculus*): Skilled movements of the hands and mouth in cricket  
552 capture and consumption. *Behav Brain Res* **412**, 113404 (2021).  
553 <https://doi.org/10.1016/j.bbr.2021.113404>
- 554 24 Gu, Z. *et al.* Control of species-dependent cortico-motoneuronal connections underlying manual  
555 dexterity. *Science* **357**, 400-404 (2017). <https://doi.org/10.1126/science.aan3721>
- 556 25 Whishaw, I. Q., Sarna, J. R. & Pellis, S. M. Evidence for rodent-common and species-typical limb  
557 and digit use in eating, derived from a comparative analysis of ten rodent species. *Behav Brain Res*  
558 **96**, 79-91 (1998). [https://doi.org/10.1016/s0166-4328\(97\)00200-3](https://doi.org/10.1016/s0166-4328(97)00200-3)
- 559 26 Barrett, J. M., Martin, M. E. & Shepherd, G. M. G. Manipulation-specific cortical activity as mice  
560 handle food. *Current Biology* **32**, 4842-4853.e4846 (2022).  
561 [https://doi.org:https://doi.org/10.1016/j.cub.2022.09.045](https://doi.org/https://doi.org/10.1016/j.cub.2022.09.045)
- 562 27 Huang, Z. J. Toward a genetic dissection of cortical circuits in the mouse. *Neuron* **83**, 1284-1302  
563 (2014). <https://doi.org/10.1016/j.neuron.2014.08.041>
- 564 28 Luo, L., Callaway, E. M. & Svoboda, K. Genetic Dissection of Neural Circuits: A Decade of  
565 Progress. *Neuron* **98**, 256-281 (2018). <https://doi.org/10.1016/j.neuron.2018.03.040>
- 566 29 PENFIELD, W. & BOLDREY, E. SOMATIC MOTOR AND SENSORY REPRESENTATION IN  
567 THE CEREBRAL CORTEX OF MAN AS STUDIED BY ELECTRICAL STIMULATION1. *Brain*  
568 **60**, 389-443 (1937). <https://doi.org/10.1093/brain/60.4.389>
- 569 30 Graziano, M. S., Taylor, C. S. & Moore, T. Complex movements evoked by microstimulation of  
570 precentral cortex. *Neuron* **34**, 841-851 (2002). [https://doi.org/10.1016/s0896-6273\(02\)00698-0](https://doi.org/10.1016/s0896-6273(02)00698-0)
- 571 31 Stepniewska, I., Fang, P. C. & Kaas, J. H. Microstimulation reveals specialized subregions for  
572 different complex movements in posterior parietal cortex of prosimian galagos. *Proc Natl Acad Sci*  
573 *U S A* **102**, 4878-4883 (2005). <https://doi.org/10.1073/pnas.0501048102>
- 574 32 Brown, A. R. & Teskey, G. C. Motor cortex is functionally organized as a set of spatially distinct  
575 representations for complex movements. *J Neurosci* **34**, 13574-13585 (2014).  
576 <https://doi.org/10.1523/JNEUROSCI.2500-14.2014>
- 577 33 Neafsey, E. J. *et al.* The organization of the rat motor cortex: a microstimulation mapping study.  
578 *Brain Res* **396**, 77-96 (1986). [https://doi.org/10.1016/s0006-8993\(86\)80191-3](https://doi.org/10.1016/s0006-8993(86)80191-3)
- 579 34 Tennant, K. A. *et al.* The organization of the forelimb representation of the C57BL/6 mouse motor  
580 cortex as defined by intracortical microstimulation and cytoarchitecture. *Cereb Cortex* **21**, 865-876  
581 (2011). <https://doi.org/10.1093/cercor/bhq159>
- 582 35 Mercer Lindsay, N. *et al.* Orofacial Movements Involve Parallel Corticobulbar Projections from  
583 Motor Cortex to Trigeminal Premotor Nuclei. *Neuron* **104**, 765-780 e763 (2019).  
584 <https://doi.org/10.1016/j.neuron.2019.08.032>
- 585 36 Hira, R., Terada, S.-I., Kondo, M. & Matsuzaki, M. Distinct Functional Modules for Discrete and  
586 Rhythmic Forelimb Movements in the Mouse Motor Cortex. *The Journal of Neuroscience* **35**, 13311  
587 (2015). <https://doi.org/10.1523/JNEUROSCI.2731-15.2015>

- 588 37 Harrison, T. C., Ayling, O. G. & Murphy, T. H. Distinct cortical circuit mechanisms for complex  
589 forelimb movement and motor map topography. *Neuron* **74**, 397-409 (2012).  
590 <https://doi.org/10.1016/j.neuron.2012.02.028>
- 591 38 Matho, K. S. *et al.* Genetic dissection of the glutamatergic neuron system in cerebral cortex. *Nature*  
592 **598**, 182-187 (2021). <https://doi.org/10.1038/s41586-021-03955-9>
- 593 39 Arenkiel, B. R. *et al.* In vivo light-induced activation of neural circuitry in transgenic mice  
594 expressing channelrhodopsin-2. *Neuron* **54**, 205-218 (2007).  
595 <https://doi.org/10.1016/j.neuron.2007.03.005>
- 596 40 Mayrhofer, J. M. *et al.* Distinct Contributions of Whisker Sensory Cortex and Tongue-Jaw Motor  
597 Cortex in a Goal-Directed Sensorimotor Transformation. *Neuron* **103**, 1034-1043 e1035 (2019).  
598 <https://doi.org/10.1016/j.neuron.2019.07.008>
- 599 41 Allred, R. P. *et al.* The vermicelli handling test: a simple quantitative measure of dexterous forepaw  
600 function in rats. *J Neurosci Methods* **170**, 229-244 (2008).  
601 <https://doi.org/10.1016/j.jneumeth.2008.01.015>
- 602 42 Whishaw, I. Q. & Coles, B. L. Varieties of paw and digit movement during spontaneous food  
603 handling in rats: postures, bimanual coordination, preferences, and the effect of forelimb cortex  
604 lesions. *Behav Brain Res* **77**, 135-148 (1996). [https://doi.org/10.1016/0166-4328\(95\)00209-x](https://doi.org/10.1016/0166-4328(95)00209-x)
- 605 43 Whishaw, I. Q. *et al.* The syntactic organization of pasta-eating and the structure of reach  
606 movements in the head-fixed mouse. *Sci Rep* **7**, 10987 (2017). [https://doi.org/10.1038/s41598-017-](https://doi.org/10.1038/s41598-017-10796-y)  
607 [10796-y](https://doi.org/10.1038/s41598-017-10796-y)
- 608 44 Whishaw, I. Q., Ghasroddashti, A., Mirza Agha, B. & Mohajerani, M. H. The temporal  
609 choreography of the yo-yo movement of getting spaghetti into the mouth by the head-fixed mouse.  
610 *Behav Brain Res* **381**, 112241 (2020). <https://doi.org/10.1016/j.bbr.2019.112241>
- 611 45 Mathis, A. *et al.* DeepLabCut: markerless pose estimation of user-defined body parts with deep  
612 learning. *Nat Neurosci* **21**, 1281-1289 (2018). <https://doi.org/10.1038/s41593-018-0209-y>
- 613 46 Hintiryan, H. *et al.* The mouse cortico-striatal projectome. *Nat Neurosci* **19**, 1100-+ (2016).
- 614 47 Salamone, J. D., Mahan, K. & Rogers, S. Ventrolateral Striatal Dopamine Depletions Impair  
615 Feeding and Food Handling in Rats. *Pharmacol Biochem Be* **44**, 605-610 (1993).
- 616 48 Bakshi, V. P. & Kelley, A. E. Dopaminergic Regulation of Feeding-Behavior .2. Differential-Effects  
617 of Amphetamine Microinfusion into 3 Striatal Subregions. *Psychobiology* **19**, 233-242 (1991).
- 618 49 Ruder, L. & Arber, S. Brainstem Circuits Controlling Action Diversification. *Annu Rev Neurosci* **42**,  
619 485-504 (2019). <https://doi.org/10.1146/annurev-neuro-070918-050201>
- 620 50 Ruder, L. *et al.* A functional map for diverse forelimb actions within brainstem circuitry. *Nature*  
621 **590**, 445-450 (2021). <https://doi.org/10.1038/s41586-020-03080-z>
- 622 51 Esposito, M. S., Capelli, P. & Arber, S. Brainstem nucleus MdV mediates skilled forelimb motor  
623 tasks. *Nature* **508**, 351-356 (2014). <https://doi.org/10.1038/nature13023>
- 624 52 Dempsey, B. *et al.* A medullary centre for lapping in mice. *Nat Commun* **12**, 6307 (2021).  
625 <https://doi.org/10.1038/s41467-021-26275-y>
- 626 53 Stanek, E. t., Cheng, S., Takatoh, J., Han, B. X. & Wang, F. Monosynaptic premotor circuit tracing  
627 reveals neural substrates for oro-motor coordination. *Elife* **3**, e02511 (2014).  
628 <https://doi.org/10.7554/eLife.02511>
- 629 54 Takatoh, J. *et al.* Constructing an adult orofacial premotor atlas in Allen mouse CCF. *Elife* **10**  
630 (2021). <https://doi.org/10.7554/eLife.67291>
- 631 55 Moore, J. D. *et al.* Hierarchy of orofacial rhythms revealed through whisking and breathing. *Nature*  
632 **497**, 205-210 (2013). <https://doi.org/10.1038/nature12076>
- 633 56 Peckre, L. R., Fabre, A.-C., Wall, C. E., Pouydebat, E. & Whishaw, I. Q. Two types of hand  
634 withdraw movement to place food in the mouth mediated by somatosensation in 22-species of  
635 strepsirrhines. *bioRxiv*, 2022.2003.2013.484147 (2022). <https://doi.org/10.1101/2022.03.13.484147>
- 636 57 Lever, T. E. *et al.* Videofluoroscopic Validation of a Translational Murine Model of Presbyphagia.  
637 *Dysphagia* **30**, 328-342 (2015). <https://doi.org/10.1007/s00455-015-9604-7>

- 638 58 Krakauer, J. W., Ghazanfar, A. A., Gomez-Marin, A., MacIver, M. A. & Poeppel, D. Neuroscience  
639 Needs Behavior: Correcting a Reductionist Bias. *Neuron* **93**, 480-490 (2017).  
640 <https://doi.org/10.1016/j.neuron.2016.12.041>
- 641 59 Lawrence, D. G. & Kuypers, H. G. The functional organization of the motor system in the monkey.  
642 I. The effects of bilateral pyramidal lesions. *Brain* **91**, 1-14 (1968).  
643 <https://doi.org/10.1093/brain/91.1.1>
- 644 60 Whishaw, I. Q., Pellis, S. M., Gorny, B., Kolb, B. & Tetzlaff, W. Proximal and distal impairments in  
645 rat forelimb use in reaching follow unilateral pyramidal tract lesions. *Behav Brain Res* **56**, 59-76  
646 (1993). [https://doi.org/10.1016/0166-4328\(93\)90022-j](https://doi.org/10.1016/0166-4328(93)90022-j)
- 647 61 Strick, P. L., Dum, R. P. & Rathelot, J. A. The Cortical Motor Areas and the Emergence of Motor  
648 Skills: A Neuroanatomical Perspective. *Annu Rev Neurosci* **44**, 425-447 (2021).  
649 <https://doi.org/10.1146/annurev-neuro-070918-050216>
- 650 62 Munoz-Castaneda, R. *et al.* Cellular anatomy of the mouse primary motor cortex. *Nature* **598**, 159-  
651 166 (2021). <https://doi.org/10.1038/s41586-021-03970-w>
- 652 63 Lemon, R. N. Descending pathways in motor control. *Annu Rev Neurosci* **31**, 195-218 (2008).  
653 <https://doi.org/10.1146/annurev.neuro.31.060407.125547>
- 654 64 Omrani, M., Kaufman, M. T., Hatsopoulos, N. G. & Cheney, P. D. Perspectives on classical  
655 controversies about the motor cortex. *J Neurophysiol* **118**, 1828-1848 (2017).  
656 <https://doi.org/10.1152/jn.00795.2016>
- 657 65 Georgopoulos, A. P. & Carpenter, A. F. Coding of movements in the motor cortex. *Curr Opin*  
658 *Neurobiol* **33**, 34-39 (2015). <https://doi.org/10.1016/j.conb.2015.01.012>
- 659 66 Warriner, C. L., Fageiry, S. K., Carmona, L. M. & Miri, A. Towards Cell and Subtype Resolved  
660 Functional Organization: Mouse as a Model for the Cortical Control of Movement. *Neuroscience*  
661 **450**, 151-160 (2020). <https://doi.org/10.1016/j.neuroscience.2020.07.054>
- 662 67 Hatsopoulos, N. G., Xu, Q. & Amit, Y. Encoding of movement fragments in the motor cortex. *J*  
663 *Neurosci* **27**, 5105-5114 (2007). <https://doi.org/10.1523/JNEUROSCI.3570-06.2007>
- 664 68 Shenoy, K. V., Sahani, M. & Churchland, M. M. Cortical control of arm movements: a dynamical  
665 systems perspective. *Annu Rev Neurosci* **36**, 337-359 (2013). <https://doi.org/10.1146/annurev-neuro-062111-150509>
- 666 69 Li, N., Daie, K., Svoboda, K. & Druckmann, S. Robust neuronal dynamics in premotor cortex during  
667 motor planning. *Nature* **532**, 459-464 (2016). <https://doi.org/10.1038/nature17643>
- 668 70 Bollu, T. *et al.* Cortex-dependent corrections as the tongue reaches for and misses targets. *Nature*  
669 **594**, 82-87 (2021). <https://doi.org/10.1038/s41586-021-03561-9>
- 670 71 Guo, J. Z. *et al.* Cortex commands the performance of skilled movement. *Elife* **4**, e10774 (2015).  
671 <https://doi.org/10.7554/eLife.10774>
- 672 72 Desmurget, M. *et al.* Neural representations of ethologically relevant hand/mouth synergies in the  
673 human precentral gyrus. *Proc Natl Acad Sci U S A* **111**, 5718-5722 (2014).  
674 <https://doi.org/10.1073/pnas.1321909111>
- 675 73 Harris, K. D. & Shepherd, G. M. The neocortical circuit: themes and variations. *Nat Neurosci* **18**,  
676 170-181 (2015). <https://doi.org/10.1038/nn.3917>
- 677 74 Kiritani, T., Wickersham, I. R., Seung, H. S. & Shepherd, G. M. Hierarchical connectivity and  
678 connection-specific dynamics in the corticospinal-corticostriatal microcircuit in mouse motor cortex.  
679 *J Neurosci* **32**, 4992-5001 (2012). <https://doi.org/10.1523/JNEUROSCI.4759-11.2012>
- 680 75 Morandell, K. & Huber, D. The role of forelimb motor cortex areas in goal directed action in mice.  
681 *Sci Rep* **7**, 15759 (2017). <https://doi.org/10.1038/s41598-017-15835-2>
- 682 76 Sobinov, A. R. & Bensmaia, S. J. The neural mechanisms of manual dexterity. *Nat Rev Neurosci* **22**,  
683 741-757 (2021). <https://doi.org/10.1038/s41583-021-00528-7>
- 684 77 Billard, A. & Kragic, D. Trends and challenges in robot manipulation. *Science* **364** (2019).  
685 <https://doi.org/10.1126/science.aat8414>
- 686

- 687 78 Chen, S. *et al.* High-Throughput Strategy for Profiling Sequential Section With Multiplex Staining  
688 of Mouse Brain. *Frontiers in Neuroanatomy* **15** (2021). <https://doi.org/10.3389/fnana.2021.771229>
- 689 79 Tyson, A. L. *et al.* Accurate determination of marker location within whole-brain microscopy  
690 images. *Scientific Reports* **12**, 867 (2022). <https://doi.org/10.1038/s41598-021-04676-9>
- 691 80 Niedworok, C. J. *et al.* aMAP is a validated pipeline for registration and segmentation of high-  
692 resolution mouse brain data. *Nature Communications* **7**, 11879 (2016).  
693 <https://doi.org/10.1038/ncomms11879>
- 694 81 Ayling, O. G. S., Harrison, T. C., Boyd, J. D., Goroshkov, A. & Murphy, T. H. Automated light-  
695 based mapping of motor cortex by photoactivation of channelrhodopsin-2 transgenic mice. *Nature*  
696 *Methods* **6**, 219-224 (2009). <https://doi.org/10.1038/nmeth.1303>
- 697 82 Sun, Z. *et al.* Sox2 and Lef-1 interact with Pitx2 to regulate incisor development and stem cell  
698 renewal. *Development* **143**, 4115-4126 (2016). <https://doi.org/10.1242/dev.138883>
- 699 83 Qian, Y. *et al.* Programmable RNA sensing for cell monitoring and manipulation. *Nature* **610**, 713-  
700 721 (2022). <https://doi.org/10.1038/s41586-022-05280-1>
- 701 84 Martianova, E., Aronson, S. & Proulx, C. D. Multi-Fiber Photometry to Record Neural Activity in  
702 Freely-Moving Animals. *J Vis Exp* (2019). <https://doi.org/10.3791/60278>
- 703 85 Han, W. *et al.* Integrated Control of Predatory Hunting by the Central Nucleus of the Amygdala.  
704 *Cell* **168**, 311-324.e318 (2017). <https://doi.org/10.1016/j.cell.2016.12.027>
- 705 86 Takeshita, H. *et al.* Modified forelimb grip strength test detects aging-associated physiological  
706 decline in skeletal muscle function in male mice. *Scientific Reports* **7**, 42323 (2017).  
707 <https://doi.org/10.1038/srep42323>
- 708 87 Zhang, X. *et al.* Genetically identified amygdala–striatal circuits for valence-specific behaviors. *Nat*  
709 *Neurosci* **24**, 1586-1600 (2021). <https://doi.org/10.1038/s41593-021-00927-0>
- 710 88 Wang, B.-S. *et al.* Retinal and Callosal Activity-Dependent Chandelier Cell Elimination Shapes  
711 Binocularity in Primary Visual Cortex. *Neuron* **109**, 502-515.e507 (2021).  
712 [https://doi.org:https://doi.org/10.1016/j.neuron.2020.11.004](https://doi.org/https://doi.org/10.1016/j.neuron.2020.11.004)

## FIGURE LEGENDS

### Figure 1. Cell-type optogenetic activation screen identifies a rostral forelimb orofacial area.

- a.** PNs comprise hierarchically organized classes, each comprising multiple subpopulations defined by marker gene expression. See **Extended Data Fig. 1** for description of all subpopulations. IT, intratelencephalic; ET, extratelencephalic; PT, pyramidal tract; CT, corticothalamic.
- b.** Schematic of optogenetic motor mapping in head-fixed mice (see Methods). Nose tip is the coordinate origin.
- c.** Schematic of the 3mm x 6mm area mapped by optogenetic activation. See appendix for abbreviations.
- d.** Vector maps of hand (blue) and jaw (red) movement direction (arrow) and distance (arrow length) following activation of PTs<sup>Fezf2</sup> and ITs<sup>PlxnD1</sup> across different locations in the boxed area in **c**. Distance was averaged across mice and normalized (hand: 13 *Fezf2* and 7 *PlxnD1* mice; jaw: 11 *Fezf2* and 7 *PlxnD1* mice).
- e.** Representation of forelimb and mouth movements following RFO PT<sup>Fezf2</sup> and IT<sup>PlxnD1</sup> stimulation. Arrows indicate movements. See **Supplementary Videos 4, 5**.
- f.** Hand and jaw movement trajectories following RFO PT<sup>Fezf2</sup> and IT<sup>PlxnD1</sup> activation (circle in **d**). Black trajectory represents average. Purple triangle in the left panels denotes jaw position at stimulation onset. Circle and square indicate start and end positions, respectively. Colors in trajectories indicate time. Jaw trajectories were normalized relative to the start position (16 and 18 trials for hand and jaw trajectories for PTs<sup>Fezf2</sup> and 15 trials for ITs<sup>PlxnD1</sup>).
- g.** Changes in hand-to-nose and hand-to-hand distances upon RFO PT<sup>Fezf2</sup> and IT<sup>PlxnD1</sup> stimulation (gray shading). Bilateral and contralateral hand-to-mouth movements were induced with IT<sup>PlxnD1</sup> and PT<sup>Fezf2</sup> activation, respectively. Darker trajectories depict averages (18 trials for PTs<sup>Fezf2</sup> and 17 trials for ITs<sup>PlxnD1</sup>).
- h.** Maps of spatial dispersion of hand positions at the end of activation (averaged across 13 *Fezf2* and 7 *PlxnD1* mice).
- i.** Maps of hand-to-nose distance after activation (averaged across 13 *Fezf2* and 7 *PlxnD1* mice).
- j.** Probability of observing contralateral and/or bilateral hand-to-mouth eating-like movement in a 1-s window immediate before (pre) and during RFO stimulation (13 *Fezf2* and 13 *PlxnD1* mice).
- k.** Schematic of RFO location in relation to other motor areas. ALM, anterolateral motor cortex; RFA, rostral forelimb area; CFA, caudal forelimb area.
- l.** Schematic of body movements induced by RFO PT<sup>Fezf2</sup> and IT<sup>PlxnD1</sup> activation (blue bars) in freely-moving mice. Red, blue, and green arrow points to the jaw, contralateral and ipsilateral hand respectively. See **Supplementary Videos 6, 7**.
- m.** Single-trial movement trajectories of different body parts induced by PT<sup>Fezf2</sup> and IT<sup>PlxnD1</sup> activation in freely-moving mice (circle and square indicate start and end positions and color saturation indicates time).
- n.** Changes in hand-to-nose and hand-to-hand distances following RFO PT<sup>Fezf2</sup> and IT<sup>PlxnD1</sup> stimulation (gray shade) in free-moving mice. Bilateral and contralateral hand-to-mouth movements were induced with IT<sup>PlxnD1</sup> and PT<sup>Fezf2</sup> activation, respectively. Darker trajectories depict averages (9 trials for PTs<sup>Fezf2</sup> and 9 trials for ITs<sup>PlxnD1</sup>).
- o.** Distance of contralateral hand to nose following activation in *Fezf2* (n = 3) and *PlxnD1* (n = 5) mice (\*p < 0.05, two-sided paired t-test).
- p.** Probability of observing contralateral and/or bilateral hand-to-mouth eating-like movement in a 1-s window immediate before (pre) and during RFO stimulation in free-moving mice (3 *Fezf2* and 5 *PlxnD1* mice).
- q.** Probability of observing head-to-hand movement in a 1-s window immediate before (pre) and during RFO stimulation (3 *Fezf2* and 5 *PlxnD1* mice).

Stars indicate Bregma in **c, d, h, i, k**. Scale bars, 1 mm in **c, d, h, i, k**. Data are mean  $\pm$  s.e.m in **j, p**, and **q**. Shades around mean denote  $\pm$  s.e.m in **g, n**. A, anterior; P, posterior; D, dorsal; V, ventral; M, medial; L, lateral. The mouse drawing in **b** was adapted from scidraw.io (<https://scidraw.io/drawing/44>).

**Extended Data Fig. 1 | Different PN types exhibit distinct motor maps.** Related to Fig. 1

**a-d.** Vector maps of hand (blue) and jaw (red) movement direction and distance following optogenetic activation of PNs<sup>Emx1</sup> (**a**), PNs<sup>Thy1-Tg18</sup> (**b**), ITs<sup>Tbr2-E17</sup> (**c**), and CTs<sup>Tle4</sup> (**d**) in different locations of the dorsal cortex. Movement direction and distance along each axis is represented by arrow direction and length (distance averaged and normalized in 2 *Emx1*, 2 *Thy1-Tg18*, 4 *Tbr2-E17*, and 5 *Tle4* mice).

**e.** Maps of hand movement distance (linear travel distance, measured from start to end). No clear hand movement was induced from *Tcerg11* and *Sema3E* mice (Maps averaged from 2 *Emx1*, 2 *Thy1-Tg18*, 13 *Fezf2*, 5 *Tcerg11*, 5 *Sema3E*, 7 *PlxnD1*, 4 *Tbr2-E17*, and 5 *Tle4* mice).

**f.** Maps of total jaw movement distance. No clear jaw movement was induced from *Tcerg11* and *Sema3E* mice (Maps averaged from 2 *Emx1*, 2 *Thy1-Tg18*, 11 *Fezf2*, 5 *Tcerg11*, 5 *Sema3E*, 7 *PlxnD1*, 4 *Tbr2-E17*, and 5 *Tle4* mice).

**g.** Schematic of in vivo electrophysiological recording with optical tagging.

**h, i.** Light-evoked spikes from electrophysiological recordings in the secondary motor cortex (MOs) in a *Fezf2*- (**h**) or *PlxnD1-CreER;Ai32* (**i**) mouse (5 light pulses were delivered at 10 Hz for 0.5 s).

**j, k.** Vector maps of hand (blue) and jaw (red) movement direction and distance with optogenetic activation of PTs<sup>Fezf2</sup> (**j**) and ITs<sup>PlxnD1</sup> (**k**) using different stimulation parameters (compare with maps of 50 Hz, 0.5 s stimulation in **Fig. 1d**). Movement direction and distance along each axis are represented by arrow direction and length, respectively. Distance was averaged across mice and normalized to that from 10 Hz, 0.5 s stimulation (10 Hz, 0.5 s: n = 5 mice for PTs<sup>Fezf2</sup> or ITs<sup>PlxnD1</sup>; 50 Hz, 0.1 s: n = 4 mice for PTs<sup>Fezf2</sup> or ITs<sup>PlxnD1</sup>).

A, anterior; P, posterior; D, dorsal; V, ventral; M, medial; L, lateral. Stars indicate Bregma. Scale bars, 1 mm. The mouse drawing in **g** was adapted from scidraw.io (<https://scidraw.io/drawing/44>).

**Extended Data Fig. 2 | Characterization of forelimb and jaw movements induced by optogenetic activation of PTs<sup>Fezf2</sup> and ITs<sup>PlxnD1</sup>.** Related to Fig. 1

**a-c.** Maps of hand linear travel distance measured from start to end (**a**), total travel distance (**b**), and straightness index (**c**) (straightness index = linear travel distance/total travel distance, with smaller index = more rhythmic movement).

**d-f.** Hand trajectories following PT<sup>Fezf2</sup> activation at three sites as indicated by the three circles in **c**. Red circle at pCFA from 15 trials (**d**); yellow circle at mCFA from 19 trials and trajectory graphs of repetitive movements (**e**); green circle at aCFA from 17 trials (**f**). Lighter trajectories represent averages in **d, f**. Black trajectories in **e** indicate averages. Circle and square indicate start and end positions respectively in **d, f**. Note: the left hand is lifted and open after stimulation (white arrow in **f**).

**g, h.** 2D projections of hand trajectories from optogenetic activation of PTs<sup>Fezf2</sup> (**g**) and ITs<sup>PlxnD1</sup> (**h**). Projected trajectories were color coded based on stimulation location (top right panel in **g**), normalized to the start position (top left panel in **g**), and averaged across 13 *Fezf2* and 7 *PlxnD1* mice. Square indicates end position.

**i-k.** Maps of jaw linear travel distance measured from start to end (**i**), total travel distance (**j**), and straightness index (**k**) (Straightness index = linear travel distance/total travel distance, with smaller index = more rhythmic movement).

**l.** Example jaw trajectories following PT<sup>Fezf2</sup> or IT<sup>PlxnD1</sup> activation at two sites as indicated by the two circles in **k** (green circle for 20 PT<sup>Fezf2</sup> trials; orange circle for 16 IT<sup>PlxnD1</sup> trials). Black trajectories indicate averages.

Maps were averaged for 13 *Fezf2* and 7 *PlxnD1* mice in **a-c**. Maps were averaged for 11 *Fezf2* and 7 *PlxnD1* mice in **i-k**. Blue bar in **e, l** represents stimulation window. Stars indicate Bregma. Scale bars, 1

mm in **a-c, g, i-k**; 5 mm in **d, f**. A, anterior; P, posterior; D, dorsal; V, ventral; M, medial; L, lateral. The mouse drawing in **g** was adapted from scidraw.io (<https://scidraw.io/drawing/44>).

**Extended Data Fig. 3 | Activating AAV-targeted PTs<sup>Fezf2</sup> or ITs<sup>PlxnD1</sup> in RFO induces hand-to-mouth and mouth movements.** Related to Fig. 1

**a.** Schematic of the approach (left panel) and images of coronal sections showing PTs<sup>Fezf2</sup> and ITs<sup>PlxnD1</sup> infected by AAV-DIO-ChR2-eYFP injected into the right RFO (right panels). Scale bar, 1 mm.  
**b, c.** Example movement trajectories for the left hand or both hands for 20 PT<sup>Fezf2</sup> trials (**b**) and 19 IT<sup>PlxnD1</sup> trials (**c**). Lighter trajectories represent averages. Circle and square indicate start and end positions respectively. Note: **b** (yellow arrow) left hand is closed and **b** (white arrows) jaw opens to the contralateral side after stimulation. Scale bar, 5 mm.  
**d, e.** Movement trajectories of the jaw from 16 PT<sup>Fezf2</sup> trials (**d**) and 8 IT<sup>PlxnD1</sup> trials (**e**).  
**f, g.** 2D projections of left-hand trajectories after stimulation of 5 *Fezf2* mice (**f**) and 6 *PlxnD1* mice (**g**). Square indicates end position. A, anterior; P, posterior; D, dorsal; V, ventral; M, medial; L, lateral.  
**h, i.** Movement trajectories of the jaw following stimulation of 5 *Fezf2* mice (**h**) and 6 *PlxnD1* mice (**i**). Movement trajectories were normalized to the start position in **d-i**. Darker trajectories represent averages in **d-i**. Blue bar in **d, e, h, i** represents stimulation window.

**Figure 2. RFO is necessary for hand recruitment and oromanual coordination in pasta eating.**

**a.** Schematic of the Mouse Restaurant. A table mounted on an XZ stage brings food to the dining area. Three cameras record movement and a microphone records bite sound. Note: mouse crosses a small elevated step to enter the dining area. See **Extended Data Fig. 4a-c** and Methods for details.  
**b.** Pasta-eating schematic showing tracking of different body parts and the pasta (colored dots). Z axis is the dorsal-ventral axis. Mice handle the pasta with a support grasp (purple arrow) and a guide grasp (red arrow).  
**c.** Actogram of a mouse retrieving and eating a 15-mm angel-hair pasta piece. Key sensorimotor events (colored and annotated at the bottom) are superimposed upon Z-axis trajectories of nose (gray) and right (dark gray) and left (black) hands throughout the trial.  
**d.** Ethogram of pasta eating, which proceeds in a sequence of stages, each consisting of multiple action motifs (top); mice consume pasta in repeated handle-eat bouts. Bottom schematic depicts a typical sequence of four major coordinated hand (blue ring) and oral (red ring) actions in a handle-eat bout. Red arrow in sketches indicates direction of hand movement. Legends for labels in the upper left corner of each drawing are the same as those in **c**.  
**e.** Probability distribution of the time of the first hand-adjustment and the first bite in each handle-eat bout (n = 7 mice). Time 0 is the onset of hand withdraw, which marks the start of each bout.  
**f.** Nearly all hand adjustments (97.0 ± 0.8 %; n = 9 mice) were made with pasta clenched in the mouth, thus involving oromanual coordination.  
**g.** Average hand-to-nose distance begins to increase (red arrow) before bite onset (time 0, n = 9 mice).  
**h.** Schematic of hand movements immediately before and during pasta bite/snap (arrow indicates movement direction along Z axis; arrow length indicates speed).  
**i.** The relationship between up-down hand movements and bite, shown as the Z-axis left-hand trajectory overlaid with bite events. Left ankle was used as the reference to compute the trajectory, which was then band-pass filtered (0.4 - 10 Hz, lower panel) to compute the hand movement phase.  
**j.** Probability distribution for the phases of left-hand movement at the time of bites from an example trial in **i**.  
**k, l.** Average hand movement phase at the time of bite (**k**) and selectivity index of the phases (**l**). The narrower the probability distribution of phases the larger the selectivity index (n = 9 mice).  
**m.** Bilateral RFO muscimol infusion resulted in increased pasta drops in each trial (upper; n = 7 mice; \*\*\*p < 0.005, two-sided paired t-test) and feeding duration for each pasta piece (lower; n = 8 mice; \*p < 0.05, two-sided Wilcoxon signed-rank test).

860 **n, o.** Probability distribution and cumulative probability of Z-axis positions of the left hand (**n**) and nose  
861 (**o**) at the time of bites following saline and muscimol infusion ( $n = 5$  mice; \*\*\*\* $p < 0.001$ ,  
862 Kolmogorov-Smirnov test). Data from left ankle after saline infusion is shown as reference.  
863 Shades around mean denote  $\pm$  s.e.m in **e, g, n, o**. Data are mean  $\pm$  s.e.m in **f, k-m**. Mouse drawings in **a**  
864 were adapted from scidraw.io (<https://scidraw.io/drawing/122> and <https://scidraw.io/drawing/96>).  
865

866 **Extended Data Fig. 4 | Design of the Mouse Restaurant for studying feeding behavior.** Related to  
867 Fig. 2

868 **a, b.** Schematic of the Mouse Restaurant. A table mounted on an XZ stage (**b**) brings food to the dining  
869 area. The food dispenser has two stacked plates, each with a capacity for 24 food items (**b**). A water port  
870 in the waiting area allows mice to drink and thus consume more food. Two pairs of infrared (IR) break-  
871 beam sensors detect a mouse moving from the waiting to dining area. A door is used to block access to  
872 the dining area during food delivery. Three cameras record mouse behavior and a microphone records  
873 bite sounds.

874 **c.** Events and behavioral sequence in Mouse Restaurant and signals used for task control. Behaviors in  
875 red were recorded in the dining area.

876 **d.** Configurations of 15-mm angel-hair pasta when delivered to the dining area. 3D-printed holders were  
877 used to load the pasta into the food dispenser in **b**. For configuration 3, mice occasionally retrieved the  
878 pasta with the hands instead of the mouth. Trials with hand retrieval were not included in the analysis  
879 due to low occurrence.

880 **e.** Processing of the audio signal for bite detection. Audio signal was band-pass filtered (800-8,000 Hz),  
881 rectified, smoothed (5-ms Gaussian window), and thresholded ( $4 \times$  s.d. above mean) to detect bite  
882 events (purple circles). Red rectangle indicates the time window enlarged on the right. Mouse drawings  
883 in **a** were adapted from scidraw.io (<https://scidraw.io/drawing/122> and <https://scidraw.io/drawing/96>).  
884

885 **Extended Data Fig. 5 | Action motifs and sensorimotor events in pasta eating.** Related to Fig. 2

886 **a-d.** Image sequences showing manually labeled action motifs observed in angel-hair pasta eating.  
887 Images in each panel represent the start (left), middle, and end (right) of each action. Red arrows in **a**  
888 point to the jaw as it opens to retrieve the pasta. A food-in-mouth event is labeled when the pasta is  
889 clearly lifted from the floor (blue arrow in **a**). Arrows in **b** point to the tongue as it brings the pasta into  
890 the mouth. Arrows in **c** indicate the upward body movement leading to the sitting posture. After mouth  
891 retrieval, mice make reaching movements to grasp pasta with the hands (arrows in **d**).

892 **e.** Image of a hand-withdraw event, in which mice raise their hands toward mouth (arrow) to start a  
893 handle-eat bout after the previous chewing phase. Right panel shows Z-axis trajectory of the right hand  
894 before and after a hand-withdraw event, with the cyan line indicating the time of withdraw shown in the  
895 left image.

896 **f, g.** Image sequences showing unimanual (**f**) and bimanual (**g**) adjustments through release and re-grasp  
897 movements to reposition the hands on the pasta. Arrows in **f, g** point to release (middle) and re-grasp  
898 (right) hand movements.  
899

900 **Extended Data Fig. 6 | Hand adjustment and pasta bite both involve oromanual coordination.**

901 Related to Fig. 2

902 **a.** Probability distribution of time from hand adjustments to the first bite in each handle-eat bout. The  
903 proportion of hand adjustments made before the first bite for 7 mice is  $69.2 \pm 2.2$  %, indicating hand  
904 adjustments mainly occur before the first bite. Data are mean  $\pm$  s.e.m.

905 **b.** Action sequences for unimanual and bimanual adjustments.

906 **c, d.** Average Z-axis position (**c**) and speed (**d**) of nose and both hands aligned to bite onset (vertical  
907 dashed line) showing that pasta biting involves joint bimanual and jaw movement. Note that the  
908 downward hand movement starts before the bite (arrows in **c, d**). The two peaks in **d** is likely due to the  
909 breaking of pasta.

910 e. Average hand-nose orientation aligned to bite onset, showing a downward hand movement relative to  
911 the nose (mouth) before the bite. The schematic depicts the angle of hand-nose orientation (left panel).  
912 Shades around mean denote  $\pm$  s.e.m in **c-e** for 9 mice.

913  
914 **Extended Data Fig. 7 | Muscimol inhibition in RFO impairs hand recruitment in pasta eating but**  
915 **not bite and grip force.** Related to Fig. 2

916 **a.** Schematic of bilateral muscimol infusion into the RFO.

917 **b.** Representative diffusion pattern of BODIPY-tagged muscimol (red; 1  $\mu$ l) in the RFO of coronally  
918 sectioned (75  $\mu$ m) tissue stained with DAPI (blue). Scale bar, 500  $\mu$ m.

919 **c, d.** Actograms of exemplar trials of a mouse following bilateral saline (**c**) or muscimol (**d**) infusion. In  
920 muscimol trials, the mouse usually did not adopt a sitting posture, bit the pasta on the ground without  
921 recruiting hands, and often dropped the pasta (red arrows) during eating. In muscimol trials feeding time  
922 is prolonged, a mouse sometimes left the dining area without finishing the pasta, or pasta flew out of the  
923 dining area after a bite due to uncoordinated oromaneal movements. Three exemplar time windows of a  
924 muscimol trial are shown in **d1-d3**. Black arrow in **d2** indicates the bite corresponding to the posture  
925 image in the bottom right panel. Note the mouse's hunched posture; red arrow in the image points to the  
926 nose close to the floor. Also see **Supplementary Videos 12, 13**.

927 Muscimol inhibition did not impair pasta detection (**e**,  $n = 8$  mice), increased mouth retrieval attempts (**f**,  
928  $n = 7$  mice;  $*p < 0.05$ , two-sided paired t-test), increased number of trials in which mice consumed the  
929 pasta without sitting on haunches (**g**;  $n = 8$  mice, with one mouse never adopting a sitting posture), and  
930 did not impair grip force or bite force (**h**;  $n = 6$  mice). Data are mean  $\pm$  s.e.m. NS, not significant, two-  
931 sided paired t-test.

932  
933 **Figure 3. PT<sup>Fezf2</sup> and IT<sup>PlxnD1</sup> activity in RFO correlate with pasta manipulation and eating.**

934 **a.** Schematic depicting fiber photometry from the right RFO and left aCFA. Star indicates Bregma.  
935 Scale bar, 1 mm.

936 **b.** Coronal sections showing PTs<sup>Fezf2</sup> and ITs<sup>PlxnD1</sup> in the RFO and aCFA expressing GCaMP7f from  
937 AAV infection. Scale bar, 500  $\mu$ m.

938 **c, d.** Single-trial calcium activity traces of PTs<sup>Fezf2</sup> (**c**) and ITs<sup>PlxnD1</sup> (**d**) in the RFO (black) and aCFA  
939 (gray) of mice eating 15-mm angel-hair pasta. Actograms were overlaid on activity traces. Example time  
940 windows are expanded in **c1-c3** and **d1-d3**. Time 0 is the entry of the dining area. The rise of aCFA  
941 activity at time 0 (dashed line) correlates with crossing the step for entering the dining area (**Fig. 2a**).

942 **e, h.** Heat maps of RFO PT<sup>Fezf2</sup> (**e**) and IT<sup>PlxnD1</sup> (**h**) population activity aligned to retrieval start (left),  
943 hand withdraw (middle), and bite (right). Activity traces were sorted by the earliest hand withdraw (left),  
944 chew (middle), and hand adjustment (right) events, respectively.

945 **f, g, i, j.** Averaged PT<sup>Fezf2</sup> (**f, g**) and IT<sup>PlxnD1</sup> (**i, j**) population activity in the RFO and aCFA aligned to  
946 retrieval start (**f, i**; left panels) and hand withdraw, hand adjustment, bite, and chew (**g, j**; left panels).

947 Vertical dashed lines indicate average time to the first hand withdraw in **f, i**. Changes in population  
948 activity are shown in the right panels. RFO PT<sup>Fezf2</sup> and IT<sup>PlxnD1</sup> activity rise after the onset of hand  
949 withdraw with a lag (red arrow in the expanded window of **g, j**).  $n = 6$  mice for PTs<sup>Fezf2</sup> and 6 mice for  
950 ITs<sup>PlxnD1</sup>;  $*p < 0.05$ ,  $***p < 0.005$ , two-sided paired t-test.

951 **k.** Time from the onset of hand withdraw to the rise of population activity ( $n = 6$  mice for PTs<sup>Fezf2</sup> and 6  
952 mice for ITs<sup>PlxnD1</sup>;  $*p < 0.05$ , two-sided Wilcoxon rank-sum test).

953 **l.** Correlation between RFO IT<sup>PlxnD1</sup> population activity and hand-to-nose distance. Boxed time window  
954 is expanded on the right. Green arrows indicate the onset of signal rise.

955 **m.** Averaged correlation coefficient of RFO population activity with hand-to-nose distance shifted in  
956 time from a *PlxnD1* mouse. Peak correlation coefficient is shown in the right panel ( $n = 6$  mice for  
957 PTs<sup>Fezf2</sup> and 6 mice for ITs<sup>PlxnD1</sup>;  $*p < 0.05$ , two-sided Wilcoxon rank-sum test).

958 **n, o, q, r.** Single-trial calcium activity in the RFO and aCFA as *Fezf2* (**n**) and *PlxnD1* (**q**) mice  
959 consumed 1-mm angel-hair pasta without sitting up or hand recruitment. Key sensorimotor events

(colored annotations) were overlaid on the activity traces. Time 0 is the entry to the dining area.

Corresponding heat maps (**o**, **r**) were aligned to retrieval start for 1-mm pasta.

**p**, **s**. Averaged RFO  $PT^{Fezf2}$  (**p**) and  $IT^{PlxnD1}$  (**s**) population activity aligned to retrieval start for 15-mm and 1-mm angel-hair pasta ( $n = 7$  mice for  $PTs^{Fezf2}$  and 3 mice for  $ITs^{PlxnD1}$ ). Vertical dashed lines indicate the average time to establish the sitting posture when eating 15-mm pasta. Activity levels remained high when mice handled and ate 15-mm pasta but declined when eating 1-mm pasta. Shading around mean denotes  $\pm$  s.e.m in **f**, **g**, **i**, **j**, **m**, **p**, **s**. Data are mean  $\pm$  s.e.m in **f**, **g**, **i-k**.

**Extended Data Fig. 8 |  $PT^{Fezf2}$  and  $IT^{PlxnD1}$  activity in aCFA correlate with skilled stepping.** Related to Fig. 3

**a**, **d**. Single-trial calcium activity of  $PTs^{Fezf2}$  (**a**) and  $ITs^{PlxnD1}$  (**d**) in the RFO and aCFA during dining area entry and pasta retrieval. Actograms were overlaid on the activity traces.

**b**, **e**. Heat maps of  $PT^{Fezf2}$  (**b**) and  $IT^{PlxnD1}$  (**e**) population activity in the RFO and aCFA aligned to crossing the entry step (see **Extended Data Fig. 4a**) and sorted by pasta retrieval start.

**c**, **f**. Averaged population activity of  $PTs^{Fezf2}$  (**c**) and  $ITs^{PlxnD1}$  (**f**) in the RFO and aCFA aligned to crossing the step to the dining area ( $n = 6$  mice for  $PTs^{Fezf2}$  and 6 mice for  $ITs^{PlxnD1}$ ). Vertical dashed lines indicate average time to the retrieval start. Shading around mean denotes  $\pm$  s.e.m.

**Extended Data Fig. 9 | Automated identification of handle-bite and chew periods in each handle-eat bout.** Related to Fig. 3

**a**. Hand-to-nose distances plotted in a pasta-eating trial superimposed with alternating handle-bite (green) and chew (red) periods. A two-state hidden Markov model (HMM) was used to identify the handle-bite and chew periods. Vertical dashed lines indicate manually labeled hand-withdraw events. An example time window is enlarged in **a'**.

**b**. Probability distribution of errors between hand-withdraw timestamps labeled manually and computed from HMM. The proportion of  $|\text{error}| < 0.1$  s is  $84.13 \pm 1.96$  % (6 sessions from 5 mice).

**c**. Hit rate. Hit rate is the proportion of hand-withdraw events labeled both manually and by HMM over all hand-withdraw events labeled manually (6 sessions from 5 mice). Data are mean  $\pm$  s.e.m.

**Figure 4. RFO  $PTs^{Fezf2}$  and  $ITs^{PlxnD1}$  contribute to distinct components of oromaneal manipulation.**

**a**. Schematic for optogenetic inhibition of PN types. AAV-DIO-GtACR1-eYFP were injected bilaterally into the RFO. Two inhibition schemes were directed to the retrieval and handle-eat stages, respectively. Green bar indicates 4s inhibition. Time 0 denotes entry into the dining area.

**b**. Actograms (legend shown in **f**) of a mouse in control (upper) and  $PN^{Emx1}$  inhibition (lower; green bar) trials. Z-axis trajectories of nose (light gray), right (dark gray) and left (black) hands are shown.

**c**, **d**.  $PN^{Emx1}$  and  $PT^{Fezf2}$  inhibition interfered with pasta retrieval, measured as lengthened time from entry to retrieval (**c**) and increased number of retrieval attempts (i.e., retrieval jaw movements) (**d**).

**e**.  $PN^{Emx1}$  and  $IT^{PlxnD1}$  inhibition delayed the first bite after adoption of a sitting posture.

**f**. Actograms of a mouse at handle-eat stage in control (top) and  $PN^{Emx1}$  inhibition (bottom) trials. Z-axis trajectories of nose and two hands are shown.  $PN^{Emx1}$  inhibition led to substantially increased hand adjustments but no biting.

**g**.  $PN^{Emx1}$ ,  $PT^{Fezf2}$ , and  $IT^{PlxnD1}$  inhibition resulted in decreased number (left) and increased delay (right) of bites. Purple ticks in top schematic indicate bite events.

**h**. Differences in total hand adjustments (left) and bimanual adjustments (right) made for each bite with PN inhibition compared to control. Note the Y-axis for  $PNs^{Emx1}$  is different from that for  $PTs^{Fezf2}$  and  $ITs^{PlxnD1}$ .

**i**. Probability distribution of pasta orientation during handle-eat stage in control and PN inhibition trials; gray trace denotes probability distribution at the time of bite in control trials. Schematic shows exemplar pasta orientation for different conditions. XY plane is the ground plane. Orientation was normalized for

010 each mouse based on the average bite orientation of control trials and then pooled together across mice  
011 (\*\*\*\* $p < 0.001$ , Control vs Inhibition, Kolmogorov-Smirnov test).  
012 **j.** Probability distribution of pasta orientations in control trials was more similar to that of bite  
013 orientations in control trials compared with that of pasta orientations in inhibition trials, quantified as  
014 difference in Hellinger distance. The smaller the Hellinger distance, the more similar the two probability  
015 distributions.  
016 **k.** Schematic of the coordinate system used for analyzing bite posture (left) and average positions of  
017 nose, eyes, hands, and pasta at the time of bite from an exemplar mouse (right). Cross indicates inferred  
018 bite location inside the mouth. Right eye is the coordinate origin. Transformed X'Y' plane denotes nose  
019 and two eyes. X' axis crosses the two eyes plane pointing toward the left eye. Y' axis points to the  
020 direction opposite to the nose. Z' axis points outward the mouse's body. Blue and black colors indicate  
021 positions with and without inhibition, respectively.  
022 **l.** Average Y'-axis position of support and guide hands at the time of the bite, showing increased hand-  
023 to-mouth distance.  
024 **m.**  $PT^{Fezf2}$  and  $IT^{PlxnD1}$  inhibition led to a vertical shift of bite orientations in the X'Y' plane.  
025 **n.** Probability distributions of the phases of support-hand movement at the time of bites in control and  
026  $PT^{Fezf2}$  or  $IT^{PlxnD1}$  inhibition trials. Schematic in the left panel depicts the coordination of hand movement  
027 with pasta bite/snap.  
028 **o, p.** Average hand movement phase at the time of the bite (**o**) and selectivity index of the bite phase (**p**).  
029 The narrower the probability distribution of phase the higher the selectivity index. Results from support  
030 and guide hands were similar and thus were pooled.  
031 Analyses in **g-p** were carried out for the same 4-s window in **a** for control and inhibition trials. Data are  
032 mean  $\pm$  s.e.m in **k-m, o, p**.  $n = 6$  mice for  $PNs^{Emx1}$ , 8 mice for  $PTs^{Fezf2}$ , and 9 mice for  $ITs^{PlxnD1}$ , for the  
033 analyses in **c-e, g-j, l, m, o, p**. \* $p < 0.05$ , \*\* $p < 0.01$ , \*\*\* $p < 0.005$ , \*\*\*\* $p < 0.001$ , two-sided paired t-  
034 test and two-sided Wilcoxon signed-rank test for **c-e, g, h, j, l, m, o, p**.

### 035 **Extended Data Fig. 10 | $PTs^{Fezf2}$ and $ITs^{PlxnD1}$ in RFO contribute to oromaneal manipulation.**

036 Related to Fig. 4

037 **a.** Coronal sections showing  $PNs^{Emx1}$ ,  $PTs^{Fezf2}$ , and  $ITs^{PlxnD1}$  in the RFO that were infected by Cre-  
038 dependent AAV-DIO-GtACR1-eYFP injection in the corresponding driver mouse. Scale bar, 1 mm.  
039 **b.** PN inhibition did not impact the time taken for pasta detection compared to control trials.  
040 **c.**  $PN^{Emx1}$  and  $IT^{PlxnD1}$  inhibition increased total hand adjustment preceding the first bite.  
041 **d.**  $IT^{PlxnD1}$  inhibition increased bimanual adjustment preceding the first bite.  
042 **e.**  $PN^{Emx1}$  and  $PT^{Fezf2}$  inhibition led to a significant increase in pasta-orientation change rate during the  
043 handle-eat stage. Left panel shows a schematic for quantifying pasta orientations. XY plane is the  
044 ground plane.  
045  $n = 6$  mice for  $PNs^{Emx1}$ , 8 mice for  $PTs^{Fezf2}$ , and 9 mice for  $ITs^{PlxnD1}$ . \* $p < 0.05$ , \*\* $p < 0.01$ , two-sided  
046 paired t-test and two-sided Wilcoxon signed-rank test.

### 047 **Extended Data Fig. 11 | Inhibiting $PTs^{Fezf2}$ or $ITs^{PlxnD1}$ in RFO does not impair the bite.** Related to 048 Fig. 4

049 **a.** Schematic of pasta-bite apparatus. Angel-hair pasta is inserted into a metal tube and secured in place  
050 with a screw. A small segment (~ 3 mm) of the pasta projects from the tube allowing the mouse to bite  
051 off the pasta segment without hand use. Bottom panel shows inhibition scheme, which covers the whole  
052 trial period (green bar).  
053 **b.** Number of bites (left panel) and duration taken (right panel) to bite a pasta segment. Purple ticks in  
054 the schematic indicate bite events.  $n = 7$  mice for  $PTs^{Fezf2}$  and 3 mice for  $ITs^{PlxnD1}$ . The mouse drawing  
055 in **a** was adapted from scidraw.io (<https://scidraw.io/drawing/94>).  
056  
057  
058

059 **Extended Data Fig. 12 | Analyses of correlation between hand-mouth distance and pasta**  
060 **orientation.** Related to Fig. 4

061 **a.** Correlations between the Y'-axis positions of support or guide hands with pasta orientation in the  
062 X'Y' plane at the time of the bite in a *Fezf2* mouse. Black and blue lines are linear fittings and yellow  
063 line indicates pasta orientation. The support hand is more strongly correlated with the pasta orientation  
064 at the time of the bite than is the guide hand. Schematic on the right shows that the more the support  
065 hand deviates from the mouth along the Y' axis, the more vertical the X'Y' orientation of the pasta at  
066 the time of a bite.

067 **b.** Correlation coefficient between Y'-axis positions of support and guide hand with pasta orientation in  
068 the X'Y' plane at the time of the bite for control trials (3 *Fezf2* and 6 *PlxnD1* mice) and inhibition trials  
069 (2 *Fezf2* and 5 *PlxnD1* mice). The support hand is more strongly correlated to pasta orientation than the  
070 guide hand, irrespective of PN inhibition.

071  
072 **Extended Data Fig. 13 | Analyses of pasta bite location.** Related to Fig. 4

073 **a, b.** Pasta and hand-mouth relationship at the time of the bite in control trials of two exemplar mice.

074 Pasta was positioned to the mouth from right side by the mouse in **a** and from either side by the mouse  
075 in **b**. Spatial 3D coordinate system is as described in **Fig. 4k**.

076 **c.** Schematic showing that if a mouse repeatedly bites pasta at a same location inside its mouth, the new  
077 variables x and y, transformed based on the top and bottom coordinates of the pasta, should have a linear  
078 relationship (see Methods for details).

079 **d, e.** Mice bit the pasta at a same location in the mouth (i.e., with the incisors) irrespective of pasta  
080 orientation and positioning from the left or right side. Linear fittings for the new variables x and y,  
081 transformed from pasta locations presented in **a, b**, are shown. Even in cases when pasta was positioned  
082 from either side (**b**), the new variables x and y still have a strong linear relationship (**e**). Yellow lines in **e**  
083 indicate the sides of pasta positioning.

084 **f, g.** Bite location in the mouth in relation to average positions of nose, eyes, hands, and the pasta. Black  
085 cross indicates bite location computed from the linear fitting in **d, e**. The bite location corresponds to  
086 incisor tips.

087 **h.** Mice bit pasta with the incisors in control and PN inhibition trials.  $R^2$  values of linear fittings (e.g.,  
088 those in **d, e**) across mice are shown (see Methods for details).  $n = 8$  mice for  $PTs^{Fezf2}$  and 8 mice for  
089  $ITs^{PlxnD1}$ .

090  
091 **Figure 5. Input-output tracing of  $PTs^{Fezf2}$  and  $ITs^{PlxnD1}$  in RFO reveal the brain network for**  
092 **oromaneal coordination.**

093 **a.** Schematic for anterograde tracing of  $PTs^{Fezf2}$  and  $ITs^{PlxnD1}$  in the RFO.

094 **b.** Axon projection matrix from RFO to 315 ipsilateral and 315 contralateral targets (in rows), each  
095 grouped under 12 major categories (left column) for *Fezf2* and *PlxnD1* mice. Color shades in each  
096 column represent fraction of total axon signal averaged from 2 *Fezf2* and 2 *PlxnD1* mice.

097 **c.** Schematic for retrograde monosynaptic rabies tracing of  $PTs^{Fezf2}$  and  $ITs^{PlxnD1}$  in the RFO.

098 **d.** Monosynaptic input matrix to RFO from 315 ipsilateral and 315 contralateral targets (in rows), each  
099 grouped under 12 major categories (left column) for *Fezf2* and *PlxnD1* mice. Color shades in each  
100 column represent fraction of total input cells averaged from 4 *Fezf2* and 5 *PlxnD1* mice.

101 **e.** A summary wiring diagram of efferent from (solid line) and afferent to (dashed line)  $PTs^{Fezf2}$  and  
102  $ITs^{PlxnD1}$  in right RFO. Related results are shown in **Extended Data Figs. 14, 15**. See text for detailed  
103 description. AId, agranular insular area, dorsal part; APN, anterior pretectal nucleus; CB, cerebellum;  
104 CEAc, central amygdalar nucleus, capsular part; CL, central lateral nucleus of the thalamus; CP,  
105 caudoputamen; GPe, globus pallidus, external segment; GPi, globus pallidus, internal segment; GRN,  
106 gigantocellular reticular nucleus; HPF, hippocampal formation; HY, hypothalamus; IRN, intermediate  
107 reticular nucleus; MD, mediodorsal nucleus of the thalamus; MDRN, medullary reticular nucleus; MOp,  
108 primary motor area; MOs, secondary motor area; MRN, midbrain reticular nucleus; OLF, olfactory

109 areas; PAL, pallidum; PARN, parvicellular reticular nucleus; PCN, paracentral nucleus; PF,  
110 parafascicular nucleus; PG, pontine gray; PO, posterior complex of the thalamus; PPN,  
111 pedunculopontine nucleus; PSV, principal sensory nucleus of the trigeminal; SC, superior colliculus;  
112 SCm, superior colliculus, motor related; SMT, submedial nucleus of the thalamus; sp, cortical subplate;  
113 SPV, spinal nucleus of the trigeminal; SSp-m, primary somatosensory area, mouth; SSp-ul, primary  
114 somatosensory area, upper limb; SSs, secondary somatosensory area; STN, subthalamic nucleus; STR,  
115 striatum; VAL, ventral anterior-lateral complex of the thalamus; VISC, visceral area; VM, ventral  
116 medial nucleus of the thalamus; ZI, zona incerta.

117  
118 **Extended Data Fig. 14 | Brian-wide projection targets of PTs<sup>Fezf2</sup> and ITs<sup>PlxnD1</sup> in RFO.** Related to  
119 Fig. 5

120 **a.** Strategy and timeline for anterograde tracing of PTs<sup>Fezf2</sup> and ITs<sup>PlxnD1</sup> in the RFO. TM, tamoxifen.  
121 **b.** Images at the RFO injection site (first row) and selected projection targets: eGFP expression from  
122 Flp-activated viral vector (green) and background autofluorescence (red). PTs<sup>Fezf2</sup> show a weak  
123 projection to the cortex and striatum whereas ITs<sup>PlxnD1</sup> show a strong bilateral projection to the cortex  
124 and striatum.  
125 **c.** Images of selected subcortical projection targets of PTs<sup>Fezf2</sup>. Left panels show eGFP expression from  
126 Flp-activated viral vector (green) and background autofluorescence (red). Right panels show mCherry  
127 expression from Flp-activated viral vector (red) and Nissl staining (blue). PT<sup>Fezf2</sup> axons form the  
128 pyramidal decussation and enter the spinal cord (bottom right panel).  
129 **d.** Schematic depicting main RFO efferent targets for PTs<sup>Fezf2</sup> and ITs<sup>PlxnD1</sup>. ITs<sup>PlxnD1</sup> project bilaterally  
130 to multiple cortical areas, the ventrolateral striatum, and CEAc. PTs<sup>Fezf2</sup> project weakly within the  
131 cerebral cortex and striatum but project strongly to subcortical structures at all levels. Scale bar, 500  $\mu$ m.  
132 AId, agranular insular area, dorsal part; APN, anterior pretectal nucleus; CEAc, central amygdalar  
133 nucleus, capsular part; CL, central lateral nucleus of the thalamus; CP, caudoputamen; GPe, globus  
134 pallidus, external segment; GPi, globus pallidus, internal segment; GRN, gigantocellular reticular  
135 nucleus; IRN, intermediate reticular nucleus; MD, mediodorsal nucleus of the thalamus; MdD,  
136 medullary reticular nucleus, dorsal part; MDRN, medullary reticular nucleus; MdV, medullary reticular  
137 nucleus, ventral part; MOp, primary motor area; MOs, secondary motor area; MRN, midbrain reticular  
138 nucleus; PARN, parvicellular reticular nucleus; PCN, paracentral nucleus; PF, parafascicular nucleus;  
139 PG, pontine gray; PO, posterior complex of the thalamus; PPN, pedunculopontine nucleus; PSV,  
140 principal sensory nucleus of the trigeminal; pyx, pyramidal decussation; SC, superior colliculus; SMT,  
141 submedial nucleus of the thalamus; Spd, spinal cord; SPV, spinal nucleus of the trigeminal; SSp-m,  
142 primary somatosensory area, mouth; SSp-n, primary somatosensory area, nose; SSp-ul, primary  
143 somatosensory area, upper limb; SSs, secondary somatosensory area; STN, subthalamic nucleus; V,  
144 motor nucleus of trigeminal; VAL, ventral anterior-lateral complex of the thalamus; VII, facial motor  
145 nucleus; VISC, visceral area; VM, ventral medial nucleus of the thalamus; ZI, zona incerta.

146  
147 **Extended Data Fig. 15 | Brian-wide monosynaptic inputs to PTs<sup>Fezf2</sup> and ITs<sup>PlxnD1</sup> in RFO.** Related  
148 to Fig. 5

149 **a.** Strategy and timeline for retrograde monosynaptic rabies tracing of PTs<sup>Fezf2</sup> and ITs<sup>PlxnD1</sup> in the RFO.  
150 TM, tamoxifen.  
151 **b.** Images at RFO injection site (first row) and selected afferent sources: mCherry expression from  
152 rabies viral vector (red) and eGFP expression from Cre-activated starter virus (green). Both PTs<sup>Fezf2</sup> and  
153 ITs<sup>PlxnD1</sup> receive afferents from cortical areas and the thalamus.  
154 **c.** Images showing input cells in the GPe that monosynaptically connect to PTs<sup>Fezf2</sup> (left panel) and  
155 ITs<sup>PlxnD1</sup> (right panel) in the RFO.  
156 **d, e.** Proportion of input cells in cortical areas and thalamic nuclei (4 *Fezf2* and 5 *PlxnD1* mice). Data  
157 are mean  $\pm$  s.e.m.

158 **f.** Schematic depicting input sources to PTs<sup>Fezf2</sup> and ITs<sup>PlxnD1</sup> in the RFO from cortical areas, the  
159 thalamus, and basal ganglia. Size of the nodes reflect input cell number. Scale bar, 500  $\mu$ m. AId,  
160 agranular insular area, dorsal part; CL, central lateral nucleus of the thalamus; CM, central medial  
161 nucleus of the thalamus; CP, caudoputamen; FRP, frontal pole; GPe, globus pallidus, external  
162 segment; GU, gustatory areas; MD, mediodorsal nucleus of the thalamus; MOp, primary motor area;  
163 MOs, secondary motor area; ORBl, orbital area, lateral part; PCN, paracentral nucleus; PF,  
164 parafascicular nucleus; PO, posterior complex of the thalamus; SI, substantia innominata; SMT,  
165 submedial nucleus of the thalamus; SSp-bfd, primary somatosensory area, barrel field; SSp-m,  
166 primary somatosensory area, mouth; SSp-n, primary somatosensory area, nose; SSp-ul, primary  
167 somatosensory area, upper limb; SSp-un, primary somatosensory area, unassigned; SSs, secondary  
168 somatosensory area; VAL, ventral anterior-lateral complex of the thalamus; VISC, visceral area;  
169 VM, ventral medial nucleus of the thalamus; VPM, ventral posteromedial nucleus of the thalamus.

## 170 SUPPLEMENTARY VIDEOS

171  
172 **Supplementary Video 1. Optogenetic activation of PTs<sup>Fezf2</sup> in posterior Caudal Forelimb Area of head-**  
173 **fixed mouse.** Optogenetic activation (PTs<sup>Fezf2</sup> in pCFA: P 1.125, L 1.125; 0.5 s) in a head-fixed mouse induces  
174 a lateral abduction of the left forelimb, with digit opening and extension and elbow extension. Associated  
175 facial movements include vibrissae whisking and eyelid opening.

176 **Supplementary Video 2. Optogenetic activation of PTs<sup>Fezf2</sup> in medial Caudal Forelimb Area of head-**  
177 **fixed mouse.** Optogenetic activation (PTs<sup>Fezf2</sup> in mCFA: A 0, L 1.5; 0.5 s) in a head-fixed mouse induces  
178 treading (up/down) movements of the left forelimb. With stimulation onset the forelimb is raised by elbow  
179 flexion and then lowered by elbow extension (repeated a number of times). Digit flexion follows elbow flexion  
180 and digit extension leads elbow extension. Vibrissae whisk with a similar rhythm to the treading movement.  
181 The movement has features of a placing response in which a hand attempts to contact and obtain support from  
182 a surface.

183 **Supplementary Video 3. Optogenetic activation of PTs<sup>Fezf2</sup> in anterior Caudal Forelimb Area of head-**  
184 **fixed mouse.** Optogenetic activation (PTs<sup>Fezf2</sup> in aCFA: A 0.75, L 1.875; 0.5 s) in a head-fixed mouse induces  
185 a stepping or reaching-like forelimb movement. The upward movement involves sequentially, elbow, wrist,  
186 and digit flexion followed by extension. At the apex of the movement the limb is in a relaxed posture. Eyelid  
187 opening and whisking accompany the movement. The movement has features resembling reaching or stepping.

188 **Supplementary Video 4. Optogenetic activation of PTs<sup>Fezf2</sup> in Rostral Forelimb Orofacial area of head-**  
189 **fixed mouse.** Optogenetic activation (PTs<sup>Fezf2</sup> in RFO: A 1.5, L 2.25; 0.5 s) in a head-fixed mouse induces  
190 left hand adduction to the body midline with hand supination and digit flexing and closing. Associated facial  
191 movement includes two cycles of jaw opening and closing with lateral leftward tongue protrusion.

192 **Supplementary Video 5. Optogenetic activation of ITs<sup>PlxnD1</sup> in Rostral Forelimb Orofacial area of head-**  
193 **fixed mouse.** Optogenetic activation (ITs<sup>PlxnD1</sup> in RFO: A 1.5, L 2.25; 0.5 s) in a head-fixed mouse induces  
194 bilateral digit flexion and closing followed by elbow flexion and adduction of both hands toward the body  
195 midline. Adduction and flexion at the shoulders then raise both hands to the mouth. The movement has  
196 features of eating or grooming.

197 **Supplementary Video 6. Optogenetic activation of PTs<sup>Fezf2</sup> in Rostral Forelimb Orofacial area of free-**  
198 **moving mouse.** Optogenetic activation (PTs<sup>Fezf2</sup> in RFO: A 1.125, L 1.9; 0.5 s) in a free-moving mouse  
199 induces shoulder adduction that carries the left hand, with associated hand supination, toward the body midline.  
200 Ipsiversive head turning and lowering bring the snout to contact the radial surface of the hand. The right hand  
201 maintains body postural support.

202 **Supplementary Video 7. Optogenetic activation of ITs<sup>PlxnD1</sup> in Rostral Forelimb Orofacial area of free-**  
203 **moving mouse.** Optogenetic activation (ITs<sup>PlxnD1</sup> in RFO: A 2, L 2.625; 0.5 s) in a free-moving mouse  
204 interrupts right-hindlimb scratching of the head. The mouse then adopts a sitting posture and concomitant  
205 bilateral shoulder adduction brings both hands, with the left hand slightly in the lead, to the body midline.  
206 During adduction, the digits flex and close and contact the mouth. At stimulation termination, the hands are  
207 replaced on the floor and scratching with the right hindlimb resumes.

208 **Supplementary Video 8. A dorsal view of the Mouse Restaurant.** The mouse leaves the waiting area,  
209 proceeds down a corridor and steps down a small step to enter the dining area to find and eat a food pellet.

210 The mouse's movements are enabled by opening the "door" to allow access to the dining area and by  
211 positioning a "table", containing a food item e.g., food pellet, angel-hair pasta, in the dining area.

212 **Supplementary Video 9. Sunflower seed eating.** The mouse is able to pick up and eat the sunflower seed in  
213 the first session of sunflower seed eating.

214 **Supplementary Video 10. Husk-intact oat eating.** The mouse enters the dining area, picks up the oat seed  
215 from the floor, removes the skin, and eats it.

216 **Supplementary Video 11. Angel-hair pasta eating after RFO saline infusion.** After saline infusion (Rostral  
217 Forelimb Orofacial area), a mouse enters the dining area and finds a 15mm piece of angel-hair pasta. It sniffs  
218 and whisks the pasta and then directs its snout to an end of the pasta where with tongue/mouth movements it  
219 grasps the pasta with the incisors. Pasta positioning in the mouth induces the adoption of a sitting posture on  
220 the haunches and concurrent raising of both hands to grasp the pasta. Bilateral hand adjustments with  
221 assistance of the mouth position the pasta in the mouth in an oblique orientation for biting. The pasta is  
222 consumed by repeated acts of positioning, biting, and chewing mediated by coordinated oromaneal  
223 movements. The tracking of different body parts and the pasta are shown.

224 **Supplementary Video 12. Angel-hair pasta eating after RFO muscimol infusion in Mouse 1.** After  
225 muscimol infusion (Rostral Forelimb Orofacial area) Mouse 1 identifies the pasta by sniffing. It is clumsy in  
226 picking up the pasta by mouth, does not seek out the end of the pasta for mouth purchase, does not use its  
227 tongue/mouth to grasp the pasta and makes little use of its hands for food retrieval from the mouth or pasta  
228 manipulation. The pasta is consumed from the floor mainly using mouth movements.

229 **Supplementary Video 13. Angel-hair pasta eating after RFO muscimol infusion in Mouse 2.** After  
230 muscimol infusion (Rostral Forelimb Orofacial area) Mouse 2 identifies the pasta by sniffing, does not seek  
231 out the end of the pasta for tongue/mouth purchase, and picks it up in the middle with its mouth. It lifts the  
232 hands to grasp the pasta but fails to manipulate the pasta or remove it from its mouth to reorient it into a  
233 position for biting. The mouse ends up breaking the pasta in half.

234 **Supplementary Video 14. Fiber photometry during 15mm angel-hair pasta eating in a *Fezf2* mouse.**  
235 Top: A mouse sniffs angel-hair pasta (15mm), grasps it with its tongue, and manipulates it with its mouth and  
236 hands into a position for biting. Bottom: Fiber photometry of  $PTs^{Fefz2}$  in right Rostral Forelimb Orofacial area  
237 (RFO: black trace) and left aCFA (grey trace). Legend is the same as that in **Fig. 3c**. Note: relatively greater  
238 activity in RFO is associated with oromaneal movements of pasta eating.

239 **Supplementary Video 15. Fiber photometry during 15mm angel-hair pasta eating in a *PlxnD1* mouse.**  
240 Top: A mouse sniffs angel-hair pasta (15mm), grasps it with its tongue, and manipulates it with its mouth and  
241 hands into a position for biting. Bottom: Fiber photometry of  $ITs^{PlxnD1}$  in right Rostral Forelimb Orofacial  
242 area (RFO: black trace) and left aCFA (grey trace). Legend is the same as that in **Fig. 3c**. Note: RFO exhibits  
243 greater activity during eating and activity peaks are associated with oromaneal manipulation.

244 **Supplementary Video 16. Fiber photometry during 1mm angel-hair pasta eating in a *Fezf2* mouse.** Top:  
245 A mouse sniffs angel-hair pasta (1mm) and grasps it with its tongue for ingestion (circa 1.7 sec). Bottom:  
246 Fiber photometry of  $PTs^{Fefz2}$  in right RFO (black trace) and left aCFA (grey trace). Legend is the same as that  
247 in **Fig. 3n**.

248 **Supplementary Video 17. Fiber photometry during 1mm angel-hair pasta eating in a *PlxnD1* mouse.**  
249 Top: A mouse sniffs angel-hair pasta (1mm) and grasps it with its tongue for ingestion (circa 2.4 sec). Bottom:

250 Fiber photometry of ITs<sup>PlxnD1</sup> in right RFO (black trace) and left aCFA (grey trace). Legend is the same as  
251 that in **Fig. 3n**.

252 **Supplementary Video 18. Retrieval stage of pasta eating in a control trial.** A mouse grasps angel-hair  
253 pasta (15 mm) by orienting its head so that it can grasp the end of the pasta. The mouse then immediately  
254 adopts a sitting posture, uses its hands to take the pasta to help orient the pasta in its mouth. Using oromanual  
255 manipulation, it proceeds to bite pieces from the pasta.

256 **Supplementary Video 19. Optogenetic inhibition of RFO PNs<sup>Emx1</sup> during retrieval stage of pasta eating.**  
257 Optogenetic inhibition of RFO (Rostral Forelimb Orofacial area) PNs<sup>Emx1</sup> (4 sec duration top left; 15mm-  
258 angel hair pasta) starting with mouse entry to the dining area. The mouse does not orient the mouth to the end  
259 of the pasta and grasps the pasta with its mouth after the 5<sup>th</sup> attempt. It then immediately adopts a sitting  
260 posture and grasps the pasta with its hands, but does not orient its mouth to the end of the pasta but bites the  
261 pasta in its middle.

262 **Supplementary Video 20. Optogenetic inhibition of RFO PTs<sup>Fezf2</sup> during retrieval stage of pasta eating.**  
263 Optogenetic inhibition of RFO (Rostral Forelimb Orofacial area) PTs<sup>Fezf2</sup> (4 sec duration top left; 15mm-angel  
264 hair pasta) begins as the mouse enters the dining area. The mouse orients its mouth to the end of the pasta but  
265 only grasps the pasta after the 6<sup>th</sup> attempt. Once the pasta is grasped, the mouse immediately adopts a sitting  
266 posture and orients its mouth to the end of pasta to bite.

267 **Supplementary Video 21. Pasta-bite test.** Control trial in the pasta-bite test, in which a *Fezf2* mouse  
268 approaches, detects, orients its mouth, and successfully bites a piece of angel-hair pasta that projects  
269 horizontally from a holder located in the aperture.

270 **Supplementary Video 22. Pasta-bite test with RFO PTs<sup>Fezf2</sup> inhibition.** Optogenetic inhibition (PTs<sup>Fezf2</sup>;  
271 whole trial) of Rostral Forelimb Orofacial area does not affect approach, detection, head orient, and successful  
272 bite of a piece of angel-hair pasta that projects horizontally from a holder located in the aperture.

273 **Supplementary Video 23. Pasta-bite test with RFO ITs<sup>PlxnD1</sup> inhibition.** Optogenetic inhibition (ITs<sup>PlxnD1</sup>;  
274 whole trial) of Rostral Forelimb Orofacial area does not affect approach, detection, mouth orient, and  
275 successful bite of a piece of angel-hair pasta that projects horizontally from a holder located in the aperture.

276 **Supplementary Video 24. Control pasta-eating in the handle-eat stage.** The mouse makes coordinated  
277 oromanual movements to position and bite the 15mm-angel hair pasta.

278 **Supplementary Video 25. Optogenetic inhibition of RFO PNs<sup>Emx1</sup> during handle-eat stage of pasta-**  
279 **eating.** Optogenetic inhibition (PNs<sup>Emx1</sup>, 4 s - top white bar, 15mm-angel hair pasta) of the Rostral Forelimb  
280 Orofacial area disrupts pasta handling. Mouth orienting to the end of the pasta is interrupted so that eventual  
281 biting is directed to the middle of the pasta. Posture is maintained and hand manipulation continues.

282 **Supplementary Video 26. Optogenetic inhibition of RFO PTs<sup>Fezf2</sup> during handle-eat stage of pasta-**  
283 **eating.** Optogenetic inhibition of the Rostral Forelimb Orofacial area (PTs<sup>Fezf2</sup>, 4 s - top white bar, 15mm-  
284 angel hair pasta) alters pasta holding position of the support hand and impairs oromanual manipulation to  
285 bite/snap the pasta.

286 **Supplementary Video 27. Optogenetic inhibition of RFO ITs<sup>PlxnD1</sup> during handle-eat stage of pasta-**  
287 **eating.** Optogenetic inhibition of the Rostral Forelimb Orofacial area (ITs<sup>PlxnD1</sup>, 4 s - top white bar, 15mm  
288 angel hair pasta) alters pasta holding position of the support hand and impairs oromanual coordination to  
289 bite/snap the pasta.

290 **Supplementary Video 28. Anterograde axon projections of RFO ITs<sup>PlxnD1</sup>.** Whole-brain stacked images  
291 of Flp-activated eGFP virus injection in a *PlxnD1* mouse showing axons in cortical areas (e.g., MOs, MOp,  
292 SSp-ul, SSp-m, SSp-n, SSs, AId, and VISC) and the ventrolateral part of the striatum of both hemispheres. In  
293 addition, ITs<sup>PlxnD1</sup> projected bilaterally to the capsular part of the central amygdala nucleus. MOs, secondary  
294 motor area; MOp, primary motor area; AId, agranular insular area, dorsal part; SSp-ul, primary somatosensory  
295 area, upper limb; SSp-m, primary somatosensory area, mouth; SSp-n, primary somatosensory area, nose; SSs,  
296 secondary somatosensory area; VISC, visceral area; RFO, Rostral Forelimb Orofacial area; IT,  
297 intratelencephalic.

298 **Supplementary Video 29. Anterograde axon projections of RFO PTs<sup>Fefz2</sup>.** Whole-brain stacked images of  
299 Flp-activated eGFP virus injection in a *Fefz2* mouse showing axons mainly in the ventrolateral part of the  
300 ipsilateral striatum, thalamus (e.g., VAL, PO, and PF), lateral superior colliculus, pons, and medulla. The  
301 axons were mainly in the contralateral medulla and eventually crossed at the pyramidal decussation to  
302 innervate the spinal cord. VAL, ventral anterior-lateral complex of the thalamus; PO, posterior complex of  
303 the thalamus; PF, parafascicular nucleus; RFO, Rostral Forelimb Orofacial area; PT, pyramidal tract.

304 **Supplementary Video 30. Retrograde monosynaptic input tracing of RFO PTs<sup>Fefz2</sup>.** Whole-brain stacked  
305 images of rabies virus injection in a *Fefz2* mouse showing input cells mainly from cortical areas (e.g., MOs,  
306 MOp, SSp-ul, SSp-m, SSp-n, SSs, AId, and VISC) and the thalamus (e.g., VAL, PO, PCN, and VM). MOs,  
307 secondary motor area; MOp, primary motor area; AId, agranular insular area, dorsal part; SSp-ul, primary  
308 somatosensory area, upper limb; SSp-m, primary somatosensory area, mouth; SSp-n, primary somatosensory  
309 area, nose; SSs, secondary somatosensory area; VISC, visceral area; VAL, ventral anterior-lateral complex of  
310 the thalamus; PO, posterior complex of the thalamus; PCN, paracentral nucleus; VM, ventral medial nucleus  
311 of the thalamus; RFO, Rostral Forelimb Orofacial area; PT, pyramidal tract.

312 **Supplementary Video 31. Retrograde monosynaptic input tracing of RFO ITs<sup>PlxnD1</sup>.** Whole-brain  
313 stacked images of rabies virus injection in a *PlxnD1* mouse showing input cells mainly from cortical  
314 areas (e.g., MOs, MOp, SSp-ul, SSp-m, SSp-n, SSs, AId, and VISC) and the thalamus (e.g., VAL, PO,  
315 PCN, and VM). MOs, secondary motor area; MOp, primary motor area; AId, agranular insular area,  
316 dorsal part; SSp-ul, primary somatosensory area, upper limb; SSp-m, primary somatosensory area,  
317 mouth; SSp-n, primary somatosensory area, nose; SSs, secondary somatosensory area; VISC, visceral  
318 area; VAL, ventral anterior-lateral complex of the thalamus; PO, posterior complex of the thalamus;  
319 PCN, paracentral nucleus; VM, ventral medial nucleus of the thalamus; RFO, Rostral Forelimb  
320 Orofacial area; IT, intratelencephalic.

## METHODS

**Animals.** Adult male and female mice bred onto a C57BL/6J background were used in the experiments. Mice were housed under a 12-h light-dark cycle (7.00 to 19.00 light), with room temperature at 22 °C and humidity at 50%. The experimental procedures were approved by the Institutional Animal Care and Use Committee of Cold Spring Harbor Laboratory (CSHL) and Duke University and performed in accordance with the US National Institutes of Health (NIH) guidelines.

The *Fezf2-CreER*, *Fezf2-Flp*, *PlxnD1-CreER*, *Sema3E-CreER*, *Tcerg11-CreER*, *Tbr2-CreER*, and *Tle4-CreER* knock-in mouse driver lines, in which the expression of the inducible Cre recombinase (CreER) or Flp are driven by endogenous promoters, were generated as previously described<sup>38</sup>. The *Emx1-Cre* knock-in mouse driver line was purchased from Jackson Laboratory (005628). The *Thy1-ChR2* transgenic line 18 (*Thy1-Tg18*) was a gift from Dr. Dinu Florin Albeanu at CSHL. The *Rosa26-loxp-stop-loxp-flpo* (*LSL-Flp*) reporter mice were in-house derived. The *Ai14* (*Rosa26-LSL-tdTomato*), *Ai32* (*Rosa26-LSL-ChR2-eYFP*), *Ai148* (*TIGRE-TRE2-LSL-GCaMP6f-LSL-tTA2*), and *Snap25-LSL-2A-EGFP-D* reporter mice were purchased from Jackson Laboratory (*Ai14*, 007908; *Ai32*, 024109; *Ai148*, 030328; *Snap25-LSL-2A-EGFP-D*, 021879). CreER or Cre driver mice were crossed with *Ai32* or *Ai148* reporter mice for optogenetic stimulation and fiber photometry respectively.

**Viral vectors.** The AAV9-Ef1a-DIO-ChR2-eYFP and AAV9-syn-FLEX-jGCaMP7f-WPRE were purchased from Addgene. The AAV2/8-Ef1a-fDIO-TVA-mCherry, AAV2/8-Ef1a-fDIO-TVA-eGFP, and AAVDJ-DIO-GtACR1-eYFP were produced in house. The AAV8-hSyn-FLEX-TVA-P2A-eGFP-2A-oG and EnVA-dG-Rabies-mCherry were purchased from Salk GT3 Vector Core (La Jolla, California). All viral vectors were aliquoted and stored at -80 °C until use.

**Stereotaxic surgery.** Mice, anesthetized with isoflurane (2-5 % at the beginning and 0.8-1.2 % for the rest of the surgical procedure), were positioned in a stereotaxic frame and their body temperature was maintained at 34-37 °C with a heating pad. Lidocaine (2%) was applied subcutaneously to the scalp prior to surgery. Ketoprofen (5 mg/kg) was administered intraperitoneally (IP) as an analgesic before and after surgery. A vertical incision was made through the scalp and connective tissue to expose the dorsal surface of the skull. The skin was pushed aside, and the skull surface was cleared using saline. A digital mouse brain atlas, linked to the stereotaxic frame, guided the identification and targeting of different brain areas (Angle Two Stereotaxic System, Leica Biosystems). Coordinates for injections and/or implantations in the RFO were 1.5-1.88 mm anterior from Bregma, 2.25-2.63 mm lateral from the midline; aCFA: 0.5 mm anterior from Bregma, 1.5 mm lateral from the midline.

For viral injection, a small burr hole was drilled in the skull and brain surface was exposed. A pulled glass pipette, with a tip of 20-30 µm, containing the viral suspension was lowered into the brain. A 300-400 nl volume was delivered at a rate of 10-30 nl/min using a Picospritzer (General Valve Corp). The pipette remained in place for 5 min, to prevent backflow, prior to retraction. Injections were made at depths of 0.3 and 0.6 mm for *PlxnD1* mice, 0.5 and 0.8 mm for *Fezf2* mice, and 0.3, 0.6, and 0.8 mm for *Emx1* mice. The incision was closed with Tissueglue (3M Vetbond) or 5/0 nylon suture thread (Ethilon Nylon Suture, Ethicon). The mice were kept warm on a heating pad during recovery.

For optogenetic activation, an optical fiber (diameter 200 µm; NA, 0.22 or 0.39) was implanted in the right RFO. For optogenetic inhibition, optical fibers (diameter 400 µm; NA, 0.37) were implanted bilaterally in the RFO. For fiber photometry, optical fibers (diameter 200 µm; NA, 0.39) were implanted in the right RFO and left aCFA. The optical fibers were implanted with their tips touching the brain

371 surface. For three *Fezf2* mice used for fiber photometry, the optical fibers were implanted at a depth of  
372 400 and 500  $\mu\text{m}$  from the cortical surface in the aCFA and RFO respectively. For drug infusion, two  
373 stainless-steel guide cannulae (24-gauge, 62002, RWD Life Science) were implanted bilaterally into the  
374 RFO 0.3 mm below the brain surface. To fix the implants to the skull, a silicone adhesive (Kwik-Sil,  
375 WPI) was applied to cover the hole, followed by a layer of dental cement (C&B Metabond, Parkell),  
376 black instant adhesive (Loctite 426), and dental cement (Ortho-Jet, Lang Dental). A titanium head bar  
377 was fixed to the skull near Lambda using dental cement. A plug cannula (62102, RWD Life Science)  
378 was inserted into the guide cannula to prevent clogging and reduce the risk of infection.

379  
380 For thin-skull window preparation, the skull of the right hemisphere was thinned in a 6 mm  $\times$  3 mm  
381 window preparation (+/- 3 mm AP from Bregma, 3 mm lateral to Bregma) using a micro drill until brain  
382 vasculature became visible after saline application. Bregma was then marked in blue. A thin layer of  
383 translucent dental cement (C&B Metabond, Parkell) was applied to the thinned skull, followed by nail  
384 polish. A titanium head bar was fixed to the skull near Lambda using dental cement (Ortho-Jet, Lang  
385 Dental).

386  
387 **Tamoxifen induction.** Tamoxifen (T5648, Sigma) was dissolved in corn oil (20 mg/ml) by stirring with  
388 a magnetic bead at room temperature overnight or by applying a sonication pulse for 60 s, followed by  
389 constant rotation overnight at 37 °C. Individual aliquots (1.5 ml each) were stored at 4 °C. For viral  
390 injected CreER driver mice, tamoxifen induction was performed via intraperitoneal injections at a dose  
391 of 100 mg/kg. The first induction was given one day after the viral injection and subsequent inductions  
392 were given once every 2 days for 2-3 times. To drive the reporter gene expression, mice were injected  
393 (IP, 100-200 mg/kg) 2-3 times at P21, 28, and/or 35. To identify embryonic day 17 (E17) for tamoxifen  
394 induction, female and male mice were housed together overnight and females were checked for a  
395 vaginal plug between 8-9 am the following morning. Following light isoflurane anesthesia, pregnant  
396 females were given oral gavage administration of tamoxifen (dose: 3 mg / 30 g of body weight) at  
397 gestational day E17.  
398

399  
400 **Immunohistochemistry.** Adult mice were anaesthetized (using 2.5% Avertin) and intracardially  
401 perfused with 25-30 ml PBS followed by 25-30 ml 4% paraformaldehyde (PFA) in 0.1 M PB. After  
402 overnight post-fixation at 4 °C, brains were rinsed three times with PBS and sectioned at a thickness of  
403 50-75  $\mu\text{m}$  with a Leica 1000s vibratome. Sections were placed in a blocking solution containing 10%  
404 normal goat serum (NGS) and 0.1% Triton-X100 in PBS1X for 1.5 h, then incubated overnight at 4 °C,  
405 or room temperature, with primary antibodies diluted in the blocking solution. Sections were rinsed  
406 three times (10 min each) in PBS and incubated for 2h at room temperature with corresponding  
407 secondary antibodies. Sections were dry-mounted on slides using Fluoromount-G mounting medium  
408 (0100-01, SouthernBiotech). Primary antibodies of chicken anti-GFP (1:1,000 or 1:500, Aves, GFP-  
409 1020) and rabbit anti-RFP (1:1,000 or 1:500, Rockland Pharmaceuticals, 600-401-379) were used. Alexa  
410 Fluor dye-conjugated IgG secondary antibodies (1:500, Molecular Probes, catalog number A11039 for  
411 goat anti-chicken 488, A11012 for goat anti-rabbit 594) were used. In some instances, sections were  
412 incubated with Neurotrace fluorescent Nissl stain (1:300, Molecular Probes, catalog number N21479) or  
413 DAPI (1:1,000, Thermo Scientific, 62248) in secondary antibody. Imaging was performed using a Zeiss  
414 Axioimager M2 fluorescence microscope, Zeiss LSM 780 or 710 confocal microscopes, or Zeiss Axio  
415 Vert.A1 microscope.  
416  
417

418  
419 **Retrograde monosynaptic rabies tracing.** To map brain-wide monosynaptic inputs onto  $\text{PTs}^{\text{Fezf2}}$  and  
420  $\text{ITs}^{\text{PlxnD1}}$  in the RFO, we first injected the *Fezf2-CreER* or *PlxnD1-CreER* mice with the starter virus of

421 AAV8-hSyn-FLEX-TVA-P2A-eGFP-2A-oG (0.3  $\mu$ l) in the right RFO. Tamoxifen induction was  
422 performed via intraperitoneal injections at a dose of 100 mg/kg, once every 2 days for 3 times (the first  
423 induction was one day after the starter virus injection). Three weeks after the AAV injection, mice were  
424 injected in the RFO with EnVA-dG-Rabies-mCherry (0.4  $\mu$ l). Brain tissue was prepared for histologic  
425 examination 7-10 days after the rabies virus injection.

426  
427 Rabies injected brains were imaged either with a Zeiss Axioimager M2 fluorescence microscope or with  
428 whole-brain STP tomography. For the wide-field epi-fluorescence imaging, 75- $\mu$ m coronal sections  
429 were obtained across the anteroposterior axis of the brain and every other section was quantitatively  
430 analyzed. RFP-labeled (that is, rabies-labeled) input cells were automatically detected, and brain slices  
431 were registered to the reference Allen Brain Atlas using Serial Section Registration  
432 (<http://atlas.brainomatics.org/a/ssr2021>)<sup>78</sup>. False- and miss-labeled cells were corrected manually. Data  
433 are presented as the ratio between the number of RFP-labeled cells in each brain area and the total  
434 number of RFP-labeled cells across the entire brain.

435  
436  
437 **Whole-brain STP tomography.** We used the whole-brain STP tomography pipeline previously  
438 described<sup>38</sup>. Perfused and post-fixed brains, prepared as described above, were embedded in 4%  
439 oxidized agarose in 0.05 M PB, cross-linked in 0.2% sodium borohydrate solution (in 0.05 M sodium  
440 borate buffer, pH 9.0-9.5). The entire brain was imaged in coronal sections with a 20 $\times$  Olympus  
441 XLUMPLFLN20XW lens (NA 1.0) on a TissueCyte 1000 microscope (Tissuevision) with a Chameleon  
442 Ultrafast-2 Ti:Sapphire laser (Coherent). EGFP/EYFP or tdTomato/mCherry signals were excited at 910  
443 nm or 920 nm, respectively. Whole-brain image sets were acquired as series of 12 (x)  $\times$  16 (y) tiles with  
444 1  $\mu$ m  $\times$  1  $\mu$ m sampling for 230-270 z sections with a 50- $\mu$ m z-step size. Images were collected by two  
445 PMTs (PMT, Hamamatsu, R3896) using a 560 nm dichroic mirror (Chroma, T560LPXR) and band-pass  
446 filters (Semrock, FF01-680/SP-25). The image tiles were corrected to remove illumination artifacts  
447 along the edges and stitched as a grid sequence. Image processing was completed using Fiji software  
448 with linear level adjustments applied only to entire images.

449  
450  
451 **Axon detection from whole-brain STP data.** For axon projection mapping, PN axon signal based on  
452 cell-type specific viral expression of EGFP or EYFP was filtered by applying a square root  
453 transformation, histogram matching to the original image, and median and Gaussian filtering using  
454 Fiji/ImageJ software to maximize signal detection while minimizing background auto-fluorescence<sup>38</sup>. A  
455 normalized subtraction of the autofluorescent background channel was applied and the resulting  
456 thresholded images were converted to binary maps. Projections were quantified as the fraction of pixels  
457 in each brain structure relative to each whole projection.

458  
459  
460 **Registration of whole-brain STP image datasets.** Registration of brain-wide datasets to the Allen  
461 reference Common Coordinate Framework (CCFv3) was performed either by 3D affine registration  
462 followed by a 3D B-spline registration using Elastix software, according to established parameters<sup>38</sup> or  
463 by brainreg software<sup>79,80</sup>. For axon projection analysis, we registered the CCFv3 to each dataset to  
464 report pixels from axon segmentation in each brain structure without warping the imaging channel.

465  
466  
467 **Axon-projection and monosynaptic-input diagrams from whole-brain imaging data.** To generate  
468 diagrams of axon projections and monosynaptic inputs for a given driver line, axon- and cell-detection  
469 outputs from all individual experiments were compared (sorting the values from high to low) and  
470 analyzed side-by-side with low-resolution image stacks (and the CCFv3 registered to the low-resolution

dataset for brain area definition) to get a general picture of the injection and high-resolution images for specific brain areas.

**In vivo electrophysiology and data analysis.** The surgery is described in previous sections. To provide a ground reference, an M1 screw connected to a silver wire (A-M systems) was implanted into the skull above the left visual cortex during surgery.

Before the first recording session, a craniotomy was made in the secondary motor cortex (MOs, A: 1.6 mm; L: 1.4 mm) under isoflurane anesthesia. A silicon probe (ASSY-37 H4, Cambridge NeuroTech, or A1x32-5mm-25-177, A4x8-5mm-100-200-177, NeuroNexus) was slowly lowered into the cortex using a micromanipulator (MP-285, Sutter Instrument). A silicone adhesive (Kwik-Sil, World Precision Instruments) was applied over the craniotomy to stabilize the exposed brain. The brain was allowed to settle for 15-30 minutes before recording began. Voltage signals were continuously recorded at 32 kHz from all 32 channels of the silicon probe by a Digital Lynx 4SX recording system (Neuralynx). Raw data were collected and saved using Cheetah software. The neuronal activity in different channels was band-pass filtered (300-6,000 Hz) for real-time visualization. For optical tagging, 473-nm blue light pulses (2-ms or 5-ms duration) at different frequencies (0.1 or 10 Hz) were delivered through an optical fiber over the craniotomy. At the end of the session, the probe was retracted, and the craniotomy was covered with the silicone adhesive to allow a subsequent recording session on the following day.

Raw data were rearranged according to probe configurations, median-subtracted across channels and time, and saved in 16-bit binary files for spike detection and sorting using Kilosort software (<https://github.com/cortex-lab/KiloSort>). We used default parameters from KiloSort2 for spike detection and sorting, and further manually curated the spike clusters in phy2 (<https://github.com/cortex-lab/phy>). Sorted data were analyzed using custom MATLAB codes. Several parameters were taken into consideration for cluster quality control: spike shape, average spike firing frequency ( $> 0.05$ ), amplitude ( $> 60$  mV), contamination rate ( $< 0.2$ ), and isolation distance ( $> 18$ ). Peri-event raster plots and histograms were used to visualize the light evoked spikes from Ai32 crossed mice.

**Optogenetic motor mapping.** Optogenetic motor mapping techniques were adapted from those previously described (**Fig. 1b**)<sup>36,37,81</sup>. We briefly anesthetized the mice with isoflurane (2%) to attach a reflective marker on the back of the left hand and to paint their jaw red. Mice were then transferred into a tube, head fixed on a mapping stage, and allowed to fully recover from the anesthesia before stimulation began. The thin-skull window was cleaned with a duster and covered with silicone oil (378399, Sigma-Aldrich). We used a 2D motorized stage (ASI, MS-2000) controlled by MATLAB programs to localize the stimulation at different cortical sites. A 473-nm laser (5-ms pulses, 10 or 50 Hz, 5-20 mW) was used to pseudo-randomly stimulate (100-ms or 500-ms duration) a grid of 128 programmed sites at intervals of 375  $\mu\text{m}$ . A plano-convex lens (focal length (FL) = 250 mm, LA1301-A, Thorlabs) coupled with a SLR photon lens (Voigtlander Nokton, 35 mm FL, f/1.2) was used to collimate the laser beam. The diameter of the laser beam was  $\sim 230$   $\mu\text{m}$  ( $1/e^2$  diameter). A dichroic mirror (Chroma T495lpxr-UF2, round, 2-inch diameter) was used to guide the laser beam to the tissue. Two SLR lenses (the same Nokton 35 mm FL and a Nikkor 105 mm FL, f/2.0, AF), coupled front to front, were used to image the thin-skull window onto the CMOS sensor of a camera (MV1-D1312-40-G2-12, Photonfocus) with a pixel size of 2.67  $\mu\text{m}$ . Bregma was used as the coordinate reference. Each site was stimulated 15-20 times per session. The inter stimulation interval was 2 s. Two cameras (FL3-U3-13E4C-C, FLIR), positioned at the front and the side of the animal, were used to take videorecordings at a frame rate of 100 Hz. The videos were time aligned by TTL signals controlled by the MATLAB programs. The video and TTL-signal states were acquired using workflows in Bonsai software. Four LED light lamps were

521 used for illumination (2 for each camera). After mapping, the thin-skull window was covered with  
522 silicone sealant (Kwik-Cast, WPI) for protection and later mapping.

523  
524  
525 **In vivo optogenetic activation.** For head-fixed activation, mice injected with ChR2 virus in the right  
526 RFO were prepared and video recorded as described above. A fiber coupled laser (5-ms pulses, 5-20  
527 mW;  $\lambda = 473$  nm) was used to apply stimulation at 10, 20, 30, and 50 Hz and constantly for 0.5 s.  
528 For free-moving activation, mice with an optical fiber implanted in the right RFO were placed into an  
529 acrylic activity box (14 cm  $\times$  14 cm  $\times$  16.5 cm, L  $\times$  W  $\times$  H). A 473-nm laser (5-ms pulses, 5-20 mW)  
530 coupled to a rotary joint (RJPFL2, Thorlabs) was used to apply stimulation at 10, 20, and 50 Hz and  
531 constantly for 0.5 s. Three cameras (FL3-U3-13S2C-CS, FLIR) were used to take video records at a  
532 frame rate of 120 Hz from two sides and the bottom of the activity box. LED light lamps adjacent to  
533 each camera provided illumination.

534  
535  
536 **Video analysis for motor mapping and optogenetic activation.** Videos of behavior from the motor  
537 mapping and head-fixed activation were analyzed either with MATLAB programs or DeepLabCut<sup>45</sup>.  
538 The two cameras were calibrated using the Camera Calibrator App in MATLAB. For hand and jaw  
539 tracking in MATLAB, the images were smoothed with a Gaussian low-pass filter (size 9, sigma 1.8).  
540 The centroid of the reflective marker on the hand and the tip of the painted jaw were detected by a  
541 combination of brightness and hue thresholding, then tracked by a feature-based tracking algorithm  
542 (PointTracker in Computer Vision Toolbox). The tracking results were validated manually and errors  
543 were corrected accordingly. For DeepLabCut training, 525 images were used from the frontal video  
544 record and 700 images were used from the side video record to track the movements of the jaw and  
545 hands. Trials in which mice made spontaneous movements before stimulation onset (within 0.5 s) were  
546 excluded from the analyses, based on either manual examinations or setting threshold ( $3 \times$  s.d. from the  
547 mean) on average speed and acceleration distributions of all trials.

548  
549 For videos obtained from free-moving activation, the tracking of different body parts was performed  
550 using DeepLabCut. The network was trained with 800 images. Eight body parts (left and right eyes,  
551 hands, ankles, nose, and tail base) were labeled in the images. The behavioral videos and tracking results  
552 were visualized and analyzed in a custom-written MATLAB app. Tracking errors were corrected using  
553 the app.

554  
555 The spatial dispersion (SD) of hand positions at the end of optogenetic activation was computed as  
556 follows:

$$SD = \frac{1}{n} \sum_{i=1}^n \sqrt{(x_i - \bar{x})^2 + (y_i - \bar{y})^2 + (z_i - \bar{z})^2},$$

558 where  $\bar{x}$ ,  $\bar{y}$ , and  $\bar{z}$  are mean positions for each axis.

559  
560 To quantify the hand-to-mouth movement induced by optogenetic activation in the head-fixed animals,  
561 we examined the videos from the cortical site that featured the shortest distance between the hand and  
562 the nose following the activation (coordinates for 13 *Fezf2* mice:  $1.24 \pm 0.12$  mm anterior from Bregma,  
563  $2.39 \pm 0.09$  mm lateral from the midline; 7 *PlxnD1* mice:  $1.66 \pm 0.14$  mm anterior from Bregma,  $2.46 \pm$   
564  $0.11$  mm lateral from the midline). Criteria for labeling hand-to-mouth movement were: (1) a forelimb  
565 movement that brought the hand to the mouth; (2) a wrist supination; (3) a flexion of the digits. Any  
566 intervening grooming movements were not scored as hand-to-mouth movements. We labeled head-to-  
567 hand movement by examining the videos from free-moving animals receiving optogenetic stimulation.  
568 A head movement that brought the mouth toward the hand contralateral to the stimulation site was  
569 defined as a head-to-hand movement.

570  
571  
572  
573  
574  
575  
576  
577  
578  
579  
580  
581  
582  
583  
584  
585  
586  
587  
588  
589  
590  
591  
592  
593  
594  
595  
596  
597  
598  
599  
600  
601  
602  
603  
604  
605  
606  
607  
608  
609  
610  
611  
612  
613  
614  
615  
616  
617  
618

**Angel-hair pasta eating behavior.** Mice given ad libitum access to water were food restricted until they reached 80 to 85% of their initial body weight. Food restriction began at least 4 days after surgery. Each day during food restriction, the mice were fed food pellets (0.3-3.5 g of 14 mg Dustless Precision Pellets, F05684, Bio-Serv) to maintain body weight. Most behavioral experiments began after the third day of food restriction, at which time body weights had reached the target level.

Feeding behavior of mice was studied in an automated Mouse Restaurant (**Fig. 2a, Extended Data Fig. 4a, b**). The apparatus has two areas, a dining area (10 cm × 10 cm × 15 cm, dimensions L × W × H) and a waiting area (15 cm × 15 cm × 15 cm), connected by a corridor (24 cm × 4 cm × 15 cm). Food items were placed on a 3D-printed plate mounted on an XZ motorized stage. The plate was moved from the dining area to a food dispenser by two stepper motors (PD42-3-1070, Trinamic Motion Control). The food dispenser, made with two stacked 3D-printed plates, placed a food item onto the table. Each of the two plates, driven by a stepper motor (NEMA-17, 324, Adafruit), could hold 24-food items, such that 48-food items can be provided in the dining area in each session. An acrylic door in the corridor was opened by a servo motor (D625MW, Hitec) to allow access to the dining area from the waiting area. In this way, mice left the waiting area entered the dining area to eat, and after eating returned to the waiting area where water was accessible from a water port in a corner. Two pairs of infrared (IR) break-beam sensors (2168, Adafruit) installed at each end of the corridor detected the movement direction of the mice. An elevated step fixed between the corridor and the dining area kept food items from being swept out of the dining area. Once mice returned to the waiting area, the door was closed, a new food item was presented and the next trial began. A session ended after all 48-food items were presented or 40 minutes elapsed. The apparatus was controlled by codes running on an Arduino Mega 2560 Rev3 (A000067, Arduino) with three shields (IO sensor shield, DFR0165, DFRobot; LCD and motor shield, 772 and 1438, respectively, Adafruit). An Arduino Uno Rev3 (A000066, Arduino), with three shields (screw shield, DFR0171, DFRobot; LCD and data logging shield, 772 and 1141, respectively, Adafruit), took signals from the IR break-beam sensors to control a laser for optogenetic stimulation and to send TTL signals to recording devices for time alignment.

The mice were pretrained to shuttle between the waiting area and the dining area for one session each day for 2-3 days, were they consumed 30-48, 20-mg pellets (Dustless Precision Pellets, F0163, Bio-Serv). On the day before a pasta-eating session, the mice were familiarized with 0.5 g of angel-hair pasta in their home cage. On the following day, 15-mm pasta pieces were loaded into the food dispenser before the session by inserting them into 3D-printed holders (10 mm × 10 mm × 2 mm, L × W × H, with a 1.5 mm diameter hole in the middle, **Extended Data Fig. 4b, d**). In the test sessions, the mice consumed 24-48 pieces of 15-mm pasta. During 1-2 sessions, concurrent fiber photometry was obtained. During 6-8 sessions, optogenetic inhibition was applied. At the completion of the 15-mm pasta-eating tests, mice received a training session in which they received 1-mm angel-hair pasta that had been manually placed on the table. Then photometry was obtained over two sessions during which 15-mm and 1-mm pasta lengths, cut using a custom-designed plate, were presented in an alternating order.

**Pasta-bite test.** Following the 15-mm pasta-eating sessions, mice used in optogenetic inhibition sessions were given a pasta-bite test. A 20-mm piece of angel-hair pasta was inserted into a metal tube and fixed in place by a screw. The apparatus was located in an aperture (15 mm × 15 mm × 15 mm, L × W × H) made of clear acrylic (**Extended Data Fig. 11a**). A mouse inserted its head into the aperture and bit off pieces of pasta (~ 3 mm). One training session was given before the inhibition session. After each trial, mice returned to the waiting area, a new piece of pasta was placed in the holder, and the next trial began.

619 The mice learned to bite the pasta in the first session after which, 1-2 sessions were given with  
620 optogenetic inhibition.

621  
622  
623 **Video recording for pasta eating and data analysis.** Three cameras, one on each side of the dining  
624 area, video recorded (120 Hz, FL3-U3-13S2C-CS, FLIR) behavior in the dining area. Each camera was  
625 fitted with a varifocal lens (T10Z0513CS, Computar). The cameras were time aligned by the TTL  
626 signals sent by the Arduino Uno Rev3. The videos and TTL-signal states were acquired using workflows  
627 in Bonsai software. Four LED light lamps placed around the dining area provided illumination. For fiber  
628 photometry, long-pass filters (590 nm, FGL590S, Thorlabs) were installed on the light lamps. A  
629 webcam (C920, Logitech) was installed on a post to monitor the mice from a dorsal perspective.

630  
631 The cameras were calibrated using Camera Calibrator App in MATLAB and 12,623 images were pooled  
632 to train a deep neural network for tracking using DeepLabCut. Ten body parts (left and right eyes,  
633 hands, ankles, nose, tongue, jaw, and tail base) and the pasta (top, center, and bottom) were labeled in  
634 the images. The behavioral videos and tracking results were visualized and analyzed in a custom-written  
635 MATLAB app.

636  
637 In the app, we labeled action motifs and sensorimotor events manually through a frame-by-frame  
638 analysis (**Extended Data Fig. 5**). Images from all three cameras were displayed for each frame and  
639 about 4 million frames were labelled. We identified the start and end frames for the following action  
640 motifs: jaw retrieve, tongue lick, left- and right-hand reach, sit, left- and right-hand adjustment. The start  
641 frame defined movement initiation and the stop frame defined movement completion. Food-in-mouth  
642 events were labeled once the pasta was clearly lifted from the floor by the mouth. A hand withdraw  
643 event was labeled as a mouse raised its hands toward the mouth after chewing. A feeding-end event was  
644 labeled when mice lowered their bodies to the floor after food consumption. For saline and muscimol  
645 infusion sessions, events in which pasta was dropped were additionally labeled.

646  
647 In addition to manual labelling, hand-withdraw events and the onsets of chewing were identified with a  
648 two-state hidden Markov model (<https://www.cs.ubc.ca/~murphyk/Software/HMM/hmm.html>) using  
649 normalized distances of the left- and right-hand to the nose. The model was trained on data from each  
650 session with ten random initializations. Only distances from the first bite to the last bite in each trial  
651 were used for the training. The model with the largest log likelihood was used to classify the handle-bite  
652 and chew states. A hand-withdraw event was computed as the transition point from a chew state to a  
653 handle-bite state. Conversely, the onset of chewing was computed as the transition point from a handle-  
654 bite state to a chew state.

655  
656 To estimate the time of pasta detection, we first computed the distances from the nose to the top, center,  
657 and bottom of the pasta at each onset of pasta retrieval in the control trials. The shortest nose-to-pasta  
658 distance at each pasta-retrieval onset was saved. The average shortest distance was used as the pasta-  
659 detection distance and computed separately for each mouse. The first time point at which the shortest  
660 nose-to-pasta distance drops below the pasta-detection distance was used as pasta-detection time and  
661 computed for all trials.

662  
663 We used Hellinger distance to quantify the similarity between two probability distributions of pasta  
664 orientations. For two probability distributions  $P = (p_1, \dots, p_k)$  and  $Q = (q_1, \dots, q_k)$ , their Hellinger distance  
665 is computed as:

$$H(P, Q) = \frac{1}{\sqrt{2}} \sqrt{\sum_{i=1}^k (\sqrt{p_i} - \sqrt{q_i})^2}.$$

To analyze the phase of hand movements, we first computed the Z-axis movement trajectory using ankle position as a reference. The movement trajectory was band-pass filtered (0.4 - 10 Hz) with forward-backward-zero-phase FIR filters. Hilbert transform was then used on the filtered trajectory to acquire instantaneous phases of the movement. A vector summation was used to obtain the average phase at the time of a bite and the selectivity index of phases:

$$R = \frac{\sum_k e^{i\theta_k}}{k},$$

where  $\theta_k$  is the phase at the time of a bite. The complex phase and amplitude of the resultant R represent the average phase and selectivity index respectively.

To determine how the bite was made, we used a head-based coordinate system (**Fig. 4k**). The right eye defined the coordinate origin. The X'Y' plane was defined by the plane where the nose and both eyes reside. The X' axis crossed both eyes pointing toward the left eye; the Y' axis pointed to the direction that was opposite to the nose; the Z' axis pointed outward from the mouse's body. The coordinates of the left eye, left and right hands, nose, and top and bottom of the pasta in the head-based coordinate system were computed by linear transformations. The analysis of bite location indicated that a mouse bites the pasta at a same location inside its mouth (**Extended Data Fig. 13a, b**). We thus assumed that the coordinates of the corresponding bite location in a 2D plane (e.g., X'Y' plane) are (a, b). Let (x1, y1) and (x2, y2) be the top and bottom coordinates of the pasta, respectively, at the time of a bite (**Extended Data Fig. 13c**). Given the line defined by the pasta passes through the bite location, we have,

$$m = \frac{y1-y2}{x1-x2}, \quad (1)$$

$$\frac{y1-b}{x1-a} = m, \quad (2)$$

where m is the slope of the line. Let  $y = y1 - mx1$ ,  $x = -m$ , Eq. 2 can be rewritten as  $y = ax + b$ , which indicates that the x and y, transformed from the top and bottom coordinates of the pasta, have a linear relationship. The experimental data support the assumption that mouse bites the pasta at a same location inside its mouth (**Extended Data Fig. 13d, e, h**). The coordinates (a, b) of the bite location were computed by linear fitting and plotted on the corresponding 2D planes (**Extended Data Fig. 13f, g**). Using a diagram of the oral cavity of a mouse<sup>82</sup>, our computation of bite location corresponded with the incisor tips.

**Sound recording and signal analysis.** A microphone (AT803, Audio-Technica) on the wall of the dining area picked up the sound of pasta biting. The audio signal from the microphone was amplified (Studio Channel, PreSonus) and digitized at 96,000 Hz by a multifunctional I/O device (PCIe-6323, National Instruments) controlled by MATLAB programs. The TTL signal sent out by the Arduino Uno Rev3 was recorded for time alignment. To detect bite events, the audio signal was band-pass filtered (Butterworth filter, 800-8,000 Hz), rectified, smoothed with a Gaussian window (5 ms), and thresholded ( $3-5 \times$  s.d. from the mean).

**Muscimol infusion.** After performing 1-2 sessions of 15-mm angel-hair pasta eating, mice were infused with 0.9% saline or muscimol (1 mg/ml, in 0.9% saline) bilaterally into the RFO for two consecutive pasta-eating sessions (saline given for one session, muscimol for the next, or vice versa). Mice were head fixed on a stage and the two hemispheres were infused sequentially after removal of the plug cannula. The injection cannula (28-gauge, 62202, RWD Life Science) connected to a microsyringe (80330, Hamilton) was inserted into the guide cannula to deliver 0.5 or 1  $\mu$ l of the solution at a rate of 0.1 or 0.2  $\mu$ l/min by a syringe pump (Legato 130, KD Scientific). After the infusion, the injection cannula was left in place for 5 min to prevent backflow and then retracted, and the plug cannula was reinserted. At the end of the experiments, muscimol diffusion in the brain tissue was determined in two

716 mice by infusing fluorescent muscimol (BODIPY TMR-X Conjugate, 1 mg/ml, dissolved in 50%  
717 dimethyl sulfoxide in 0.9% saline; M23400, ThermoFisher Scientific) bilaterally into the RFO (0.5 and  
718 1  $\mu$ l in the left and right hemispheres respectively), with the same infusion procedure used for the pasta-  
719 eating sessions.

720  
721  
722 **In vivo optogenetic inhibition.** The implanted optical fibers were cleaned using alcohol swab sticks and  
723 connected to a rotary joint (FRJ\_1x2i\_FC-2FC, Doric Lenses) with two fiber patch cords (fiber core  
724 diameter, 200  $\mu$ m; RWD Life Science). A fiber coupled laser (5-15 mW;  $\lambda$  = 532 nm) controlled by the  
725 Arduino Uno Rev3 was used for the stimulation. For 15-mm angel-hair pasta eating sessions, the laser  
726 was turned on for 4 s at mouse entry into the dining area (early inhibition, from 0 s to 4 s) or 4 s after  
727 entry (late inhibition, from 4 s to 8 s). Thus, the late inhibition targeted oromanual handling. For late-  
728 inhibition sessions, control and inhibition trials in which mice didn't adopt a sit posture within 4 s were  
729 excluded from analysis. For the pasta-bite test, the laser was turned on at entry into the dining area and  
730 turned off at the return to the waiting area. Stimulation was given pseudo-randomly for half of the trials  
731 in each session.

732  
733  
734 **Fiber photometry and data analysis.** A commercial fiber photometry system (Neurophotometrics) was  
735 used to record calcium activity of PTs<sup>Fezf2</sup> and ITs<sup>PlxnD1</sup> in the right RFO and left aCFA at 20 Hz. A  
736 branching patch cord (fiber core diameter, 200  $\mu$ m; Doric Lenses) connected the photometry system  
737 with the implanted optical fibers. The intensity of the blue light ( $\lambda$  = 470 nm) for GCaMP excitation was  
738 adjusted to 20-50  $\mu$ W at the tip of the patch cord. A violet light ( $\lambda$  = 415 nm, 20-50  $\mu$ W at the tip) was  
739 used to acquire the isosbestic control signal to detect calcium-independent artifacts. Emitted signals  
740 were band-pass filtered and focused on the sensor of a CMOS camera. Photometry signals and  
741 behavioral events were aligned based on the TTL signals generated by the Arduino Uno Rev3. Mean  
742 values of signals from the two ROIs were calculated and saved by using Bonsai software, and were  
743 exported to MATLAB for further analysis.

744  
745 The recorded photometry signals were processed as previously described<sup>83,84</sup>. A baseline correction of  
746 each signal was made using the adaptive iteratively reweighted Penalized Least Squares (airPLS)  
747 algorithm (<https://github.com/zmzhang/airPLS>) to remove the slope and low frequency fluctuations in  
748 the signals. The baseline corrected signals were then standardized (Z-score) on a trial-by-trial basis  
749 using the median value and standard deviation of the baseline period (10.6 s, while mouse is waiting for  
750 food delivery). The standardized 415-nm excited isosbestic signal was fitted to the standardized 470-nm  
751 excited GCaMP signal using robust linear regression. The standardized isosbestic signal was scaled  
752 using parameters of the linear regression and regressed out from the standardized GCaMP signal to  
753 obtain calcium dependent signal.

754  
755 To compute the correlation coefficient between the hand-to-nose distance and GCaMP signal, we used  
756 the average of left- and right-hand to nose distances. The hand-to-nose distance was low-pass filtered (5  
757 Hz), shifted forward and backward in time, and downsampled to compute the correlation coefficients of  
758 different time lags from -1 s to 1 s. Data in the time window from the first bite to the last bite were used  
759 for the correlation analysis.

760  
761  
762 **Grip and bite strength analysis.** Bite strength was measured using an accurate single point load cell  
763 system (OEM Style Single Point Load Cells, Omega)<sup>85</sup>. The system was connected to a custom-built  
764 mouth piece with dimensions (H = 3 mm  $\times$  W = 5 mm  $\times$  L = 15 mm) based on the incisor morphology  
765 of adult C57BL6/J mice. Output signals were amplified (IN-UVI, Omega), digitized via a National

.766 Instruments board (PCIe-6323), and fed into a custom MATLAB-based computer interface. A mouse  
.767 was constrained in a 60-ml plastic tube with an opening on the top to accommodate the implanted  
.768 cannulae. To prevent the mouse from escaping, a plunger was inserted to loosely confine the mouse. A  
.769 mouth piece was presented manually and moved slowly at 0.5-1 cm/sec toward the mouth so that the  
.770 mouse could bite it. Bite strength was measured for 3-4 sessions (120-240 sec per session) for each  
.771 mouse.

.772  
.773 Forelimb grip strength was measured using a custom-designed 3D-printed metal bar (L = 8 cm, diameter  
.774 = 1.2 mm) attached to an accurate single point load cell system (OEM Style Single Point Load Cells,  
.775 Omega). The record of the output signal was acquired following a previously described protocol<sup>86</sup>. In  
.776 each of 3-4 tests, when a mouse grasped the bar with both hands, its tail was slowly pulled downward  
.777 with increasing pressure so that the mouse was required to increase its resistance.

.778  
.779  
.780 **Statistics and data presentation.** Significance levels used in the analyses and figures were: \*P < 0.05,  
.781 \*\*P < 0.01, \*\*\*P < 0.005, \*\*\*\*P < 0.001, with data presented as mean ± s.e.m., except where otherwise  
.782 indicated. In the statistical comparisons, data normality was checked with quantile plots and a Shapiro-Wilk  
.783 normality test in MATLAB. Non-normally distributed data were subsequently compared with non-  
.784 parametric tests. All statistical tests were two-tailed and adjustments were made for multiple comparisons.  
.785 No statistical methods were used to predetermine sample size, but our sample sizes are similar to those  
.786 reported in previous publications<sup>87,88</sup>.

.787  
.788  
.789 **Data availability.** The data that support the findings of this study are available from the corresponding  
.790 author upon reasonable request.

.791  
.792  
.793 **Code availability.** Custom-written scripts used in this study are available in a GitHub repository at  
.794 <https://github.com/XuAn-universe/Publication-source-code>.

795 **LIST OF ABBREVIATIONS**

796

797 ACAd, anterior cingulate area, dorsal part

798 AId, agranular insular area, dorsal part

799 APN, anterior pretectal nucleus

800 CB, cerebellum

801 CEAc, central amygdalar nucleus, capsular part

802 CL, central lateral nucleus of the thalamus

803 CP, caudoputamen

804 FRP, frontal pole

805 GPe, globus pallidus, external segment

806 GPi, globus pallidus, internal segment

807 GRN, gigantocellular reticular nucleus

808 GU, gustatory areas

809 HPF, hippocampal formation

810 HY, hypothalamus

811 IRN, intermediate reticular nucleus

812 MD, mediodorsal nucleus of the thalamus

813 MdD, medullary reticular nucleus, dorsal part

814 MDRN, medullary reticular nucleus

815 MdV, medullary reticular nucleus, ventral part

816 MOp, primary motor area

817 MOs, secondary motor area

818 MRN, midbrain reticular nucleus

819 OLF, olfactory areas

820 ORBl, orbital area, lateral part

821 PAL, pallidum

822 PARN, parvicellular reticular nucleus

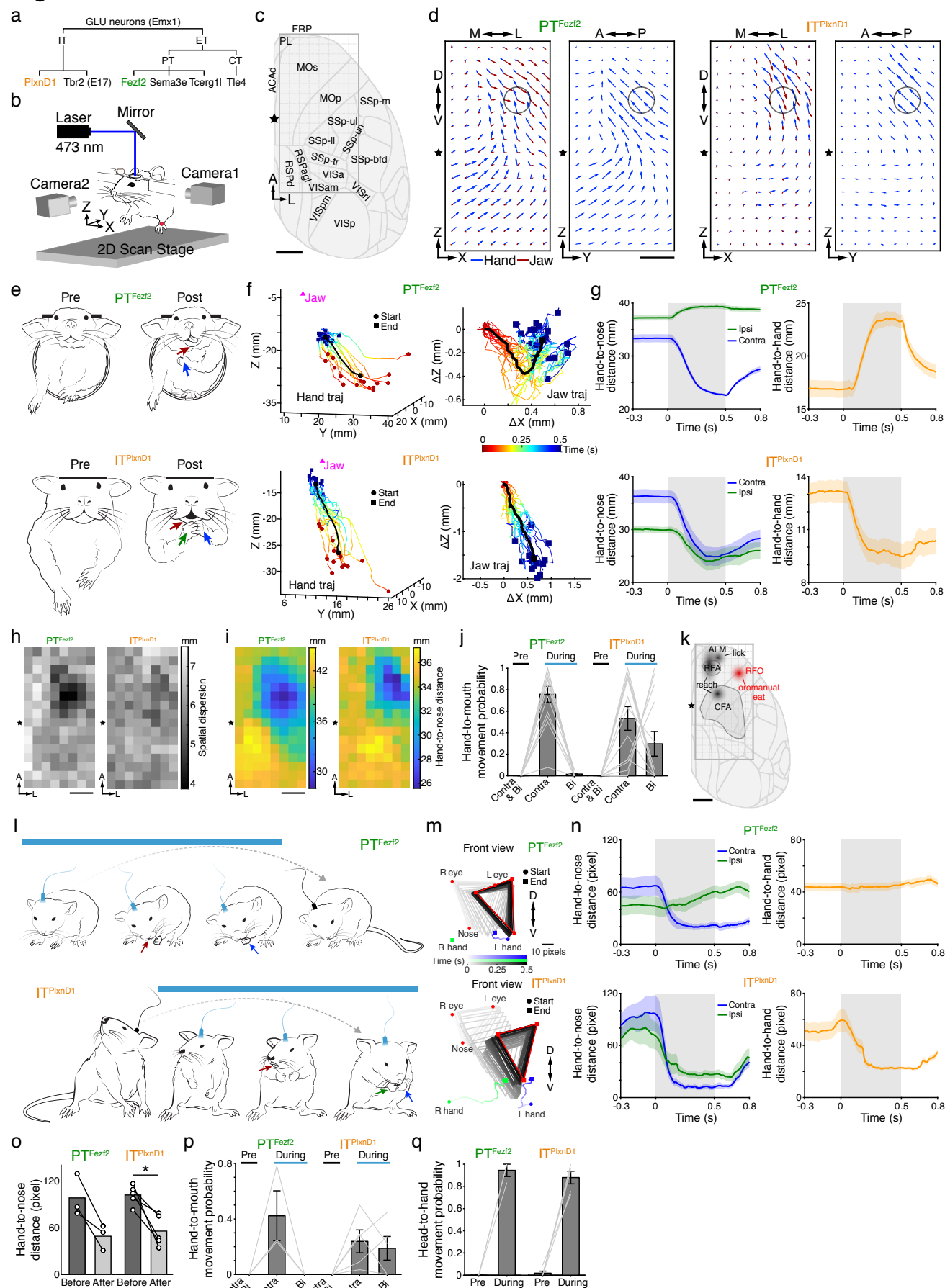
823 PCN, paracentral nucleus

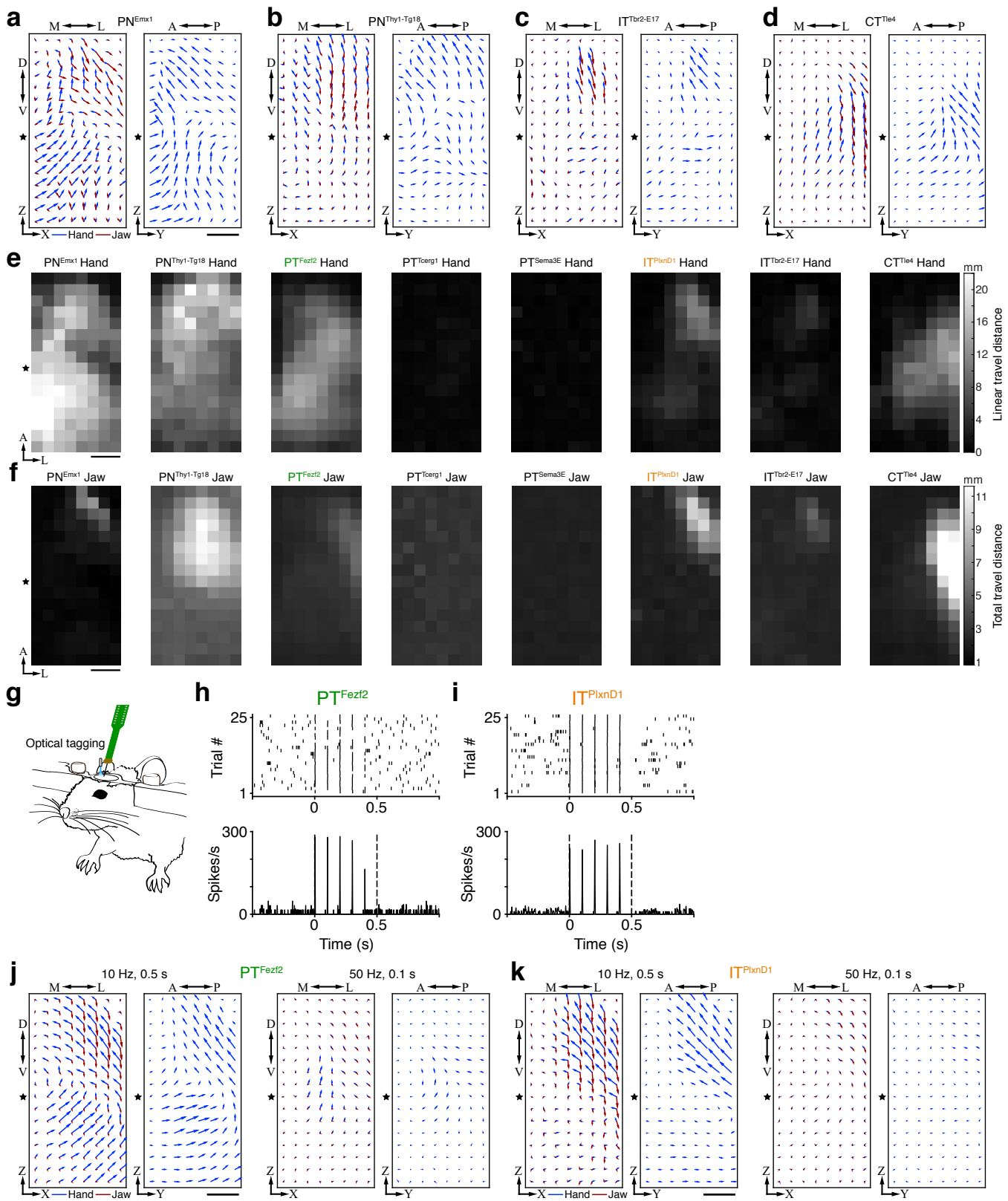
824 PF, parafascicular nucleus

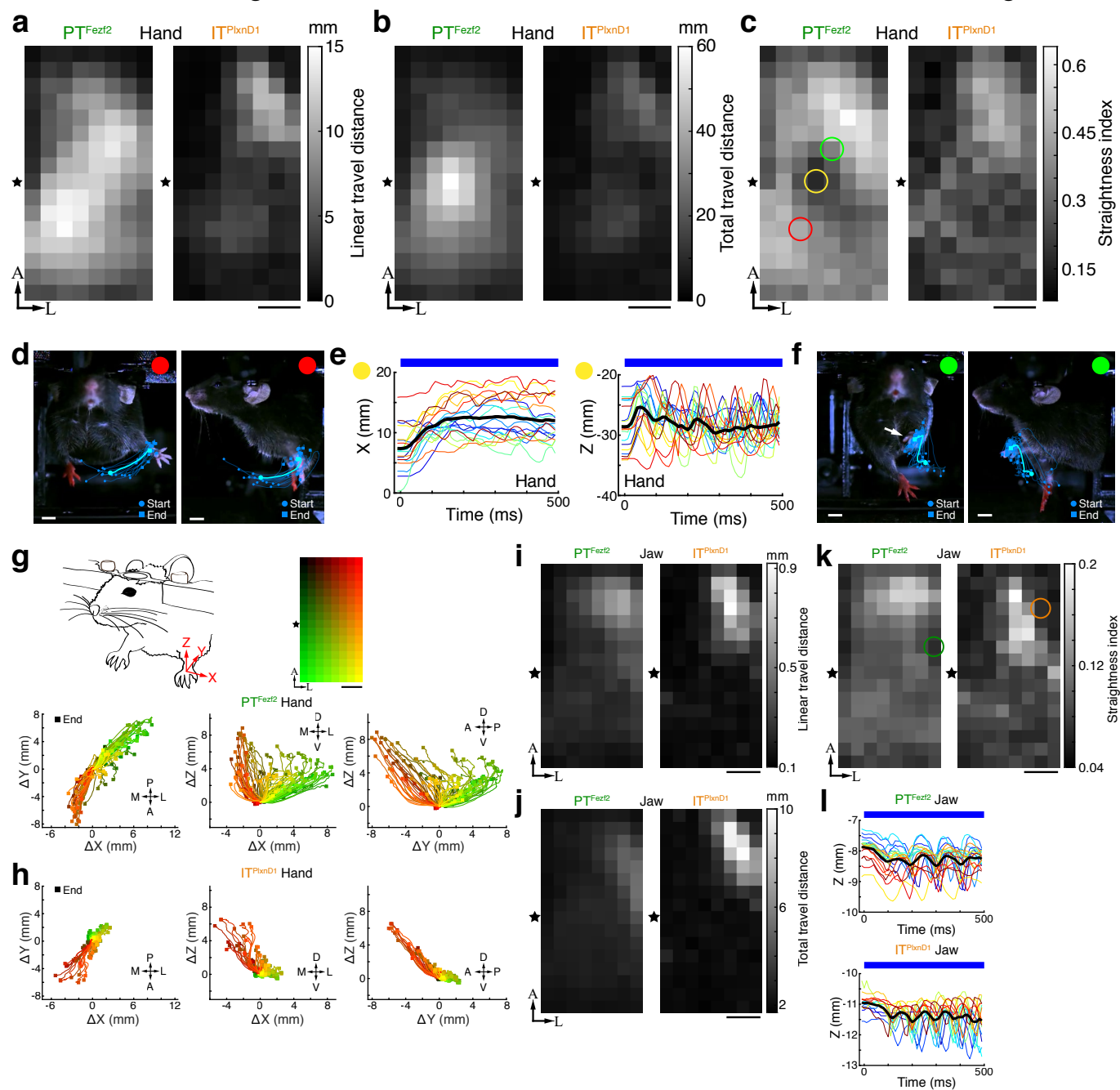
825 PG, pontine gray  
826 PL, prelimbic area  
827 PO, posterior complex of the thalamus  
828 PPN, pedunclopontine nucleus  
829 PSV, principal sensory nucleus of the trigeminal  
830 pyx, pyramidal decussation  
831 RSPagl, retrosplenial area, lateral agranular part  
832 RSPd, retrosplenial area, dorsal part  
833 SC, superior colliculus  
834 SCm, superior colliculus, motor related  
835 SI, substantia innominata  
836 SMT, submedial nucleus of the thalamus  
837 sp, cortical subplate  
838 Spd, spinal cord  
839 SPV, spinal nucleus of the trigeminal  
840 SSp-bfd, primary somatosensory area, barrel field  
841 SSp-ll, primary somatosensory area, lower limb  
842 SSp-m, primary somatosensory area, mouth  
843 SSp-n, primary somatosensory area, nose  
844 SSp-tr, primary somatosensory area, trunk  
845 SSp-ul, primary somatosensory area, upper limb  
846 SSp-un, primary somatosensory area, unassigned  
847 SSs, secondary somatosensory area  
848 STN, subthalamic nucleus  
849 STR, striatum  
850 V, motor nucleus of trigeminal  
851 VAL, ventral anterior-lateral complex of the thalamus  
852 VII, facial motor nucleus  
853 VISa, anterior area  
854 VISam, anteromedial visual area

- 855 VISC, visceral area
- 856 VISp primary visual area
- 857 VISpm, posteromedial visual area
- 858 VISrl, rostromedial visual area
- 859 VM, ventral medial nucleus of the thalamus
- 860 VPM, ventral posteromedial nucleus of the thalamus
- 861 ZI, zona incerta

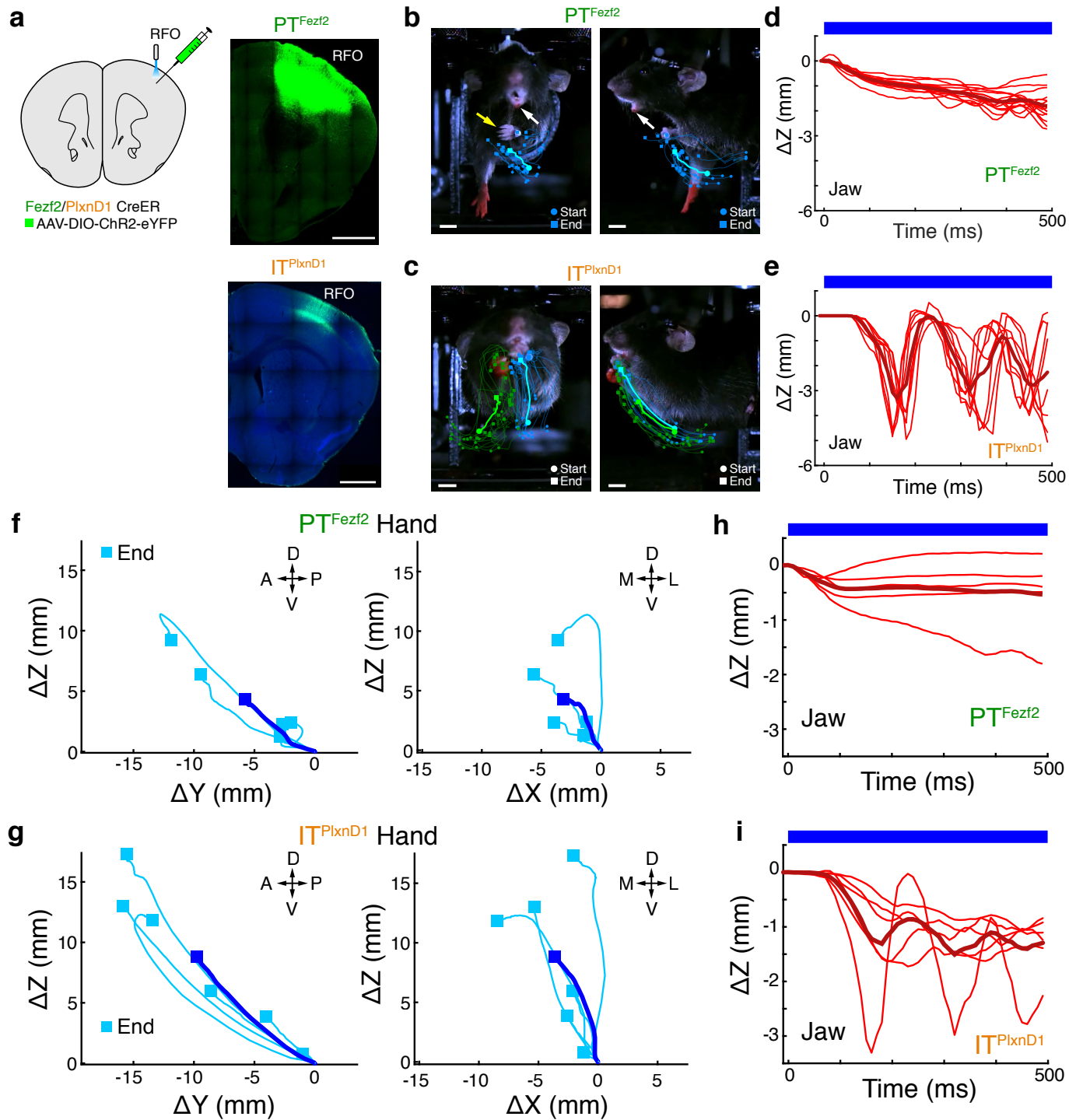
# Figure 1



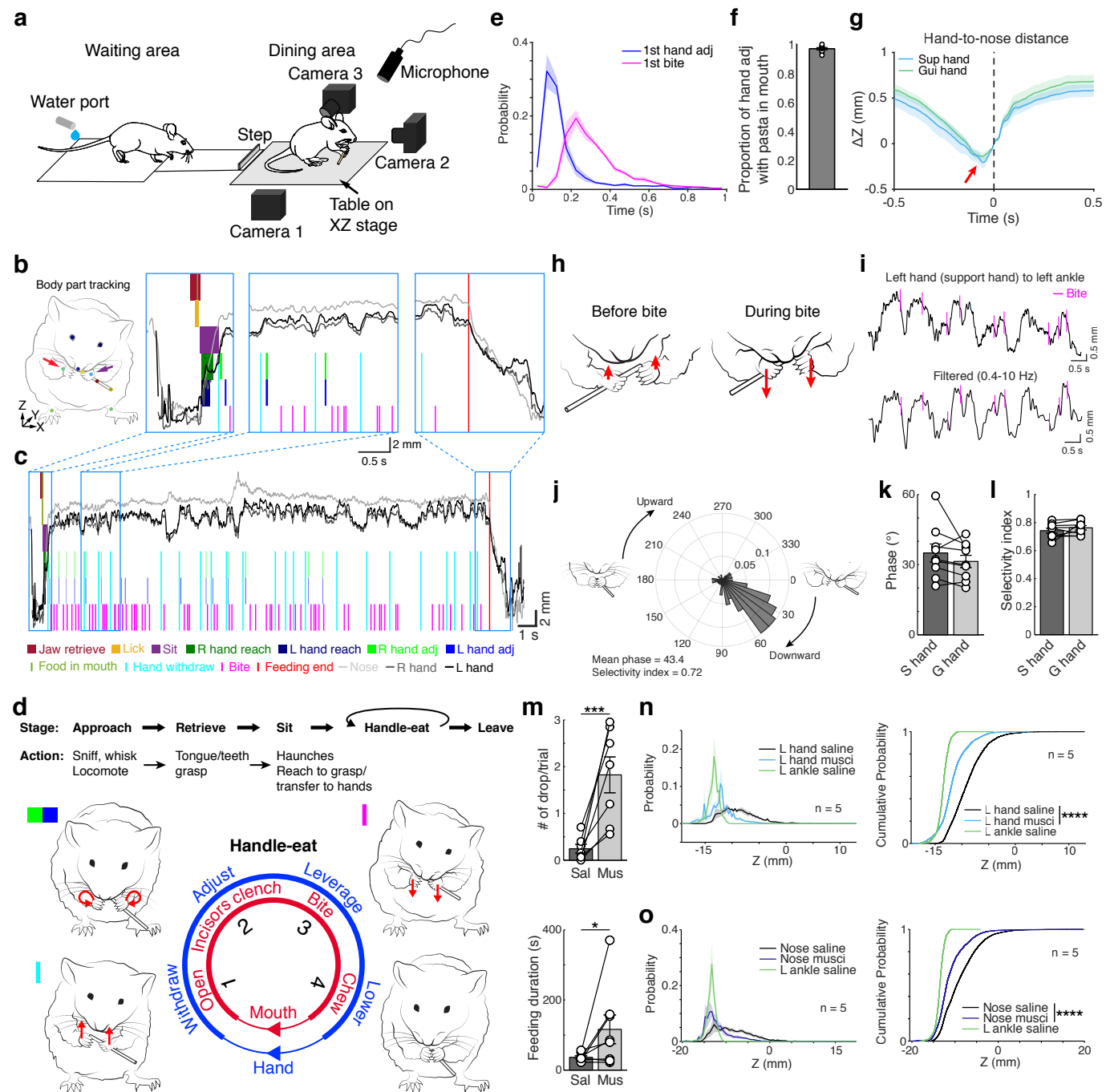




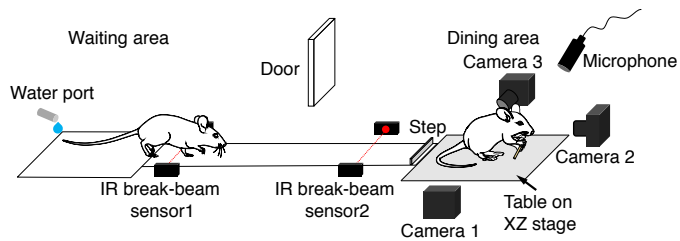
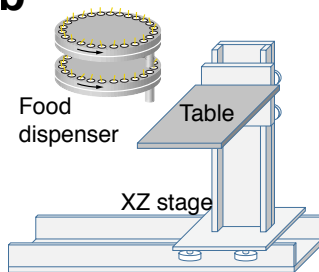
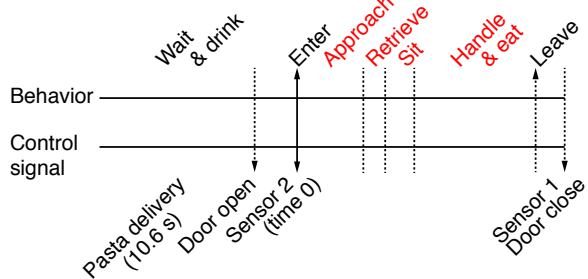
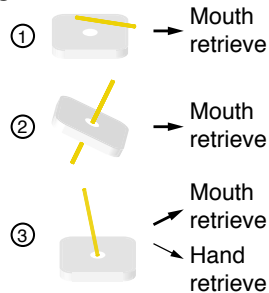
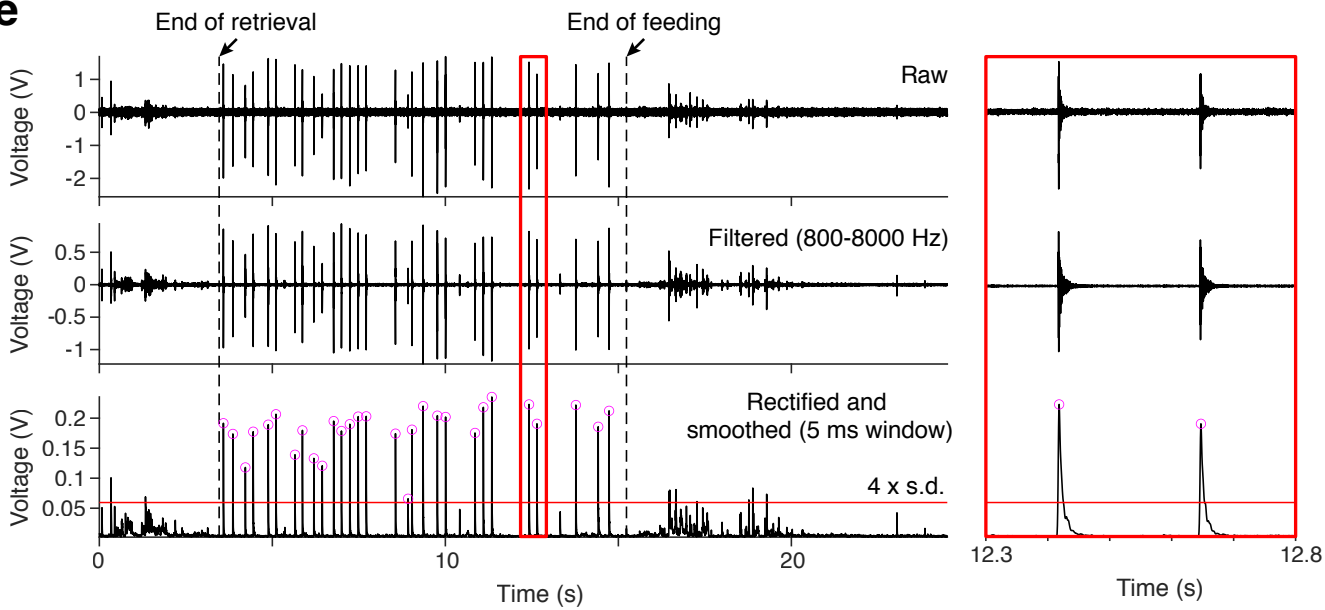
## Extended Data Figure 3

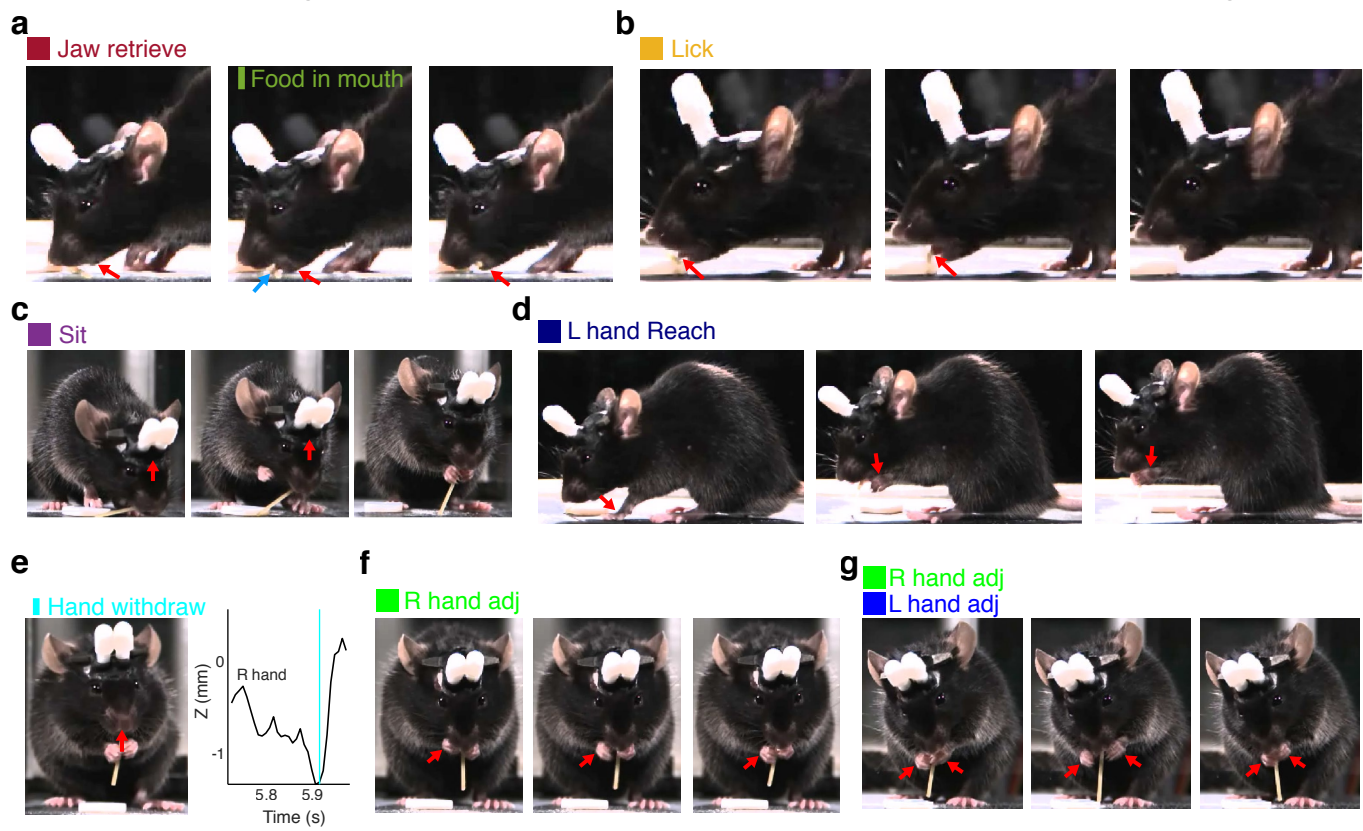


**Figure 2**

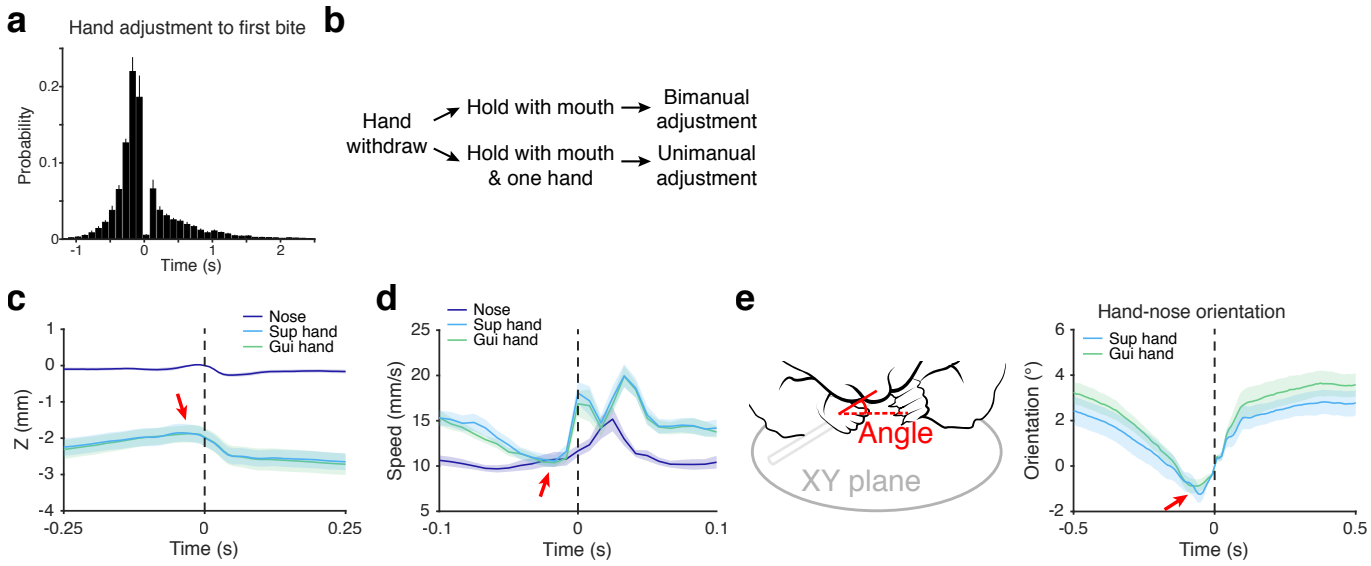


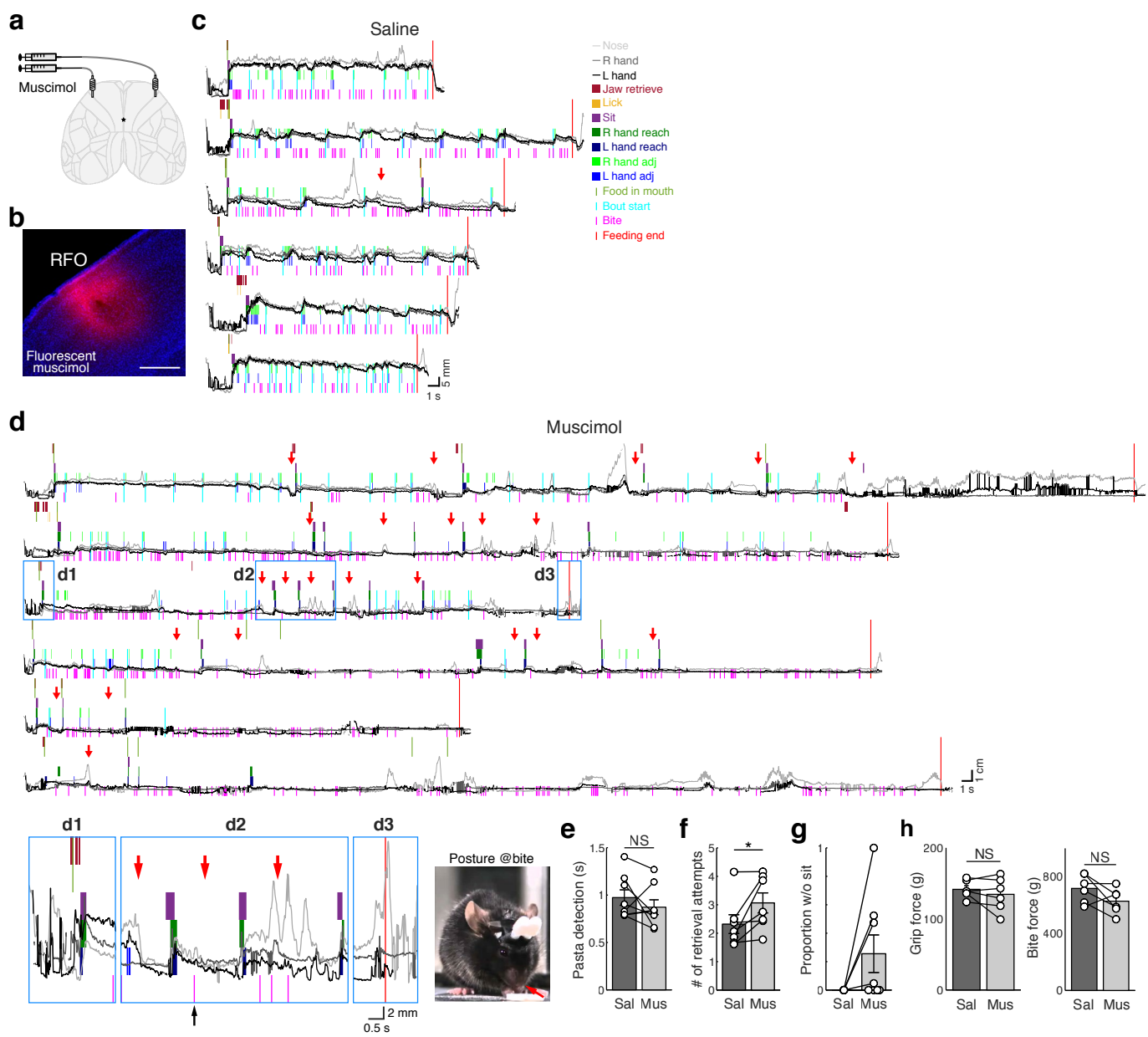
## Extended Data Figure 4

**a****b****c****d****e**

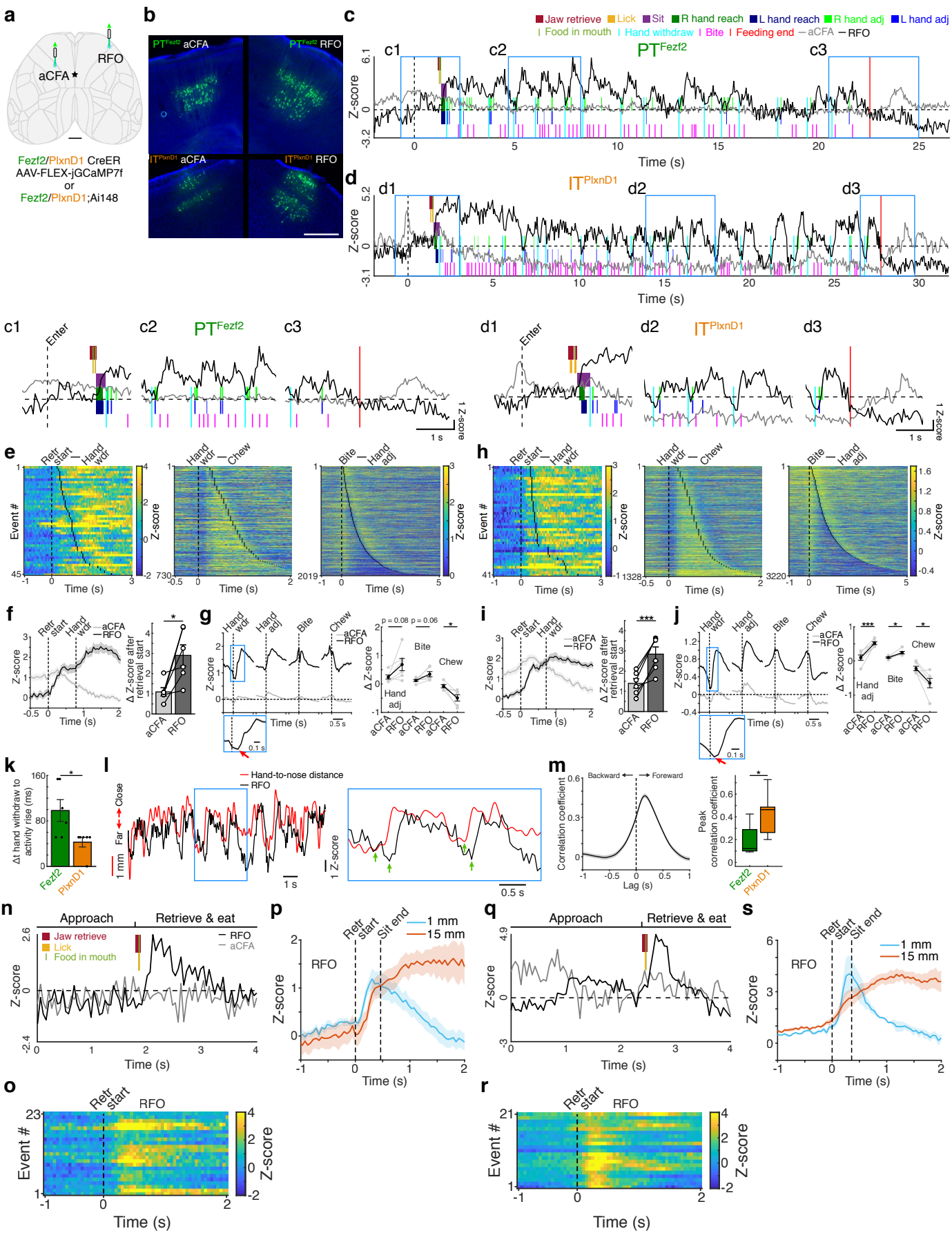


## Extended Data Figure 6

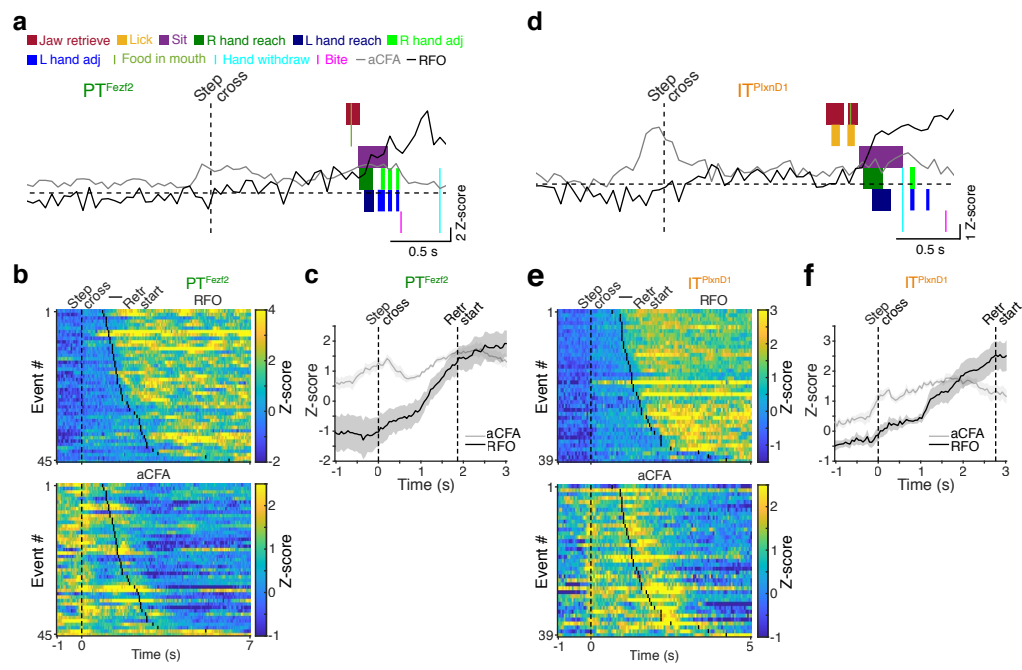




**Figure 3**



## Extended Data Figure 8



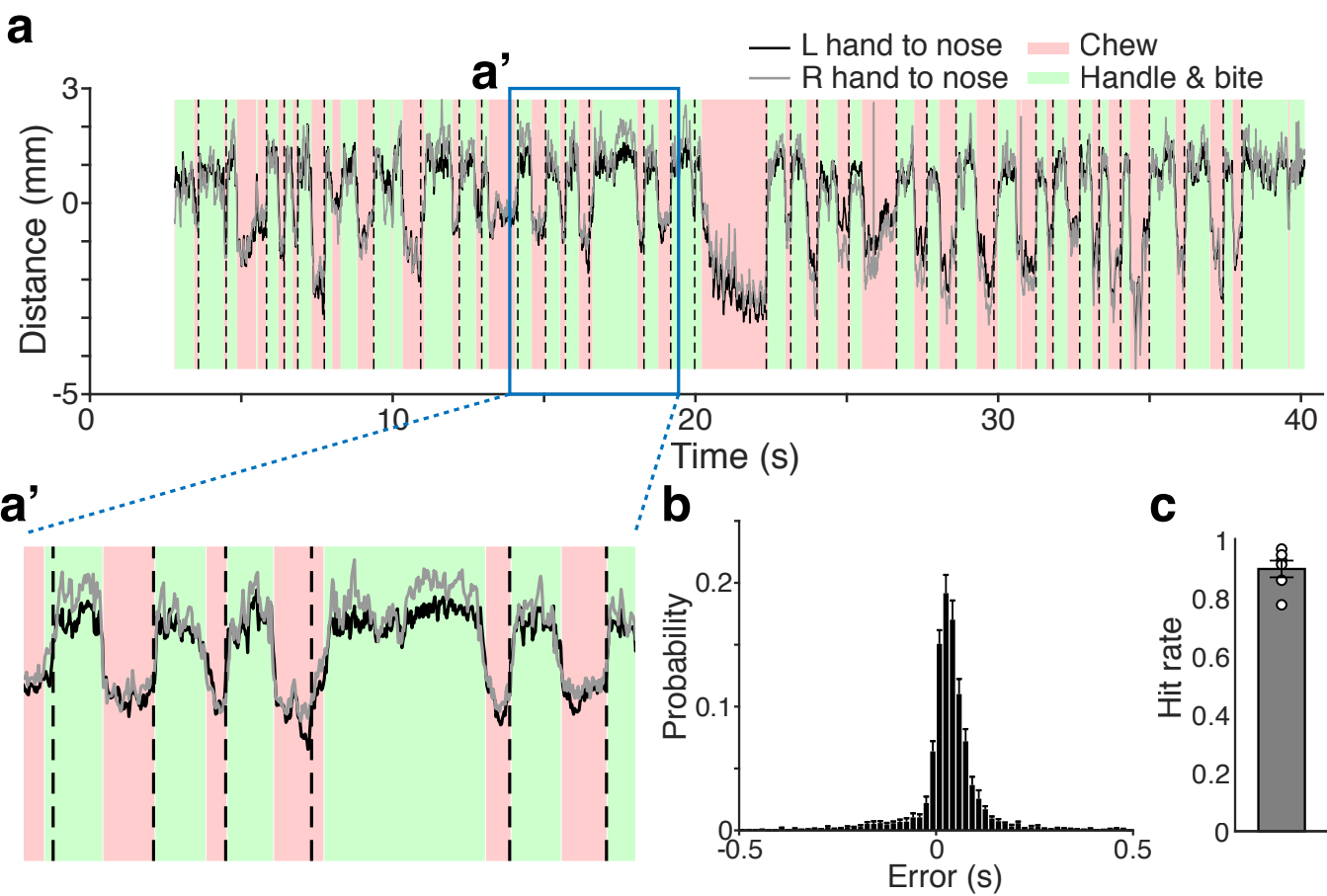
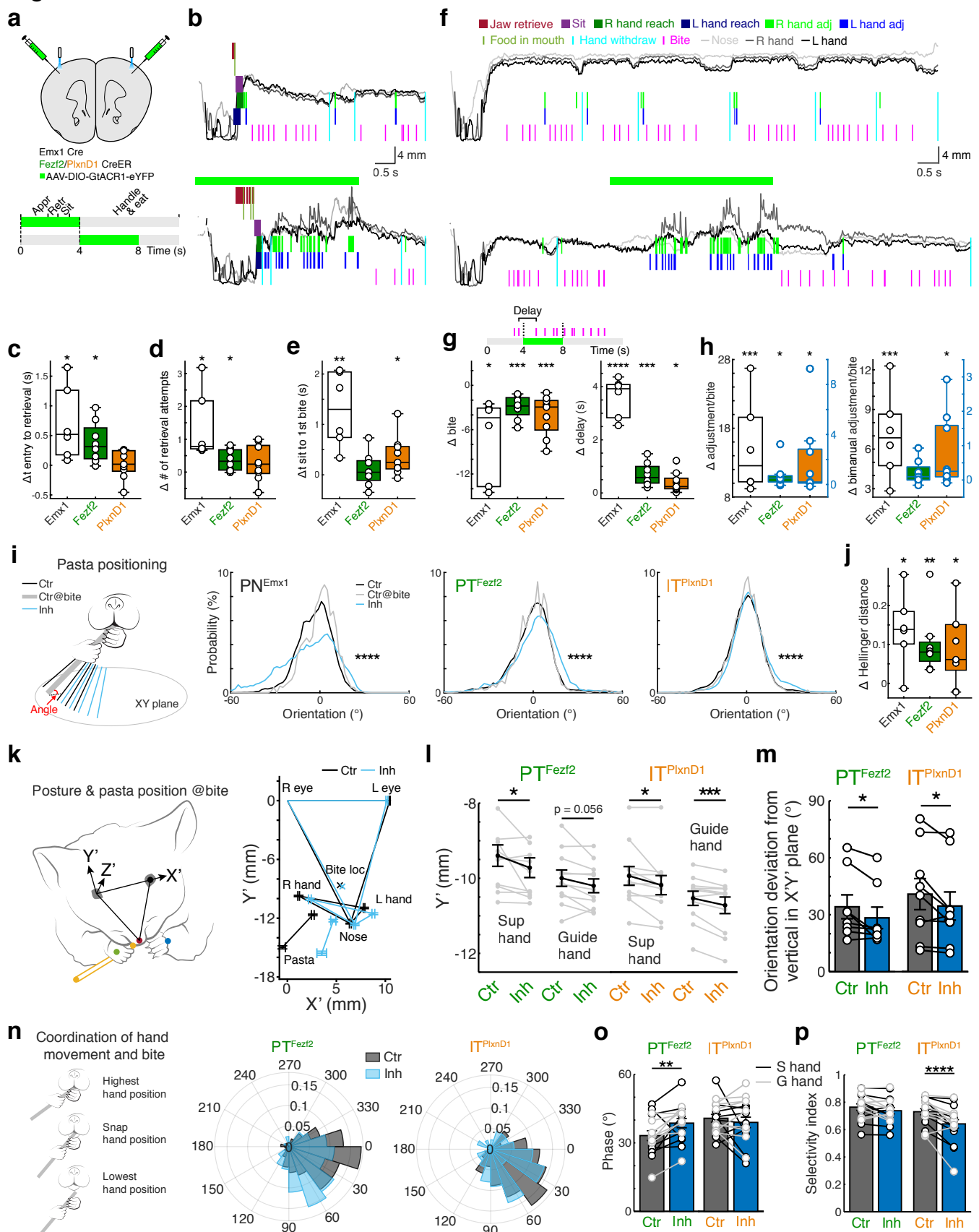
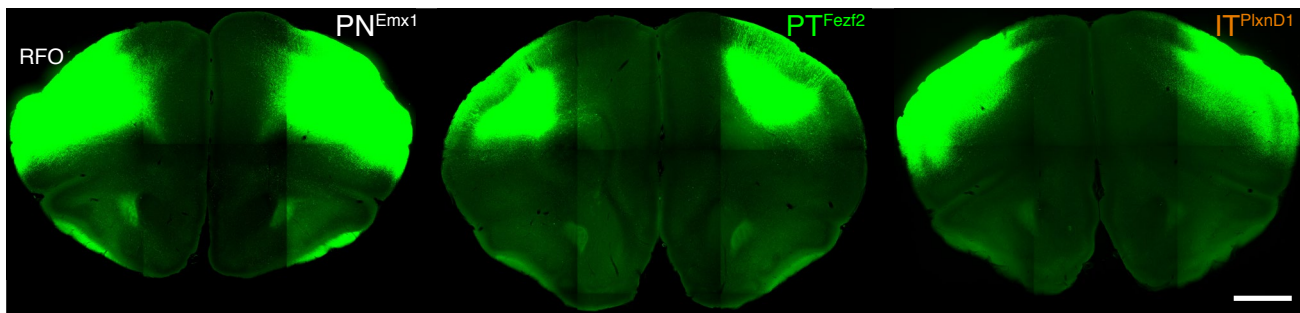


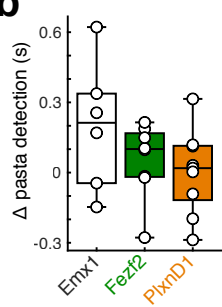
**Figure 4**



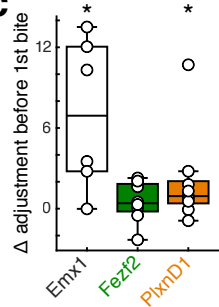
**a**



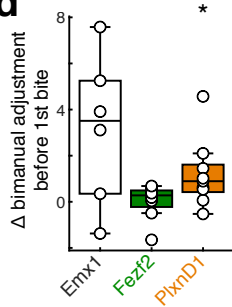
**b**



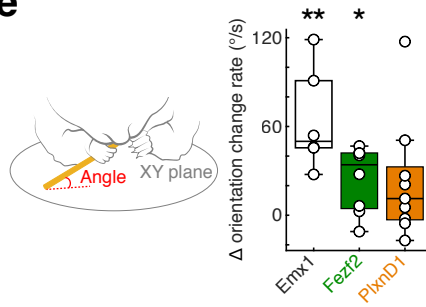
**c**

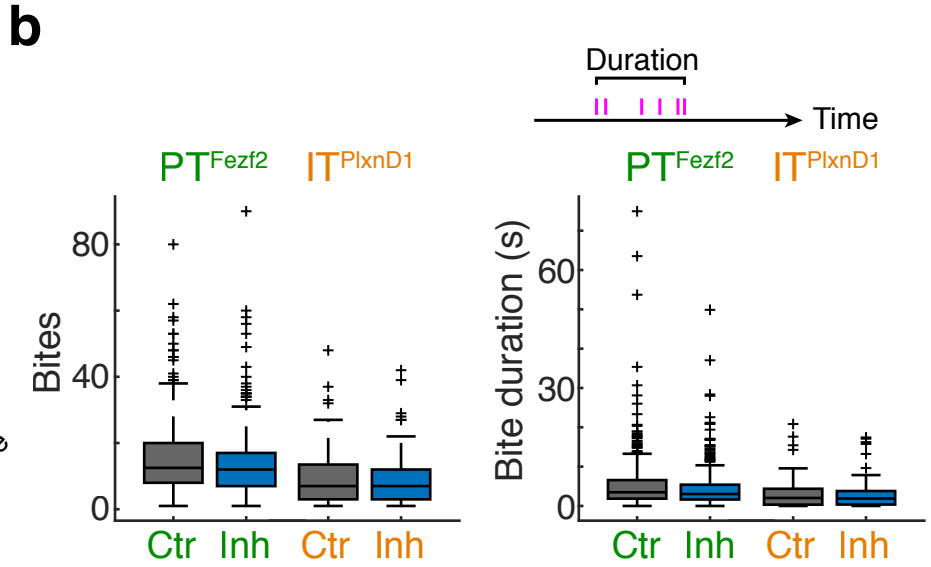
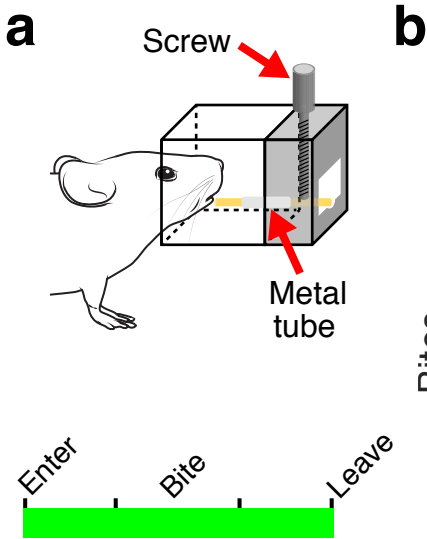


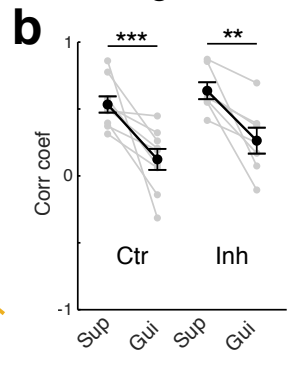
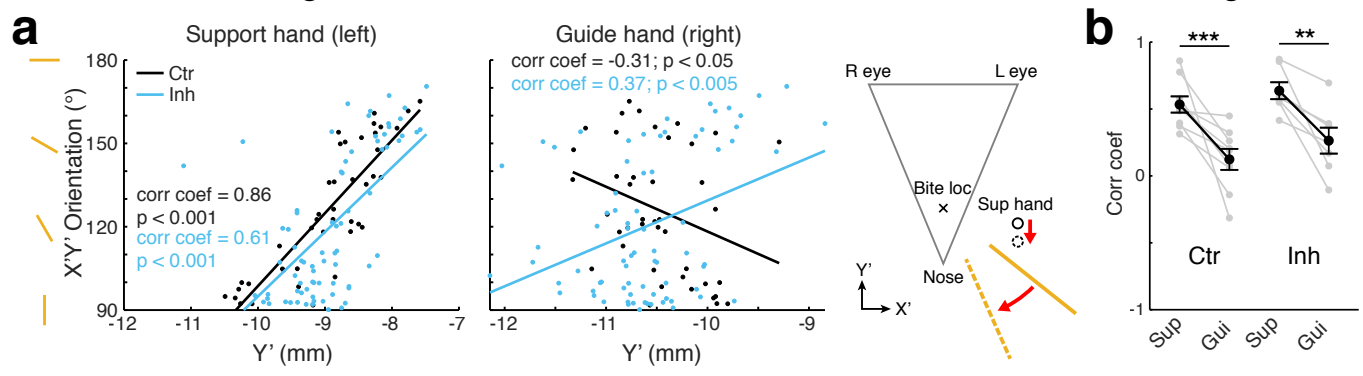
**d**



**e**







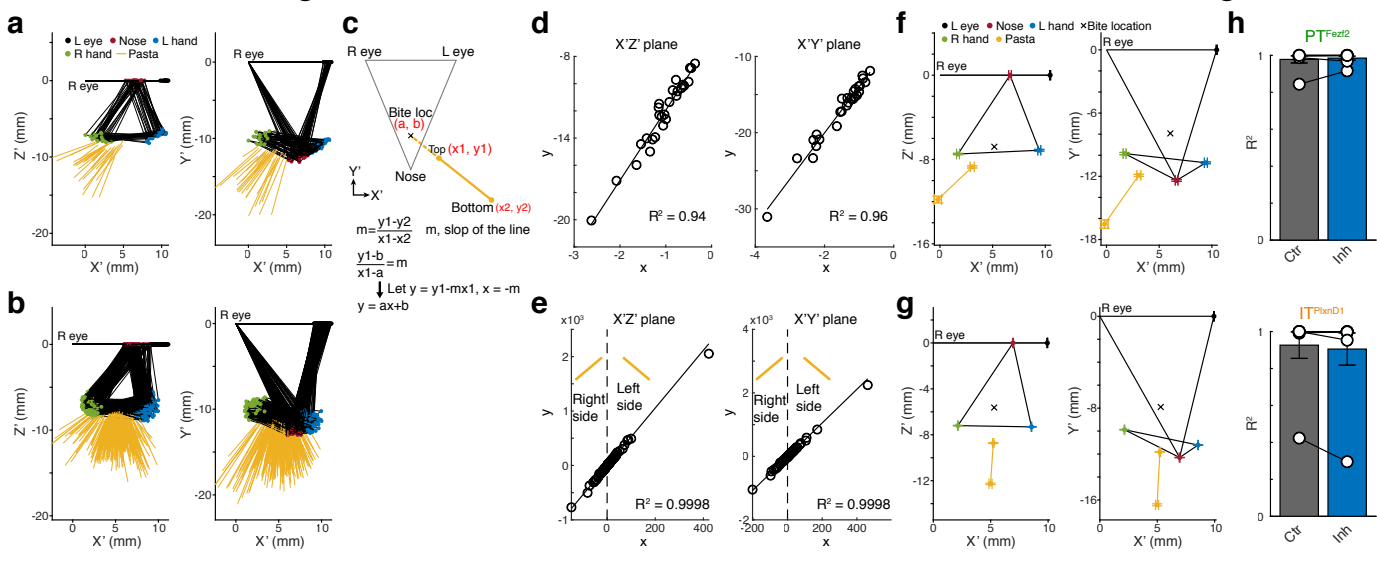
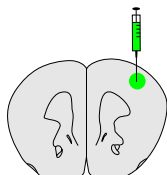


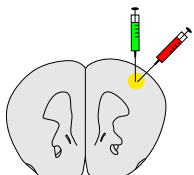
Figure 5

**a**



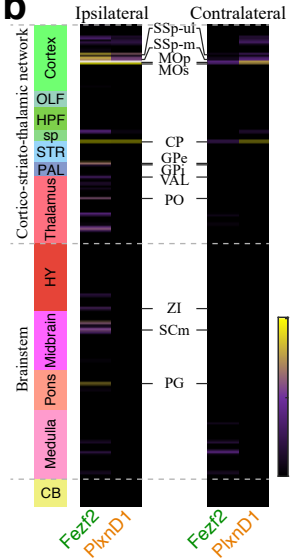
Fezf2<sup>CreER</sup>/PlxnD1<sup>CreER</sup> X Rosa-stop<sup>fllox-flp</sup>  
 Tamoxifen @ P21, P28  
 AAV-fDIO-TVA-eGFP

**c**

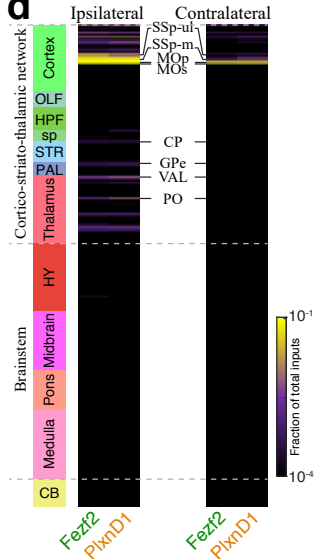


Fezf2<sup>CreER</sup>/PlxnD1<sup>CreER</sup>  
 Day 0 : AAV-FLEX-TVA-eGFP-eG  
 Day 21 : Rabies-EnvA-SAD-ΔG-mCherry  
 Tamoxifen @ Day 2, 5, 8

**b**



**d**



**e**

